University of New Mexico
UNM Digital Repository

Mechanical Engineering ETDs | Engineering ETDs

9-1-2015

A Mesh Objective Algorithm for Modeling Mode-I Cracks Using a Standard Finite Element Formulation

Damon Burnett

Follow this and additional works at: https://digitalrepository.unm.edu/me_etds

Recommended Citation
Burnett, Damon. "A Mesh Objective Algorithm for Modeling Mode-I Cracks Using a Standard Finite Element Formulation." (2015).
https://digitalrepository.unm.edu/me_etds/26

This Dissertation is brought to you for free and open access by the Engineering ETDs at UNM Digital Repository. It has been accepted for inclusion in Mechanical Engineering ETDs by an authorized administrator of UNM Digital Repository. For more information, please contact disc@unm.edu.

Damon J. Burnett

Candidate

Mechanical Engineering

Department

This dissertation is approved, and it is acceptable in quality and form for publication:

Approved by the Dissertation Committee:

Howard Schreyer & Yu-Lin Shen , Chairpersons

Tariq Khraishi

Deborah Sulsky

Paul Taylor

A Mesh Objective Algorithm for Modeling Mode-I Cracks Using a Standard Finite Element Formulation

by

Damon J. Burnett

B.S., Mechanical Engineering, Colorado School of Mines, 2000
M.S., Mechanical Engineering, Rensselaer Polytechnic Institute, 2002

DISSERTATION

Submitted in Partial Fulfillment of the
Requirements for the Degree of

Doctor of Philosophy
Engineering

The University of New Mexico
Albuquerque, New Mexico

July, 2015

Dedication

To the teachers that made a difference – Ms. Heinz, Ms. Wilkes, Ms. Lord, Mr. Mcintosh, Mr. Byrd, Ms. Morris, Mr. Krumm, Mr. Hanewald, Ms. Parkinson, Mr. Wildman, and Mr. Best

Acknowledgments

I would first like to express my deepest gratitude to my advisor Dr. Howard "Buck" Schreyer for his dedication, guidance, contributions to this challenging problem, and the many enjoyable lunches that we spent discussing cracks, kinematics, and many other topics. I would also like to thank my co-advisor Dr. Deborah Sulsky for her series of excellent courses on numerical methods and assistance with many facets of the research. I would also like to acknowledge Dr. Yu-Lin Shen, Dr. Tariq Khraishi, and the UNM ME department staff.

I would like to thank my colleague and friend Dr. Paul Taylor for his mentorship, friendship, and guidance throughout my work and education and Mr. Douglas Dederman for being very supportive of my career and education. I acknowledge Mr. Ryan Terpsma and Dr. John Ludwigsen for providing useful comments and discussion during the course of the research.

I would also like to gratefully acknowledge the University Part-time Program at Sandia National Laboratories for giving me the opportunity and financial support to go back to school while working part-time. All this wouldn't have been possible without such support.

Finally, I would like to thank my wife, Kym, for being patient, understanding, and supportive under such challenging circumstances. I could not have done it without you.

A Mesh Objective Algorithm for Modeling Mode-I Cracks Using a Standard Finite Element Formulation

by

Damon J. Burnett

B.S., Mechanical Engineering, Colorado School of Mines, 2000
M.S., Mechanical Engineering, Rensselaer Polytechnic Institute, 2002
Ph.D., Engineering, University of New Mexico, 2015

Abstract

A computationally efficient mesh objective algorithm for modeling mode-I cracks is developed and implemented within a standard finite element formulation. The algorithm applies the crack opening displacements across the standard nodal degrees of freedom that is consistent with formalism of the conventional smeared crack approach.

Various versions of the conventional smeared crack approach have been proposed since the introduction of the finite element method. The approach has not been successful for the following reasons: (i) accumulation of spurious shear resulting in stress locking, (ii) misalignment of the stress field around the cracked element, and (iii) incorrect prediction of the crack propagation direction.

Four new and distinct techniques are developed to preclude both spurious shear accumulation and misalignment of the stress field around the crack tip to provide mesh objective results. First, to preclude shear locking, a modified failure constitutive model is developed, which derives an alternative for the stress increment rather than using the full strain field of the cracked element. The crack orientation is held

fixed after crack initiation to provide an accurate representation of the crack orientation and resulting crack path. A tangent crack stiffness is derived to provide an explicit update for the stress components without the need for an iterative solver for both linear and nonlinear softening.

Next, a computationally efficient crack tracking algorithm is implemented to preclude the misalignment of the stress field. The tracking algorithm uses the crack orientation predicted from the failure model and a series of crack segments to define the crack path.

An hourglass control method is developed for an element undergoing softening. The tangent crack stiffness is used to derive hourglass forces that help obtain mesh objectivity when one-point quadrature is applied.

Finally, a cross-over scaling method is used to provide the correct characteristic crack length to obtain complete mesh objectivity.

The developed methods work collectively to provide a fully explicit and efficient algorithm for modeling mode-I failure in brittle materials without mesh bias. It is demonstrated that the algorithm predicts load deflection curves and crack paths that are independent of both mesh size and orientation when modeling failure at an angle through a finite element mesh. The methods developed are expected to be applicable to higher dimensions and for mode-II failure.

Contents

List of Figures

Chapter 1

Introduction

Several approaches have been formulated to predict crack propagation in a variety of materials from ductile metals to brittle concrete undergoing controlled quasi-static deformation and highly dynamic blast or penetration loading. Ultimately, the goal is the same in either case and that is to develop a numerical method that predicts the primary features observed in experimental data while at the same time providing results that are insensitive to the numerical discretization. This dissertation focuses on developing a simple algorithm that can be used to model cracks within a standard finite element formulation that is insensitive to the spatial discretization using the smeared crack approach (SCA) originally proposed by Rashid [1]. This chapter provides the motivation, objectives, and a brief introduction into the previous work of other researchers that relate to modeling material failure and concludes with a narrative summary.

1.1 Motivation

Structural components inherently contain stress concentrations and defects which upon loading may eventually create the necessary conditions in a localized region of the material to initiate cracks leading to bulk structural failure. As a consequence, there is still a need to develop computational tools and constitutive models that predict the material failure process. With the popularity of the finite element method (FEM) over the past several decades in research and applied engineering and its extensive use in modeling continuum problems, generating cracks within a finite element framework is relevant and the work within this research area is still vigorous.

Presently, the computational failure mechanics community does not possess an adequate methodology to simulate failure at an angle through a computational domain using a standard finite element formulation. A finite element computational failure methodology is composed of two key components: (i) a numerical representation for a crack surface and (ii) a constitutive model that somehow links the traction acting on the crack surfaces to the crack opening displacement. We believe that the term adequate embodies the following requirements for the computational failure methodology: (1) mesh size and orientation independent, (2) computationally efficient, (3) allows for failure at an arbitrary angle, and (4) is straight-forward to implement within a finite element framework.

In order to satisfy the requirements stated previously, we feel that a continuous representation of a crack within a finite element is the best approach because of its simplicity and the fact that an arbitrary crack orientation can be specified. In addition, the ability to predict the crack orientation is necessary. If the initial predicted crack orientation is erroneous, the direction of crack propagation will probably be incorrect, irrespective of the numerical procedure. We choose to use a decohesive constitutive model that provides the stress at failure, crack surface orientation, and crack opening displacement.

The pathological sensitivity to the orientation of the mesh was the primary reason why SCA was abandoned in the 1990's over discrete methods such as that originated by Ngo and Scordelus [2] and more recently the extended finite element method (XFEM) introduced by Belytschko and Black [3]. As a result, SCA requires substantial improvements to alleviate mesh orientation bias. The solutions to these problems with SCA form the basis of this dissertation.

1.2 Objectives and Scope

The objective of the research is to develop a computationally efficient algorithm for modeling mode-I cracks in primarily brittle materials using the smeared crack approach. The materials of interest are concrete and geological materials undergoing stress paths without much lateral confining stress. Under this loading, concrete and rock typically fail due to the loss of cohesion that is tied to the most tensile principal stress. As a result, slip due to shear is rather limited and is not of concern in this work. Even though concrete can exhibit large plastic deformations prior to failure under large confining stress, this work assumes that the material behaves elastically under small deformations for problems with low confining stress prior to mode-I failure. Much of the history of modeling failure in finite elements is tied to these very assumptions as many of the original computational methods were developed to model the brittle response of concrete. Here we formulate a set of requirements for the computational failure algorithm:

- mesh size and orientation independent - mesh objectivity
- allows for failure at an arbitrary angle
- implemented within a standard finite element formulation
- straightforward to implement into an existing finite element code
- computationally efficient
- remeshing isn't necessary.

1.3 Preliminary Remarks

Before we start to address the problems associated with material failure, there are a few key points that must first be stated to clarify subsequent concepts. First, material failure, as it is discussed in this dissertation, is separation of material such that two new surfaces are generated. The geometric structure generated from the failure process is denoted a macrocrack and the energy required to form the macrocrack per unit of surface area generated is termed the fracture energy. The state of the material in between failure initiation and a macrocrack is termed a microcrack. The term crack is used to represent either a microcrack or macrocrack.

The focus is on modeling tensile failure of materials that exhibit brittle behavior under small lateral compression such as concrete where the cohesive characteristics of the material govern the crack formation and shape of the load deflection curves. As a result, we assume that the deformation within the material is small and that the material remains elastic until failure. The general idea is to approximate the complex behavior of gradual microcracking and tortuous decohesion that eventually leads to a macrocrack within the material using a failure model that provides the necessary features observed in experiments such as the crack path shape and load deflection curves that exhibit a negative slope.

The term smeared crack approach is not a constitutive model, but an approach that is used to represent a crack continuously in a finite element. This is accomplished with the assumption that the total strain computed at each quadrature point is additively decomposed into an elastic and inelastic contribution denoted *crack strain*, where the latter is exclusively due to the crack opening displacement. SCA provides a geometric representation of a crack within a finite element using the standard nodal degrees of freedom of an element without altering the mesh topology such that remeshing isn't necessary. Only elements that have initiated failure contain crack strain.

The term smeared crack model represents a class of failure constitutive models that use an orthotropic stiffness tensor to directionally degrade the stress in an element that contains a crack. These models apply the formalism of the smeared crack approach to represent a crack in a finite element.

Finally, the term standard finite element formulation refers to the classical finite element method where nodal displacements are the unknowns and standard shape functions are used. The specific finite element implementation used in this dissertation was taken directly from Hughes [4] with computation of the nodal force vector rather than the stiffness matrix.

1.4 Previous Research

As stated previously, a finite element computational failure methodology requires a constitutive model that links the forces acting on the crack surfaces to how far the crack has opened and a numerical representation for a crack surface. This section will briefly review previous work of other researchers in these two areas with emphasis placed on quasi-brittle materials such as concrete, rock, and ice. The intent is to provide a brief introduction of a few methods that relate to quasi-brittle materials.

1.4.1 Methods for Modeling Failure

The primary objective of computational failure mechanics is to solve a set of governing equations numerically that describe the material's response before, during, and after strain localization, when subjected to certain boundary conditions. The resulting solution should not depend on the the mesh. The governing equation in solid mechanics, without thermal considerations can be expressed in terms of the Cauchy stress tensor $\boldsymbol{\sigma}$ as

$$\rho\ddot{\mathbf{u}} = \nabla \cdot \boldsymbol{\sigma} + \mathbf{f}, \tag{1.1}$$

where $\mathbf{u}$ is a vector defining the displacement of a point defined within a body, $\ddot{\mathbf{u}}$ is the acceleration, ρ the density of the material of which the body is composed, and $\mathbf{f}$ is the body force per unit volume acting on the body at the point. The nomenclature used is that scalars are *italicized*, vectors are not italicized and are in **bold**, second order tensors are in **bold** and are capitalized unless they are symbols, and finally fourth order tensors are denoted by letter like symbols (e.g. $\mathbb{E}$) unless otherwise noted. In addition, we also require a relationship between the forces in the body and the amount of displacement generated by these forces. Practically, this is accomplished through a definition of a strain measure (kinematic equation) and an equation relating the stress to the strain (constitutive equation). The form of the constitutive equations are composed such to reproduce the key features observed in data acquired through laboratory material testing. Together these equations form a description for the response of a continuum.

Continuum Softening Models

Continuum softening models involve strain softening and a definition of failure based on an invariant (often of plastic strain) after which stress is reduced to zero, usually isotropically, using a damage variable. Although such a constitutive model makes no pretense of modeling the physical features of material separation, it is such a convenient approach for use with existing numerical codes that the method is widely used. Results are mixed for the following reasons: (1) once softening is allowed, there is the possibility that the problem becomes ill-posed with the consequence that convergence with mesh refinement cannot be demonstrated and (2) the energy dissipated prior to failure initiation and fracture energy are combined and rarely discussed in connection with the choice for the critical value of the invariant used to define failure.

The primary reason why continuum models are used is because numerical algorithms based on continuum constitutive models can be used with minor modifications

to underlying numerical algorithms. The fundamental challenge is solving eq. 1.1 for which the stress-strain relationship has a negative slope characterized by a reduction of stress with an increase of strain. This regime of material behavior occurs after the peak stress has been reached and is referred to as strain-softening. Within this regime, the governing partial differential equations may lose hyperbolicity (or ellipticity for $\ddot{\mathbf{u}} = 0$) and the boundary value problem may become ill-posed. This results in a bifurcation where a unique solution is not available with continuous dependence on the boundary conditions thereby generating a material instability. Numerically, the solution becomes pathologically dependent on the numerical discretization or more specifically the size of the finite elements. In addition, as the size of the finite element that represents the localization zone is further reduced, the predicted fracture energy continuously drops towards zero which is nonphysical. As a result, special treatment of the mathematical problem must be carried out for materials undergoing strain localization. Determining when or under what conditions material localization occurs is an important aspect of modeling failure because the point at which to engage the failure portion of the constitutive equations must be known.

Mathematical Aspects of Continuum Softening

The conditions of bifurcation were examined by Hill [5] who postulated that the second order work must remain positive generating the necessary condition that the tensor inner product of the stress rate and strain rate remain positive or $\dot{\boldsymbol{\sigma}} : \dot{\boldsymbol{\epsilon}} > 0$, which suggests that the slope of the stress-strain curve remain positive. For problems where the orientation of the plane of instability is important, the condition that the acoustic tensor $\mathbf{A}$ is positive definite or that the eigenvalues remain positive can be used as in Schreyer and Neilsen [6, 7] where the acoustic tensor is defined as,

$$\mathbf{A}(\mathbf{n}) = \mathbf{n} \cdot \mathbb{T} \cdot \mathbf{n} \tag{1.2}$$

where $\mathbb{T}$ is the fourth order tangent tensor and $\mathbf{n}$ is a vector normal to a potential instability plane. The determination of the plane of instability, which could be

assumed to be the plane of material failure, requires a computationally intensive search for the smallest eigenvalue of the acoustic tensor for all possible orientations defined by **n**. The plane of instability is then defined by the normal vector **n** that generates the negative eigenvalue of the acoustic tensor. Unfortunately, failure stress and failure surface orientations predicted from the eigen-analysis of the acoustic tensor do not match the failure orientations observed in experiments for quasi-brittle materials [8]. Bazant [9] recognized that if the region of softening was limited to a fixed width and if the finite element size was limited to this characteristic dimension, then mesh size objectivity could be obtained. This concept later became the crack band theory [10] applied to modeling fracture in concrete.

Nonlocal Models

Nonlocal formulations were proposed for modeling fracture by Eringen [11] and later applied by Bazant and Lin [12] for fracture in concrete. These type of formulations assume that the stress is a function of a nonlocal strain measure or a spatial average of some strain measure. In [12], a nonlocal damage variable that is a function of the spatial average of the most tensile principal strain is used to preclude mesh dependence. However, as Jirásek [13] found for modeling fracture in quasi-brittle materials, there can be a residual force in the material as the crack fully opens that is similar to a stress locking effect. Nonlocal methods in the context of modeling crack propagation in finite elements are also useful to prevent the crack paths from following element edges that are at an angle relative to the crack orientation as well as preclude some of the ill-posedness issues as noted previously. Nonlocal methods provide a length scale that continuum softening models do not provide. Upon strain localization, the nonlocal length scale controls the size of the localization zone thereby precluding some of the problems associated with continuum softening models such as zero energy dissipation as the mesh size is reduced to zero.

Gradient enhanced methods use higher order strain gradients that introduce a

nonlocal effect. Aifantis [14, 15] used strain gradient constitutive equations to preclude strain singularities that arise during strain localization and fracture. Typically, a higher order differential operator is applied to the strain tensor and added to the conventional strain. This operator is typically the Laplacean (∇^2). Nonlocal and gradient enhanced approaches introduce complexity in how to handle the additional boundary conditions, a question on how to interpret material parameters, and added computational expense in order to resolve the high strain gradients.

Another nonlocal method called peridynamics [16] recasts the divergence of the stress term, as observed in the traditional equation of motion, with a nonlocal version using an integral of force densities exerted by a set of material points over a finite volume. This approach is designed to eliminate the problems associated with localization and failure observed with partial differential equations (PDEs), such as the loss of ellipticity for quasi-static problems. However, the use of traditional stress-strain based constitutive models is not straight-forward. Research is still on-going to address these issues [17, 18].

Smeared Crack Models - Fixed and Rotating Crack Models

Smeared crack models, as defined in this dissertation, use a tangent stiffness tensor to degrade the stress appropriately based on the orientation of the crack surface. They also follow the smeared crack approach formalism by decomposing the total strain into elastic and inelastic components. The inelastic strain portion is due to the crack opening displacements that are *smeared* over the standard nodal degrees of freedom of the cracked element. The form of the tangent stiffness tensor controls the mode of failure introduced into the cracked element. Because these models use the full strain tensor to compute the stress, they are susceptible to shear locking. Two common smeared crack models are the fixed crack model and rotating crack model as studied extensively by Rots [19, 20], de Borst [21], and Jirásek [22]. The fixed crack model fixes the crack orientation after failure initiates. However, spurious

shear stress is allowed to accumulate which leads to shear locking. In contrast, the rotating crack model allows the crack orientation to evolve such that the shear strain along the crack surface is zero. This is accomplished by assuming that the crack surface normal is in the direction of maximum principal strain. In simple terms, the spurious shear strain is essentially removed by rotating the crack surface. This helps to preclude some of the shear locking observed in the fixed crack model, but there is an inconsistency between the physical crack orientation and the orientation predicted from the model. As a result, the rotating crack model cannot accurately predict the physical crack path. The rotating crack model is still prone to shear locking for large crack openings. In [22], the proposed fix to preclude such problems was to introduce an isotropic damage variable, after the crack opening reached a certain extent, that would decay all components of the stress to zero as published in [23].

Discrete Crack Models

Discrete models of material failure prescribe an orientation of the failure surface together with an evolution equation for describing the change in traction on the failure surface with an increase in the displacement discontinuity of the failure surface. Discrete in this context implies the incorporation of the actual discontinuity as opposed to a continuum model that is based on the assumption of continuity.

Discrete crack models idealize complicated material behavior by introducing a constitutive equation that relates the traction along the crack surface $\boldsymbol{\tau}$, defined by a crack normal vector $\mathbf{n}$, to the crack opening displacement $[[\mathbf{u}]]$ in some local failure plane basis established by the crack orientation. These methods are not to be confused with discrete numerical representations of a crack as in [2][1].

Discrete crack models that use a failure or decohesion function to predict the failure stress and orientation of the crack are denoted a *decohesion* failure model. The models use a formulation that is similar to plasticity where the crack opening

[1]Discrete crack models can be used in the smeared crack approach as is done here.

displacement is determined such that the decohesion function is approximately equal to zero. However, instead of an increase in stress or hardening with an increase in equivalent plastic strain, a decohesion formulation provides the reduction in traction or softening, for an increase in the crack opening displacement. This type of model will be used in this dissertation and examples of such models for predicting failure in rock, concrete, and ice can be found in Xu [24], Schreyer [25, 8], and Sulsky [26]. It has been also shown in [8] that these type of models are able to predict the failure orientations observed in experimental data [27]. Further details are provided in Chapter 3 for the discrete failure model.

1.4.2 Numerical Representations

Regardless of the class of failure model chosen, we still need to decide how we represent a crack within our numerical discretization. This choice has ramifications on the complexity of implementation, the computational efficiency, and properties of the solution all of which influence development costs, runtime of simulations, and errors in the solution. In the 1960s and 1970s researchers developed the two primary numerical representations for failure in finite elements: (1) the continuous approach in which the effect of the crack is smeared over a finite area typically a finite element [1] and (2) the discrete approach in which the displacement discontinuities developed from material fracture are directly represented by the numerical discretization [2].

Continuum Representation

With the smeared crack approach, a crack is represented as a set of crack segments, where each segment has a constant discontinuity across an element. Figure 1.1 illustrates the differences between a discrete crack and a continuous representation of a crack. In Figure 1.1(a), the dashed line segments are continuous from one element to the next, although this isn't required. The key point is that the finite element

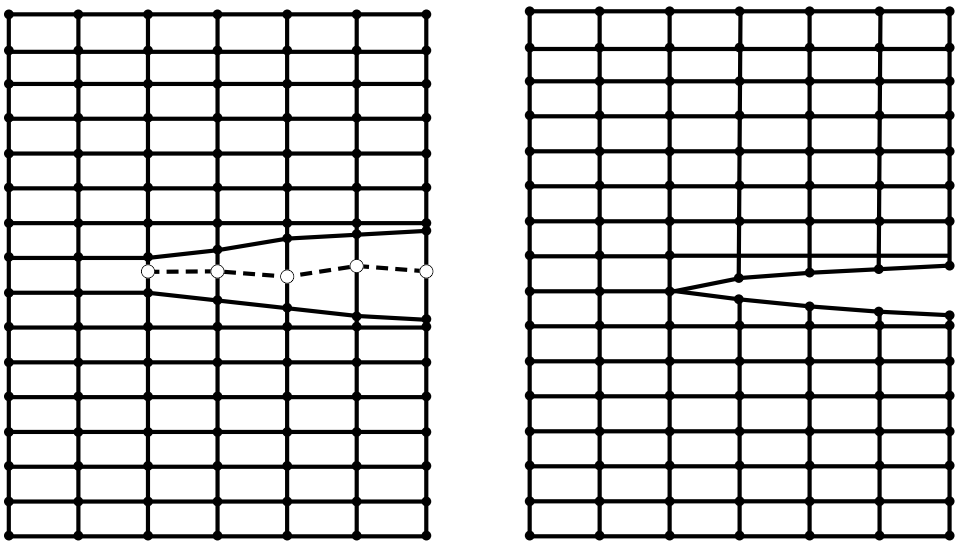

(a) Continuous (smeared) crack with mesh topology unchanged

(b) Discrete crack with mesh topology discontinuity

Figure 1.1: Smeared vs. Discrete Crack

mesh topology does not change as the crack propagates across the mesh. A uniform displacement discontinuity of a crack is considered as a corresponding displacement at the nodes of an element. The use of the conventional finite element kinematics relations for strain within an element results in a crack strain representing the crack displacement discontinuity in a continuum sense. The result is that the numerical scheme contains the same advantages of those of continuum models. However, as we will see, using the same kinematic relations for a cracked element as those for a continuum element introduces spurious components.

The advantage of the smeared crack approach is that it is relatively computationally inexpensive and the underlying finite element numerical structure does not require significant changes, which makes it straightforward to implement. If pervasive failure obtained during blast and penetration loading is of interest, then the smeared crack approach could be applied to a particle method that solves the governing equations on a background finite element grid such as the Material-point Method (MPM)

originally developed by Sulsky et. al. [28],[29], and [30] for modeling penetration. This approach was recently applied to modeling pervasive fracture in blast loading of rock in Xu et. al. [24]. Another approach that has been applied to modeling pervasive failure during penetration is a particle conversion method that converts a finite element into a particle once a criterion is reached such as in Johnson et. al. [31].

In addition, the angle of failure is not dependent on the topology of the finite element mesh as is the case in the discrete method in which the cracks must form along element edges. However, it was discovered that the smeared approach was susceptible to mesh orientation dependence when the finite element edges were not aligned with the crack manifested by inaccurate load deflection curves and crack paths[2]. Due to the simplicity of the method, a significant effort was made to resolve the problem by researchers in the 1980's and 1990s [19, 20, 23] and more recently [32, 33] with limited success. A more recent effort [34] using a mixed finite element formulation with displacmements and strains has shown that improved mesh objectivity is obtained if both strain and displacements are computed as unknowns at the nodes. This type of formulation requires twice as many unknowns as a standard finite element formulation and there are other stability issues to deal with related to the Babuška-Brezzi condition.

Embedded Discontinuities

Methods that introduce a discontinuity within a finite element to enrich its degrees of freedom encompass embedded discontinuities. A thorough review of the subject is provided by Jirasek [35]. The development of such methods was intended to help solve some of the issues associated with modeling strain localization and failure problems using finite elements.

[2]Having aligned element edges is only a limiting case of a more general requirement that will be derived in Chapter 2.

The general approach is to expand the degrees of freedom of an element such that a discontinuity is represented within a single band inside the element. An enrichment of the standard element basis functions is made for either strain or displacement. Ortiz et. al. [36] enriched the strain field within a quadrilateral element to improve the resolution of shear bands using a weak discontinuity (strain contains a jump and the displacement remains continuous). This idea was further developed by Belytschko et. al. [37] by introducing a band of localized strain where the width of the band was independent of the element size.

Another option is to add in a strong discontinuity (a jump in displacement) within the element as proposed by Dvorkin et. al. [38]. Linder and Armero [39] introduced embedded discontinuities that provide additional modes of deformation for a crack opening to model failure in concrete. For example, a crack is allowed to open linearly across the finite element, whereas, the standard approach is to assume a constant crack opening.

Here we note that the intent of embedded discontinuities is related to our own objective of resolving the problems of modeling cracks using finite elements. It is interpreted here, in a general sense, that embedded discontinuities are designed to preclude the formation of spurious shear strains within an element upon the formation of a crack. These methods also require additional integration points along the discontinuity line. In contrast, we focus here not on introducing more degrees of freedom within an element, but rather focusing on projecting out the spurious stresses that accumulate during crack evolution while keeping the properties of the element unchanged. We note that spurious strain and stress are only part of a broader problem of modeling cracks within finite elements as will be demonstrated later.

Discontinuous Representation

A discontinuous representation of a crack captures the geometric discontinuity that can be observed directly as shown in Figure 1.1(b). The first of these methods, introduced by Goodman et. al. [40] used interface elements with zero thickness along the interelement boundaries. This method was later applied by Hillerborg et. al. [41] and Rots [19] for modeling cracks in concrete using a cohesive crack model, which relates the crack surface traction to the crack opening displacement. Modeling failure in finite elements using this approach is not prone to shear locking as observed in [19] because there isn't spurious kinematic components introduced as the crack forms. However, the primary disadvantage to this approach is that cracks are restricted to follow element edge boundaries. Mesh refinement precludes this problem, but this introduces computational expense as the full mesh must be refined for problems that involve unknown crack paths a priori.

Automatic mesh refinement methods were used to preclude some of the mesh dependencies in earlier interface element methods. Ingraffea and Saouma [42] applied automatic mesh refinement to the crack tip region to model crack propagation in concrete. However, automatic mesh refinement is computationally expensive especially when it must be completed several times during a simulation.

The extended finite element method (XFEM) [3] is a numerical method based on the partition of unity method (PUM) and generalized finite element method (GFEM) [43]. The method enriches the solution space for discontinuous functions thereby improving the ability of the finite element method to model problems with discontinuities. A distinct advantage of the approach is that the discontinuity or crack can be tracked without remeshing. Usually the level set method is used to determine where the discontinuity is in the mesh. In simple terms, the crack opening displacements have their own degrees of freedom. As a result, the use of the standard nodal degrees of freedom to represent a crack is not required, which precludes some

of the shortcomings of the smeared crack approach. However, XFEM does have certain disadvantages which include complexity in the implementation, requirement to determine the location of the crack tip and it's trajectory, and the requirement to use refined meshes in the vicinity of the crack tip.

1.5 Narrative Summary

Chapter 2 provides an analysis of the smeared crack approach. Strain equations for the 4-node quadrilateral element are derived and are used to illustrate formation of spurious shear and normal strains. Chapter 2 also provides a summary of other possible remedies to SCA shortcomings that were examined.

In Chapter 3, a chronological review is provided that outlines the various approaches that were attempted to alleviate the issues with SCA. An overview of a decohesion failure model is provided next to introduce the important features of these class of constitutive models. Finally, a new decohesion failure model applicable to mode-I failure is developed to alleviate spurious shear stress accumulation during crack evolution for both linear and nonlinear softening.

Chapter 4 provides the necessary equations to implement the numerical algorithm such as the finite element formulation, the hourglass control methods, the crack tracking algorithm, and the complete numerical algorithm for an explicit dynamic time integration scheme. Finally, implementation of the algorithm within a host finite element code is discussed.

In Chapter 5, several numerical experiments are conducted to test the validity of the proposed methods. These include a mode-I model problem where a crack forms in the center of a two-dimensional bar and propagates to the edges. Various mesh sizes and orientations are examined. A set of double-edge-notch experiments are simulated under both direct tension and combined shear-tension load paths. Finally, a summary is provided in Chapter 6 that reviews the primary contributions.

Chapter 2

Spurious Shear Strain

This chapter provides an analysis of spurious shear strain that accumulates when a crack is introduced within an element for a standard finite element formulation. In a mode-I crack, where a normal crack strain is introduced, a spurious shear strain component is introduced that accumulates linearly with the crack opening displacement. Similarly, for a mode-II crack, where a shear crack strain is introduced, a spurious normal strain is produced. Finite element simulations have demonstrated that the bulk of mesh orientation bias, when the traditional smeared crack approach is applied, is caused from this spurious strain. Understanding the origins of spurious strain is important when attempting to formulate methods that preclude it.

First, the strain components in the global coordinate system for a 4-node quadrilateral element are derived. Next, an analysis is provided that illustrates the associated problems with opening up a crack in a 4-node quadrilateral element using the smeared crack approach. Constraints on the element geometry are derived that precludes spurious shear strain accumulation for a mode-I crack. Finally, a way to apply the crack opening displacement across the nodes to preclude spurious shear strain is presented followed by concluding remarks.

2.1 Strain Components for the 4-node Quad

The equations that follow are the basic equations (e.g. in [4]) obtained from a standard finite element graduate course. However, what usually isn't covered are the resulting strain equations for an arbitrary quadrilateral element in the global coordinate system. In this section, the equations usually carried through numerically in a finite element program are evaluated symbolically. A more detailed outline of the equations is provided in Chapter 4.

Consider an arbitrary 4-node quadrilateral element in a Cartesian coordinate system $\{x, y\}$ as shown in Figure 2.1(a). The local element numbering is counter-clockwise starting from the Southwest node. This arbitrary element geometry maps to the parent domain with an associated local element coordinate system $\{\xi, \eta\}$ as shown in Figure 2.1(b). The shape functions for the 4-node quadrilateral element in the parent domain can be written as,

$$N_1(\xi,\eta) = \frac{1}{4}(1-\xi)(1-\eta) \tag{2.1}$$

$$N_2(\xi,\eta) = \frac{1}{4}(1+\xi)(1-\eta) \tag{2.2}$$

$$N_3(\xi,\eta) = \frac{1}{4}(1+\xi)(1+\eta) \tag{2.3}$$

$$N_4(\xi,\eta) = \frac{1}{4}(1-\xi)(1+\eta). \tag{2.4}$$

The corresponding shape function derivatives in the local coordinate system become,

$$N_{1,\xi} = \frac{1}{4}(\eta-1) \tag{2.5}$$

$$N_{2,\xi} = \frac{1}{4}(1-\eta) \tag{2.6}$$

$$N_{3,\xi} = \frac{1}{4}(1+\eta) \tag{2.7}$$

$$N_{4,\xi} = \frac{1}{4}(-1-\eta) \tag{2.8}$$

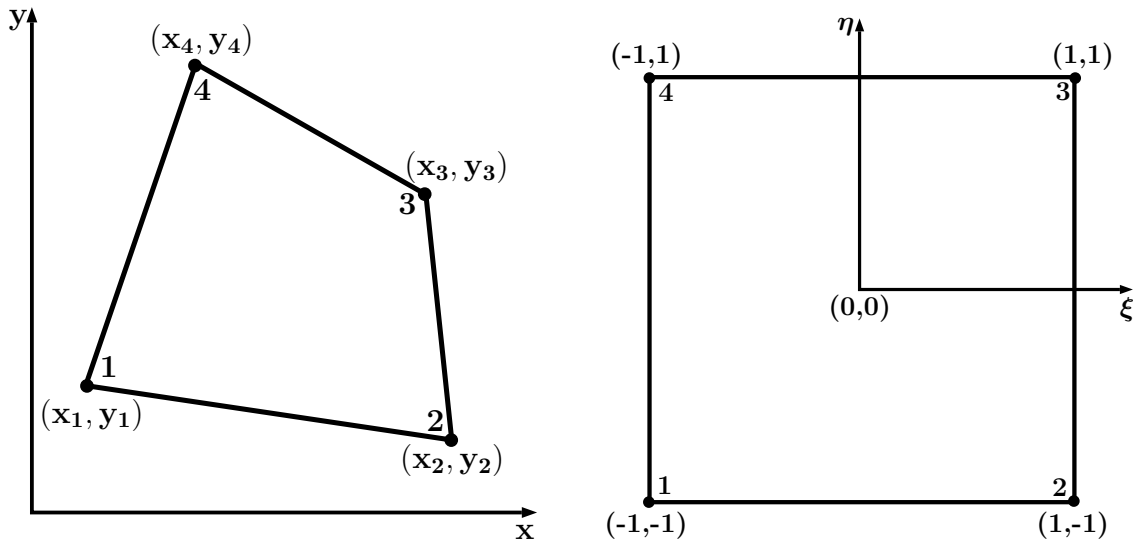

(a) Global Domain (b) Parent Domain

Figure 2.1: Arbitrary 4-node Quadrilateral

$$N_{1,\eta} = \frac{1}{4}(\xi - 1) \tag{2.9}$$

$$N_{2,\eta} = \frac{1}{4}(-1 - \xi) \tag{2.10}$$

$$N_{3,\eta} = \frac{1}{4}(1 + \xi) \tag{2.11}$$

$$N_{4,\eta} = \frac{1}{4}(1 - \xi), \tag{2.12}$$

where the comma in the subscript denotes a partial derivative. The isoparametric representation that maps $\{x, y\}$ based on values of $\{\xi, \eta\}$ is as follows:

$$x = \sum_{i=1}^{4} N_i(\xi, \eta) x_i^e \tag{2.13}$$

$$y = \sum_{i=1}^{4} N_i(\xi, \eta) y_i^e, \tag{2.14}$$

where $\{x_i^e, y_i^e\}$ are the global nodal coordinates. Then the respective derivatives are

$$x_{,\xi} = \sum_{i=1}^{4} N_{i,\xi} x_i^e \tag{2.15}$$

$$y_{,\xi} = \sum_{i=1}^{4} N_{i,\xi} y_i^e \tag{2.16}$$

$$x_{,\eta} = \sum_{i=1}^{4} N_{i,\eta} x_i^e \tag{2.17}$$

$$y_{,\eta} = \sum_{i=1}^{4} N_{i,\eta} y_i^e. \tag{2.18}$$

Similarly, the displacement approximations in the x and y directions in the $\{\xi, \eta\}$ coordinate system can be written respectively as

$$u^h = \sum_{i=1}^{4} N_i(\xi, \eta) u_i \tag{2.19}$$

$$v^h = \sum_{i=1}^{4} N_i(\xi, \eta) v_i, \tag{2.20}$$

where u_i and v_i are the nodal displacements in the x and y directions, respectively. The strain components are

$$e_{xx} = \sum_{i=1}^{4} N_{i,x}(\xi, \eta) u_i \tag{2.21}$$

$$e_{yy} = \sum_{i=1}^{4} N_{i,y}(\xi, \eta) v_i \tag{2.22}$$

$$2e_{xy} = \sum_{i=1}^{4} \left[N_{i,y}(\xi, \eta) u_i + N_{i,x}(\xi, \eta) v_i \right]. \tag{2.23}$$

By writing out $N_{i,\xi}$ and $N_{i,\eta}$ using the chain rule and solving the system of equations for $N_{i,x}$ and $N_{i,y}$ we obtain

$$N_{i,x} = \frac{N_{i,\xi} y_{,\eta} - N_{i,\eta} y_{,\xi}}{J}, \qquad \text{for } \; i = 1..4 \tag{2.24}$$

$$N_{i,y} = \frac{-N_{i,\xi} x_{,\eta} + N_{i,\eta} x_{,\xi}}{J}, \qquad \text{for } \; i = 1..4, \tag{2.25}$$

where J is the determinant of the Jacobian and is written as,

$$J = x_{,\xi} y_{,\eta} - y_{,\xi} x_{,\eta}. \tag{2.26}$$

For simplicity, we evaluate the strain at the center of the element with $\{\xi, \eta\} = \{0, 0\}$. Using eqs. 2.1 through 2.26 for $\xi = \eta = 0$, the resulting strain components e_{xx}, e_{yy}, and e_{xy} become,

$$e_{xx} = \frac{1}{2A}\left[(y_2 - y_4)(u_1 - u_3) + (y_3 - y_1)(u_2 - u_4)\right] \tag{2.27}$$

$$e_{yy} = \frac{1}{2A}\left[(x_4 - x_2)(v_1 - v_3) + (x_1 - x_3)(v_2 - v_4)\right] \tag{2.28}$$

$$e_{xy} = \frac{1}{4A}\left[(x_4 - x_2)(u_1 - u_3) + (x_1 - x_3)(u_2 - u_4)\right] + \frac{1}{4A}\left[(y_2 - y_4)(v_1 - v_3) + (y_3 - y_1)(v_2 - v_4)\right], \tag{2.29}$$

where A is the element area defined as,

$$A = \frac{1}{2}\left[(x_1 - x_3)(y_2 - y_4) + (x_2 - x_4)(y_3 - y_1)\right]. \tag{2.30}$$

It turns out that eq. 2.29 is the most important equation to consider when trying to understand shear locking during mode-I failure. Similarly, for mode-II failure, the normal strain eqs. 2.27 and 2.28 are useful. Next, let's compute the spurious strains that are introduced by both mode-I and mode-II failure.

2.2 Spurious Shear Accumulation

2.2.1 Mode-I Crack

Let's assume that a crack forms in the center of the element with a crack opening displacement of $[[u_n]] = 2\delta$ as shown in Figure 2.2(a). Note that the brackets indicate that u_n is a displacement jump. The crack normal defined by $\mathbf{n}$ is in the $\mathbf{e}_1$ direction as indicated by the local element crack $\{\mathbf{n}, \mathbf{t}\}$ basis in Figure 2.2(a). The

smeared crack approach formalism is applied and the crack opening displacement is represented via a displacement of nodes 1 through 4 such that the element expands by 2δ. The expanded element due to the crack opening is shown in Figure 2.2(b) where the original element geometry is represented by a dotted line. Notice that the nodes only move in the $\mathbf{e}_1$ direction. Because the crack opening is exclusively in the $\mathbf{e}_1$ direction, the nodal displacements in the $\mathbf{e}_2$ are equal to zero, or $v_1 = v_2 = v_3 = v_4 = 0$. One form for the nodal displacements in the normal direction that is consistent with the conventional finite element method for either the stiffness approach or dynamic approach based on nodal forces is that of assuming $u_1 = u_4 = -\delta$, and $u_2 = u_3 = +\delta$. Substituting these displacements into eqs. 2.27 through 2.29, the strains in the element due to the crack denoted e^{cr}_{xx}, e^{cr}_{yy}, and e^{cr}_{xy} simplify to

$$e^{cr}_{xx} = \frac{\delta}{A}\left(y_4 - y_2 + y_3 - y_1\right) \tag{2.31}$$

$$e^{cr}_{yy} = 0 \tag{2.32}$$

$$e^{cr}_{xy} = \frac{\delta}{2A}\left(x_1 - x_4 + x_2 - x_3\right). \tag{2.33}$$

The result shown in eq. 2.33 is the dreaded spurious shear strain contribution due to the crack opening. This parasitic shear strain increases linearly with the crack opening displacement and ultimately spreads across the mesh leading to erroneous load deflection curves. The spurious shear strain becomes zero for the following conditions:

$$\delta = 0 \tag{2.34}$$

$$x_1 - x_4 + x_2 - x_3 = 0. \tag{2.35}$$

The constraint in eq. 2.34 is a kinematic constraint and the constraint in eq. 2.35 is a geometric constraint on the element. Clearly, if there is no crack or $\delta = 0$, then there will be no crack shear strain for any element geometry. However, if there is a crack or $\delta > 0$, then eq. 2.35 must be satisfied to ensure that the shear strain is

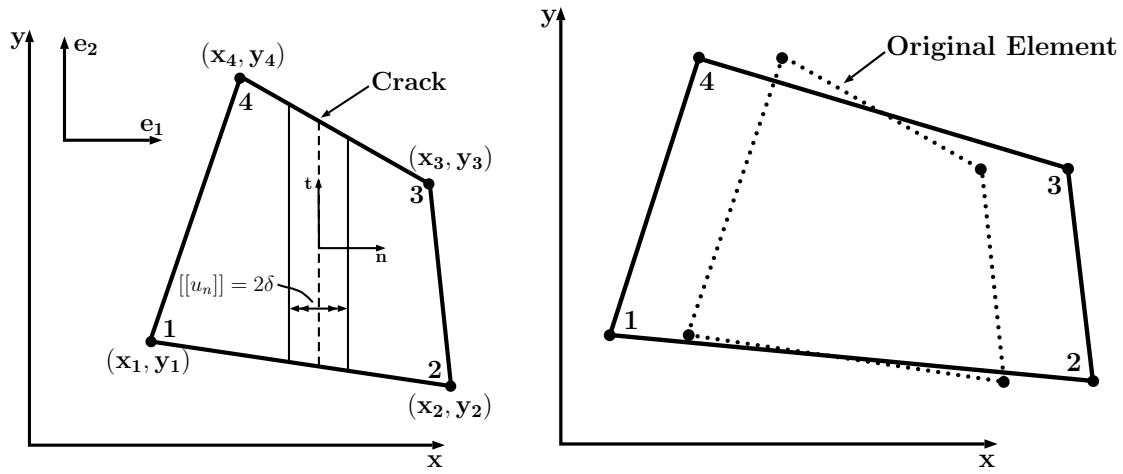

(a) Initiated Crack (b) Cracked Element

Figure 2.2: Cracked 4-node Quadrilateral Element

zero. One particular element geometry that satisfies eq. 2.35 is an element with the edges aligned with the crack surface such that $x_1 = x_4$ and $x_2 = x_3$. However, this is not the only geometry that precludes spurious shear strain. Even for this simple crack problem, there are geometric constraints that must be placed on an element such that spurious shear strain isn't accumulated. Because the crack orientation isn't known a priori, it is not possible to use mesh geometry to preclude spurious shear for general problems. In general, spurious shear will arise in an arbitrary element unless the crack opening displacement is distributed across the nodes in a specific way as shown in Section 2.3.

2.2.2 Mode-II Crack

A similar analysis can be completed for mode-II cracks. Let's consider an initiated crack with the same orientation and element geometry as before. However, now let's introduce a crack in shear with crack opening displacement $[[u_t]] = 2\delta$ in the $\mathbf{t}$ direction as shown in Figure 2.3(a). Applying nodal displacements of $v_1 = v_4 = -\delta$ and $v_2 = v_3 = +\delta$ results in the cracked element shown in Figure 2.3(b). The

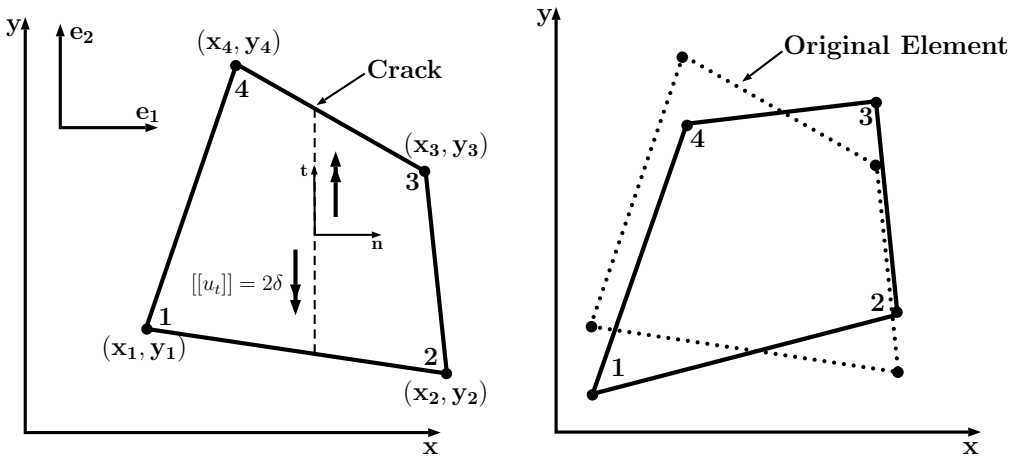

(a) Initiated Crack (b) Cracked Element

Figure 2.3: Cracked 4-node Quadrilateral Element

corresponding strain components are

$$e_{xx}^{cr} = 0 \tag{2.36}$$

$$e_{yy}^{cr} = \frac{\delta}{A}\left(x_2 - x_3 + x_1 - x_4\right) \tag{2.37}$$

$$e_{xy}^{cr} = \frac{\delta}{2A}\left(y_4 - y_2 + y_3 - y_1\right). \tag{2.38}$$

Notice now that from eq. 2.37 a spurious normal strain e_{yy} is obtained. Similar to the mode-I crack, if the element edges are parallel to the crack or $x_1 = x_4$ and $x_2 = x_3$ the spurious normal strain vanishes. Note that if the crack normal $\mathbf{n}$ is rotated counter-clockwise by 90^o, then a spurious normal strain e_{xx} would arise.

2.3 Precluding Spurious Shear

In the previous section, a particular distribution of nodal displacements was used to represent a crack within an element. Recall that a symmetric displacement distribution was applied such that each node was moved equally or $u_1 = u_4 = -\delta$ and $u_2 = u_3 = +\delta$ for a mode-I crack. It was shown that this specific distribution

resulted in spurious shear strain unless certain element geometry constraints were satisfied. Now let's consider another possibility where the nodal displacements due to the crack are computed based on the distance from the element center to the node. The smeared crack approach assumes that an element contains a constant crack strain α located at the element center. The coordinates of the element center $\{x_c, y_c\}$ are computed as follows:

$$x_c = \frac{1}{4}\left(x_1 + x_2 + x_3 + x_4\right) \tag{2.39}$$

$$y_c = \frac{1}{4}\left(y_1 + y_2 + y_3 + y_4\right). \tag{2.40}$$

The nodal displacements due to the crack are computed by integrating the crack strain over the distance from the element center to the node as follows:

$$u_1 = -\alpha\left(x_c - x_1\right) \tag{2.41}$$

$$u_2 = \alpha\left(x_2 - x_c\right) \tag{2.42}$$

$$u_3 = \alpha\left(x_3 - x_c\right) \tag{2.43}$$

$$u_4 = -\alpha\left(x_c - x_4\right). \tag{2.44}$$

At this point, it doesn't matter how we define the crack strain. Substituting in the element coordinates x_c and y_c into eqs. 2.41 through 2.44, we obtain the following nodal displacement distribution for the crack opening,

$$u_1 = \frac{\alpha}{4}\left(3x_1 - x_2 - x_3 - x_4\right) \tag{2.45}$$

$$u_2 = \frac{\alpha}{4}\left(3x_2 - x_1 - x_3 - x_4\right) \tag{2.46}$$

$$u_3 = \frac{\alpha}{4}\left(3x_3 - x_1 - x_2 - x_4\right) \tag{2.47}$$

$$u_4 = \frac{\alpha}{4}\left(3x_4 - x_1 - x_2 - x_3\right). \tag{2.48}$$

Next, the nodal displacement method can be tested by subsituting in eqs. 2.45 through 2.48 into the strain relations eqs. 2.27 to 2.29 resulting in

$$e_{xx}^{cr} = \frac{\alpha}{2A}\left[(y_2 - y_4)(x_1 - x_3) + (y_3 - y_1)(x_2 - x_4)\right] \tag{2.49}$$

$$e_{yy}^{cr} = 0 \tag{2.50}$$

$$e_{xy}^{cr} = 0. \tag{2.51}$$

Upon careful examination of eq. 2.49, it is seen that the bracket in the numerator is equal to $2A$ and as a result, the strains simplify to

$$e_{xx}^{cr} = \alpha \tag{2.52}$$

$$e_{yy}^{cr} = 0 \tag{2.53}$$

$$e_{xy}^{cr} = 0. \tag{2.54}$$

2.4 Concluding Remarks

The results shown in eqs. 2.52 through 2.54 are ideal because the assumed crack strain is obtained while the shear strain is equal to zero. However, eqs. 2.45 through 2.48 represent global nodal displacements. They are essentially kinematic boundary conditions that must be imposed. In a real problem, the nodal displacements due to the crack opening are driven by the unloading of surrounding elements caused by the reduction in stress imposed by equilibrium. As a result, the motion of the cracked element nodes is problem dependent (e.g. where the crack forms). In other words, the nodal displacement distribution shown above, does not satisfy equilibrium in general. As a result, there is an inconsistency between the kinematic conditions imposed to eliminate spurious shear for the cracked element and the kinematic conditions imposed by the equilibrium solution. Another issue is that satisfying the linear crack distribution in one element would violate the linear crack distribution in the neighboring element. This would eventually lead to problems.

Another possibility that was investigated was to alter the distribution of local element nodal forces. However, the resulting form of the assembled global internal force vector was inconsistent with the stress field. For example, for the problem with constant uniaxial stress without body and external forces, the global internal nodal force vector should be zero. However, by redistributing the local element internal forces, the resulting assembled global force vector was nonzero. The next chapter provides an alternative to the standard approach.

Chapter 3

Failure Model

This chapter provides a modification to a conventional failure model for mode-I cracks that precludes spurious shear stress formation in a cracked element. A similar formulation is expected to apply to mode-II failure that would preclude spurious normal stress. The principal differences between the proposed discrete failure model and other failure models is that certain components of the stress are projected out to preclude pollution of the numerical solution due to spurious shear stress. Another important aspect is that the crack orientation is assumed fixed after crack initiation and does not rotate as the crack evolves. Only nonspurious total strain components are selected to update the stress. The total strain components chosen are also consistent with the mode of failure.

First, a chronological overview is provided that may provide insights into the thought processes that led up to the failure model proposed. Next, the layout for a discrete decohesion failure model is presented to provide background. A generalized failure constitutive model is presented next to model mode-I cracks. Finally, constitutive equations are derived for specific linear and nonlinear softening functions. The resulting failure model provides a simple, easily implementable, and computationally efficient means to model mode-I cracks without mesh orientation bias.

3.1 Chronological Review

Initial simulations of a crack forming across a 2D bar with uniaxial stress using a standard decohesion failure model showed that when the element edges were not aligned with the crack surface, the normal stress in the bar was much larger than the stress predicted by the analytical solution. As a result, the computed force in the bar was incorrect. The extent of the error became larger as the element edge angles increased. These results are consistent with results observed by other researchers such as Jirásek and Zimmermann [22].

Initially, the focus was to try to derive a kinematic approach of applying the crack opening displacement across the nodes of the cracked element to preclude spurious shear strain. Several different approaches were tested including redistributing nodal forces to achieve a linear crack opening displacement and applying global nodal displacement boundary conditions for nodes of the cracked element that satisfied the no shear constraint as derived in Chapter 2. Unfortunately, these methods did not work primarily because the kinematic and nodal force constraints imposed were not consistent with the equilibrium solution. In some cases, the numerical method didn't converge or distortions of the stress field resulted.

Over time, it became evident that attempting to correct the kinematics of an element undergoing a crack to preclude spurious shear strain wasn't really working. Instead, enforcing conditions on the stress within the cracked element was much more successful. Eventually, the thinking shifted from kinematics to focusing on the stress within the cracked element. The logic behind this thinking was that one of the roles of the failure model is to reduce the traction in the proper direction as the crack opens. That is, the form of the stress increment should be consistent with the failure model and mode of failure. These thoughts led to a stress increment based failure model that doesn't use strain components that are spurious. Application of this sort of failure model for mode-I cracks essentially precluded mesh orientation bias with

respect to the load-deflection curve as long as the crack was allowed to propagate along element edges.

However, another problem arose. The cracks would follow the column of elements due to the misalignment of the initial stress field around the initiated crack. It was discovered, that this problem was unrelated to spurious shear stress. Even when there was no spurious shear in the solution, the crack direction was still erroneous. These results were also observed by other researchers and led some to use nonlocal models such as the nonlocal damage model in [12] and Oẑbolt and Baẑant [44]. A more direct approach considered here is to use a crack tracking algorithm that propagates the crack based on the failure orientation obtained from the failure model.

Applying a crack tracking algorithm provided the correct crack path, but also led to another problem. For straight cracks propagating through an oriented mesh, a crack cross-over (i. e. a zig-zag pattern) must eventually occur. Once crack cross-overs were generated, this led to a mild shear locking effect that would not allow the cross-over elements to fully unload. This led to mesh orientation bias because as the mesh was rotated, the number of cross-over cracks increased, which led to further errors in the load-deflection curve. It was discovered that when the characteristic crack length was adjusted to account for the total length of the cross-over (typically two elements), then this essentially eliminated the cross-over locking effects observed. Once the appropriate hourglass methods and characteristic crack dimension definitions were implemented into the algorithm, both mesh size and orientation objectivity were obtained.

The chapters that follow will provide the theoretical foundations for the following key components that are required to obtain mesh objectivity: (1) mode-I failure model that precludes spurious shear stress, but does not evolve the crack orientation, (2) crack tracking algorithm that provides the correct crack path, (3) hourglass control for softening, and (4) cross-over scaling to eliminate unloading errors.

3.2 Review of a Standard Decohesion Model

A decohesion model, as defined here, is essentially a cohesive crack model that uses a decohesion function to provide the correct failure stress, failure orientation, fracture energy, and evolution of failure as the crack opens. To achieve all of these features is challenging and quite often not appreciated. For concrete materials undergoing large confining stress, a mode-I failure model is not enough to capture the failure behavior because concrete begins to fail in combined tension and shear, and the orientation of the failure plane changes with confining stress as noted in quasi-static experiments [27]. Much more complicated decohesion models are required to capture the failure behavior of quasi-brittle materials such as the model proposed in [8]. Here, the scope is limited to mode-I fracture for brittle materials such as concrete under very little confining stress. First, the general structure of a failure model is presented based on a general decohesion model that provides the failure orientation, failure stress, fracture energy, and failure evolution.

The model begins with the assumption that the complex process of turning a network of microcracks into a macrocrack occurs along an oriented plane of failure defined by a unit normal vector $\mathbf{n}$ and two unit orthogonal vectors $\mathbf{t}$ and $\mathbf{p}$ defined such that $\mathbf{p} = \mathbf{n} \times \mathbf{t}$, where $\mathbf{p}$ is out of the plane shown in Figure 3.1. The traction is represented by the vector $\boldsymbol{\tau} = \tau_n \mathbf{n} + \tau_t \mathbf{t} + \tau_p \mathbf{p}$ as shown in Figure 3.1(a). The corresponding crack opening displacement vector $[[\mathbf{u}]]$ is shown in Figure 3.1(b) where $[[\mathbf{u}]] = [[u_n]]\mathbf{n} + [[u_t]]\mathbf{t} + [[u_p]]\mathbf{p}$. Here it is assumed that a crack initiates at an orientation defined by $\mathbf{n}$. The crack then evolves as the crack opening displacement $[[\mathbf{u}]]$ increases while the traction $\boldsymbol{\tau}$ decreases. The traction is obtained from the stress as follows:

$$\boldsymbol{\tau} = \boldsymbol{\sigma} \cdot \mathbf{n}. \tag{3.1}$$

A discrete failure model defines the relationship between the forces acting on the crack surface defined by $\boldsymbol{\tau}$ and how far the crack has opened as defined by $[[\mathbf{u}]]$.

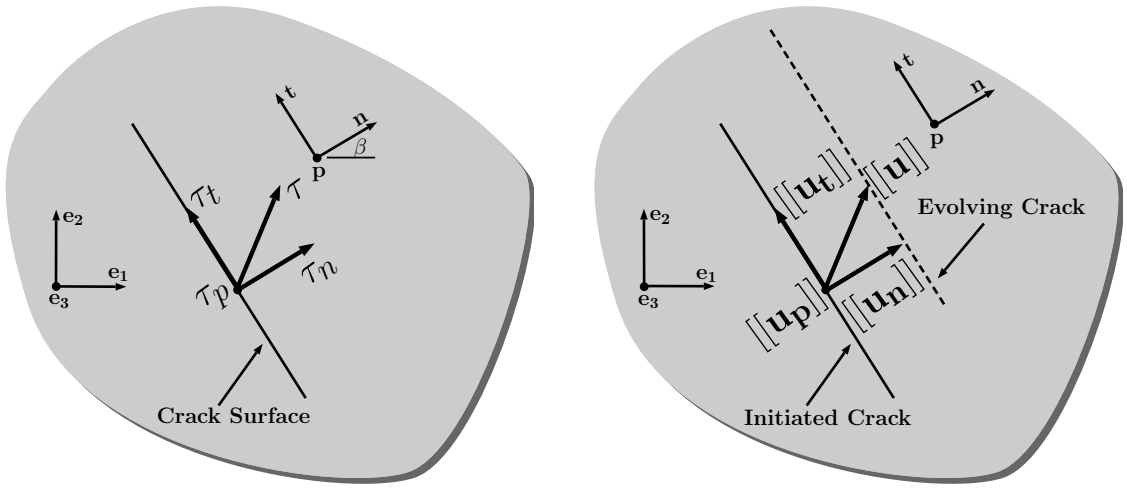

(a) Traction (b) Crack Opening Displacement

Figure 3.1: Failure Model Crack Representation

Mathematically the failure model provides the function $\boldsymbol{\tau} = \boldsymbol{\tau}([[\mathbf{u}]])$. For mode-I failure, the relationship is simplified to $\tau_n = \tau_n([[u_n]])$ with $\tau_t = \tau_p = [[u_t]] = [[u_p]] = 0$. The basis vectors in the crack coordinate system are defined in terms of the global orthonormal basis $\{\mathbf{e_1}, \mathbf{e_2}, \mathbf{e_3}\}$ as

$$\mathbf{n} = n_1\mathbf{e_1} + n_2\mathbf{e_2} + n_3\mathbf{e_3} \tag{3.2}$$

$$\mathbf{t} = t_1\mathbf{e_1} + t_2\mathbf{e_2} + t_3\mathbf{e_3} \tag{3.3}$$

$$\mathbf{p} = p_1\mathbf{e_1} + p_2\mathbf{e_2} + p_3\mathbf{e_3}. \tag{3.4}$$

A transformation matrix $\mathbf{A}$ is used to map the stresses between the global and local basis as follows:

$$[A] = \begin{bmatrix} n_1 & t_1 & p_1 \\ n_2 & t_2 & p_2 \\ n_3 & t_3 & p_3 \end{bmatrix}. \tag{3.5}$$

The stress in the crack basis $\boldsymbol{\sigma^{cr}}$ is computed using $\mathbf{A}$ and the stress in the global basis $\boldsymbol{\sigma}$ with

$$\boldsymbol{\sigma^{cr}} = \mathbf{A}^T\boldsymbol{\sigma}\mathbf{A}. \tag{3.6}$$

Similarly, the stress in the global basis is computed from the stress in the crack basis with

$$\boldsymbol{\sigma} = \mathbf{A}\boldsymbol{\sigma}^{\boldsymbol{cr}}\mathbf{A}^T. \tag{3.7}$$

The components of $\mathbf{A}$ are computed by finding the crack normal $\mathbf{n}$ that maximizes the value of the decohesion function. Some examples of decohesion functions are

$$F^{TR} = \frac{\sqrt{\tau_t^2}}{\tau_{sf}} - f_s, \qquad \text{(Tresca)} \tag{3.8}$$

$$F^{R} = \frac{\tau_n}{\tau_{nf}} - f_s, \qquad \text{(Rankine)} \tag{3.9}$$

$$F^{MC} = \frac{\sqrt{\tau_t^2}}{\tau_{sf}^*} + \frac{\tau_n}{\tau_{nf}^*} - f_s, \qquad \text{(Mohr} - \text{Coulomb)}, \tag{3.10}$$

where τ_{sf} is the shear strength for Tresca, τ_{nf} is the tensile strength of the material for Rankine, τ_{sf}^*, τ_{nf}^*, are material parameters used for Mohr-Coulomb formulation, and f_s is a softening function used to incorporate softening, fracture energy, and failure evolution. When the crack initiates, $[[\mathbf{u}]] = \mathbf{0}$ and $f_s = 1$. Once the crack opening displacement reaches u_0, the crack is traction free and $f_s = 0$. To predict the failure stress and failure orientation, the decohesion function with $f_s = 1$ is used. The Tresca decohesion function is primarily used for metals that fail due to shear along 45^o failure planes with respect to the direction maximum of principal stress. The Rankine decohesion function is used for brittle materials that fail due to loss of cohesion in tension where the crack normal is in the direction of the most tensile principal stress. The Mohr-Coulomb (MC) decohesion function has been used to model quasi-brittle materials where the shearing action is dependent on the extent of normal traction on the failure plane.

To compute the failure angle, the decohesion function is first expressed in terms of the principal stresses and failure angle β (see Figure 3.1(a)). A Newton solver, when an analytical solution isn't available, can be used to find at what value of β $\partial F/\partial\beta = 0$ is satisfied. A closed form solution to find β may exist when the failure angle doesn't depend on the state of stress. As an example, the decohesion functions

provided earlier are expressed as functions of the principal stress and failure angle β below.

$$F^{TR} = \frac{\sqrt{(1-\gamma)\gamma}(\sigma_{max} - \sigma_{min})}{\tau_{sf}} - 1, \qquad \text{(Tresca)} \quad (3.11)$$

$$F^{R} = \frac{(1-\gamma)\sigma_{min} + \gamma\sigma_{max}}{\tau_{nf}} - 1, \qquad \text{(Rankine)} \quad (3.12)$$

$$F^{MC} = \frac{\sqrt{(1-\gamma)\gamma(\sigma_{max} - \sigma_{min})^2}}{\tau_{sf}} + \frac{(1-\gamma)\sigma_{min} + \gamma\sigma_{max}}{\tau_{nf}} - 1, \qquad \text{(MC)}, \quad (3.13)$$

where $\gamma = \sin^2(\beta)$ and σ_{max} and σ_{min} are maximum and minimum principal stresses, respectively. None of the failure models above provide a failure angle that is dependent on the state of stress. The crack normal for the Tresca and Rankine failure models is always 45 and 0^o, respectively, with respect to the direction of maximum principal stress. The failure orientation for a Mohr-Coulomb material is dependent on the *shear* and *tensile* strengths. The decohesion models above have an analytical

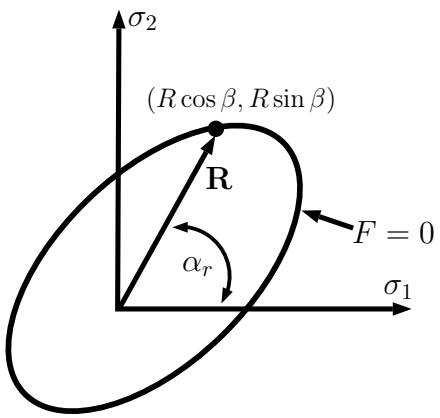

Figure 3.2: Failure Surface

solution for the failure angle as follows:

$$\gamma^{TR} = \frac{1}{2} \Rightarrow \beta^{TR} = \pm\frac{\pi}{4} = \pm 45^o, \qquad \text{(Tresca)} \quad (3.14)$$

$$\gamma^{R} = 0, 1 \Rightarrow \beta^{R} = 0, \frac{\pi}{2} = 0, 90^o, \qquad \text{(Rankine)} \quad (3.15)$$

$$\gamma^{MC} = \frac{\tau_{nf}^2 + \tau_{sf}^2 \pm \sqrt{\tau_{sf}^4 + \tau_{sf}^2 \tau_{nf}^2}}{2(\tau_{nf}^2 + \tau_{sf}^2)} \Rightarrow \beta^{MR} = \sin^{-1}\left(\pm\sqrt{\gamma^{MR}}\right), \qquad \text{(MC)}. \quad (3.16)$$

In order to fit a decohesion model to experimental data, the failure surface defined by the locus of points satisfying $F = 0$ where $F = \max F_n \; \forall \; \mathbf{n}$ must be extracted from the decohesion function F_n. Because the failure surface is commonly expressed in $\sigma_{max} - \sigma_{min}$ space, it is convenient to transform the principal stresses into polar cooordinates as follows:

$$\sigma_1 = R\cos(\alpha_r) \quad (3.17)$$

$$\sigma_2 = R\sin(\alpha_r), \quad (3.18)$$

where R is the length of a vector $\mathbf{R}$ extending to the failure surface and α_r is the angle from the σ_1 axis as shown in Figure 3.2. The failure surface is then mapped out by incrementing R and for each increment the failure angle β is computed numerically using Newton's method. The radius R is incremented until the value of the function F is positive at which point the values of σ_1 and σ_2 are computed from eqs. 3.17 and 3.18. This is repeated for remaining increments in the polar angle α_r for $0 \leq \alpha_r \leq 2\pi$ such that enough points are generated to plot a failure surface such as that shown in Figure 3.2 for plane stress. Note that for some segments, σ_{max} and σ_{min} are zero. Decohesion function parameters are then optimized to minimize an error function that compares the failure surface to experimental data.

The total fracture energy W_f per unit of area that considers all modes of failure is computed by integrating the product of the tractions and the crack opening displacement rates over time as follows:

$$W_f = \int_0^t \{\tau_t[[\dot{u_t}]] + \tau_n[[\dot{u_n}]] + \tau_p[[\dot{u_p}]]\}dt. \quad (3.19)$$

The corresponding fracture energy for mode-I failure incorporating u_0 is,

$$G_{f_I} = \int_0^{u_0} \tau_n [[du_n]]. \tag{3.20}$$

The softening function parameters are chosen such that the correct fracture energy is obtained. Quite often u_0 and the shape of the softening function are adjusted to obtain the correct fracture energy. For simplicity, often a linear softening function is used.

The remaining feature of the decohesion model is the mechanism to evolve the failure surface as the material softens. A decohesion model is formulated as an analogy to rate independent plasticity where the decohesion function is analogous to the yield function, the crack opening displacement vector is analogous to the plastic strain tensor, and the traction is analogous to the stress tensor. Assuming an associated failure rule, the crack opening displacement vector evolves as,

$$[[\dot{\boldsymbol{u}}]] = \dot{\omega} \frac{\partial F}{\partial \boldsymbol{\tau}}, \tag{3.21}$$

where $\dot{\omega}$ is a positive monotonically increasing function and is determined from the consistency condition.

$$\dot{F} = 0. \tag{3.22}$$

The components of $[[\dot{\boldsymbol{u}}]]$ follow from eq. 3.21:

$$[[\dot{u_n}]] = \dot{\omega} \frac{\partial F}{\partial \tau_n} \tag{3.23}$$

$$[[\dot{u_t}]] = \dot{\omega} \frac{\partial F}{\partial \tau_t} \tag{3.24}$$

$$[[\dot{u_p}]] = \dot{\omega} \frac{\partial F}{\partial \tau_p}. \tag{3.25}$$

The decohesion model is activated if $F_{max} > 0$ at which point the value of the increment in crack opening displacement is computed such that $F_{max} \approx 0$, where F_{max} is defined as the largest value of the decohesion function F obtained over the space of all possible orientations $\mathbf{n}$.

The remaining part of the formulation shows how to incorporate the decohesion model into a continuum representation. An additive decomposition is applied where the total strain $\mathbf{e}$ consists of an elastic strain $\mathbf{e^e}$ and an inelastic strain, denoted the crack strain $\mathbf{e^{cr}}$, as follows:

$$\mathbf{e} = \mathbf{e^e} + \mathbf{e^{cr}}. \tag{3.26}$$

The crack strain is computed by casting the crack opening displacement over a characteristic length L_c. Recall that the fracture energy is dissipated within a finite region to avoid numerical issues. This finite region has a dimension equal to L_c. Because we want the crack band to consist of a width of a single element, L_c is on the order of the element size h. Generally, the crack strain is computed from

$$\mathbf{e^{cr}} = \frac{1}{L_c}\{[[\mathbf{u}]] \otimes \mathbf{n}\}^{\mathrm{S}}, \tag{3.27}$$

where the superscript S indicates that the symmetric part of the tensor is taken. Note that a more thorough formalism is introduced in Chapter 4 for handling strong discontinuities. The stress is evaluated using the elastic part of the strain as follows,

$$\boldsymbol{\sigma} = \mathbb{E} : \mathbf{e^e} = \mathbb{E} : (\mathbf{e} - \mathbf{e^{cr}}), \tag{3.28}$$

where $\mathbb{E}$ is the fourth order elasticity tensor. What is important to note is that smeared crack methods have in the past used the formalism of eq. 3.28 to compute the stress. However, using all strain components in $\mathbf{e}$ to compute the stress, results in spurious shear stress because as we know from Chapter 2, a spurious shear strain arises within the total strain $\mathbf{e}$ when a mode-I crack is opened in a finite element. Now let's formulate a modification to the standard decohesion model that provides a way to model mode-I cracks without introducing spurious shear stress in the cracked element.

3.3 Failure Model

The key idea behind the failure model is to update the stress in the cracked element without introducing spurious shear stress components. This generally can be considered as a new method for numerically implementing the constitutive equation. Certain components of the stress are projected out to preclude pollution of the numerical solution due to spurious shear stress. Another important aspect is that the crack orientation is assumed fixed after crack initiation and does not rotate as is assumed in the rotating crack model. This allows the actual physical crack path to be predicted more accurately. First, the generalized constitutive equations will be derived for mode-I failure that are applicable to a general softening function. The remaining sections will provide the specific equations for both linear and nonlinear softening.

3.3.1 Generalized Constitutive Equations

In Section 2.2.1, it was demonstrated that opening a crack in mode-I introduces a spurious shear strain within the total strain tensor $\mathbf{e}$. For a mode-II crack opening, a similar analysis showed that spurious normal strains arise. The standard smeared crack approach that provides a continuum representation of a crack assumes that the total strain is additively decomposed into an elastic strain $\mathbf{e}^e$ and a crack strain $\mathbf{e}^{cr}$ as follows:

$$\mathbf{e} = \mathbf{e}^e + \mathbf{e}^{cr}. \tag{3.29}$$

The stress in the cracked material is then updated using the elastic strain determined from eq. 3.29 and Hooke's law as

$$\boldsymbol{\sigma}^{cr} = \mathbb{E} : \mathbf{e}^e = \mathbb{E} : (\mathbf{e} - \mathbf{e}^{cr}) . \tag{3.30}$$

Applying the formalism of eq. 3.30 causes spurious shear stress to accumulate in elements that contain a crack strain because of the spurious shear strain component

appearing in the total strain $\mathbf{e}$. For example, in a mode-I crack, the crack shear strain component in the local crack basis $e_{nt}^{cr} = 0$ because the crack opening displacement is exclusively in the $\mathbf{n}$ direction. However, upon opening a crack, the total strain component e_{nt} is non-zero and spurious as derived in Section 2.2.1. As a result, the elastic shear strain component $e_{nt}^{e} = e_{nt} - e_{nt}^{cr}$ will be nonzero and this will result in a nonzero spurious shear stress component σ_{nt}. This spurious shear stress component will then accumulate with the crack opening displacement and will ultimately cause spurious shear stress transfer across the mesh or shear locking resulting in erroneous load-deflection curves and crack paths. If the crack surface is parallel to the element edges, then during a mode-I crack opening, $e_{nt} = e_{nt}^{cr} = 0$ and as a result $\sigma_{nt} = 0$. However, this situation in general cannot be assumed if failure at an angle through a mesh is of interest as is the focus of this dissertation. Therefore, another approach is required.

From the onset, we will seek a relationship between how the stress in the cracked element changes with a change in the total strain $\mathbf{e}$ that is consistent with the mode of failure and does not introduce spurious stress components. As mentioned in Chapter 1, the dissertation research is focused on modeling cracks that are formed in brittle materials when the material is loaded in tension. The failure mechanism is predominately due to loss of cohesion and during the failure process the material cannot sustain much shear loading along the crack surface. For this reason we assume that during the crack evolution the rate of shear stress in the local crack basis is approximately zero. As a result, we state the functional forms of the constitutive equations that govern the failure model as follows:

$$\dot{\sigma}_{nn} \equiv \dot{\sigma}_{nn}\left(\dot{e}_{nn}, \dot{e}_{tt}\right) \tag{3.31}$$

$$\dot{\sigma}_{tt} \equiv \dot{\sigma}_{tt}\left(\dot{e}_{nn}, \dot{e}_{tt}\right) \tag{3.32}$$

$$\dot{\sigma}_{nt} \equiv 0 \tag{3.33}$$

where the superscript cr on $\dot{\sigma}_{nn}$, $\dot{\sigma}_{tt}$, and $\dot{\sigma}_{nt}$ have been dropped for convenience.

Let's also make a strong statement as to what the stresses will not depend on to alleviate any confusion as follows:

$$\dot{\sigma}_{nn} \not\equiv \dot{\sigma}_{nn}\left(\dot{e}_{nt}\right) \tag{3.34}$$

$$\dot{\sigma}_{tt} \not\equiv \dot{\sigma}_{tt}\left(\dot{e}_{nt}\right) \tag{3.35}$$

$$\dot{\sigma}_{nt} \not\equiv \dot{\sigma}_{nt}\left(\dot{e}_{nt}\right). \tag{3.36}$$

By stating eqs. 3.34 through 3.36, the condition of spurious free stress in a cracked element is enforced for the specific finite element formulation and specific finite element used. These same equations cannot be stated until a spurious strain analysis has been conducted for the specific finite element formulation and specific element.

The fundamental difference between the proposed failure model and the equations of the standard smeared crack approach is that the total shear strain rate $\dot{e}_{nt}$ is never used to compute the stress in the proposed model. The proposed approach doesn't require $\dot{e}_{nt}$ because the accumulation of shear stress in the local crack basis isn't allowed or $\dot{\sigma}_{nt} = 0$. Kinematically, this is equivalent to allowing the crack shear strain rate to evolve such that the elastic shear strain rate is zero or that the shear crack strain rate is equivalent to the total shear strain rate or $\dot{e}^{cr}_{nt} = \dot{e}_{nt}$. Also, note that the rates can be removed and that the same statements hold for the actual strain measure, that is to say $e^{cr}_{nt} = e_{nt}$.

The first step is to develop a decohesion function for the material of interest. As mentioned previously, for modeling mixed mode failure in concrete requires advanced models [8, 45] that depend on all three traction components. However, for modeling brittle materials such as concrete under little confining stress, a Rankine failure model suffices as follows:

$$F = \frac{\tau_n}{\tau_{nf}} - f_s = \frac{\sigma_{nn}}{\tau_{nf}} - f_s, \tag{3.37}$$

where f_s is the softening function and τ_{nf} is the tensile strength. The failure orientation was provided in the previous section where $\mathbf{n}$ is always aligned with the direction of most tensile principal stress.

Next, we must define explicitly the stress rate functions which describe how the stress components change in time. It is convenient to transform the stress tensor that defines the stress in the cracked material to a vector form that can be more readily applied in the finite element formulation. Here we invoke the plane stress or strain assumption which leads to a rate form of the elastic constitutive equation in matrix form as follows:

$$\begin{Bmatrix} \dot{\sigma}_{nn} \\ \dot{\sigma}_{tt} \\ \dot{\sigma}_{nt} \end{Bmatrix} = \begin{bmatrix} C_{11} & C_{12} & 0 \\ C_{12} & C_{22} & 0 \\ 0 & 0 & C_{33} \end{bmatrix} \begin{Bmatrix} \dot{e}^{e}_{nn} \\ \dot{e}^{e}_{tt} \\ 0 \end{Bmatrix}, \tag{3.38}$$

where C_{11}, C_{22}, and C_{33} are elastic constants that depend on which planar assumption is made and will be defined in Section 4.2.2. Next, we apply the smeared crack formalism of eq. 3.29. Note that there is only a crack opening displacement in the **n** direction. As a result, $e^{cr}_{tt} = 0$ and therefore $e_{tt} = e^{e}_{tt}$. The stress rate equations then become

$$\begin{Bmatrix} \dot{\sigma}_{nn} \\ \dot{\sigma}_{tt} \\ \dot{\sigma}_{nt} \end{Bmatrix} = \begin{bmatrix} C_{11} & C_{12} & 0 \\ C_{12} & C_{22} & 0 \\ 0 & 0 & 0 \end{bmatrix} \begin{Bmatrix} \dot{e}_{nn} - \dot{e}^{cr}_{nn} \\ \dot{e}_{tt} \\ 0 \end{Bmatrix}. \tag{3.39}$$

Carrying out the matrix-vector product of eq. 3.39 results in the following explicit stress rate functions

$$\dot{\sigma}_{nn} = C_{11}\left(\dot{e}_{nn} - \dot{e}^{cr}_{nn}\right) + C_{12}\dot{e}_{tt} \tag{3.40}$$

$$\dot{\sigma}_{tt} = C_{12}\left(\dot{e}_{nn} - \dot{e}^{cr}_{nn}\right) + C_{22}\dot{e}_{tt} \tag{3.41}$$

$$\dot{\sigma}_{nt} = 0 \tag{3.42}$$

Note that we assume that the material is isotropic and as a result the elastic constants will remain the same for the global and local crack bases. We now require an equation for the crack strain rate $\dot{e}^{cr}_{nn}$. We apply the rate form of the strong discontinuity eq. 3.27 with $\langle \dot{u} \rangle = \langle \dot{u}_n, 0, 0 \rangle$, $\langle n \rangle = \langle 1, 0, 0 \rangle$, and $L_c = h_c$ resulting in,

$$\dot{e}^{cr}_{nn} = \frac{\dot{u}_n}{h_c}. \tag{3.43}$$

Note that the [[ ]] has been dropped on u_n for convenience. The characteristic element size h_c is defined as,

$$h_c = \frac{h}{\cos\beta}, \qquad -\frac{\pi}{4} \leq \beta \leq \frac{\pi}{4} \tag{3.44}$$

$$h_c = \frac{h}{\sin\beta}, \qquad \frac{\pi}{4} \leq \beta \leq \frac{3\pi}{4}, \tag{3.45}$$

where β is the orientation of $\mathbf{n}$ as shown in Figure 3.1(a) and $h = \sqrt{A}$ where A is the element area. The derivation of the failure model will be kept general in terms of differential functions. As a result, the functional dependencies must be known to establish which time derivatives to take. We note the variables in F that depend on time are as follows:

$$F = F\left(\sigma_{nn}, f_s\right). \tag{3.46}$$

Next, the variables that depend on time in F are identified i. e. σ_{nn}, f_s, and u_n:

$$\sigma_{nn} = \sigma_{nn}\left(e_{nn}, e^{cr}_{nn}, e_{tt}\right) \tag{3.47}$$

$$f_s = f_s\left(u_n\right) \tag{3.48}$$

$$u_n = u_n\left(e_{nn}\right). \tag{3.49}$$

It is hopefully clear at this point that we have not assumed a specific decohesion or softening function. All that we have assumed is what variables each function depends on. We have also assumed a specific relationship between the strain rates and stress rate acting normal to the crack as defined in eq. 3.40.

The objective now is to differentiate F with respect to time considering the functional dependencies defined previously to obtain $\dot{F}$. The consistency condition $\dot{F} = 0$ is then applied to obtained the relationship between the crack strain rate and the total strain rates acting normal and tangential to the crack or we seek $\dot{e}^{cr}_{nn} = \dot{e}^{cr}_{nn}\left(\dot{e}_{nn}, \dot{e}_{tt}\right)$. We will then substitute this result into eq. 3.40. Taking the time derivative of a notional decohesion function F using eq. 3.46 results in

$$\dot{F} = \frac{\partial F}{\partial \sigma_{nn}}\dot{\sigma}_{nn} + \frac{\partial F}{\partial f_s}\dot{f}_s. \tag{3.50}$$

Next, we apply the functional dependencies of σ_{nn} and f_s shown in eqs. 3.47 and 3.48 to define their time derivatives as follows:

$$\dot{\sigma}_{nn} = \frac{\partial \sigma_{nn}}{\partial e_{nn}} \dot{e}_{nn} + \frac{\partial \sigma_{nn}}{\partial e^{cr}_{nn}} \dot{e}^{cr}_{nn} + \frac{\partial \sigma_{nn}}{\partial e_{tt}} \dot{e}_{tt} \tag{3.51}$$

$$\dot{f}_s = \frac{\partial f_s}{\partial u_n} \dot{u}_n \tag{3.52}$$

$$\dot{u}_n = \frac{\partial u_n}{\partial e^{cr}_{nn}} \dot{e}^{cr}_{nn}. \tag{3.53}$$

Using eqs. 3.51 through 3.53 with eq. 3.50 results in the final form for $\dot{F}$

$$\dot{F} = \frac{\partial F}{\partial \sigma_{nn}} \left(\frac{\partial \sigma_{nn}}{\partial e_{nn}} \dot{e}_{nn} + \frac{\partial \sigma_{nn}}{\partial e^{cr}_{nn}} \dot{e}^{cr}_{nn} + \frac{\partial \sigma_{nn}}{\partial e_{tt}} \dot{e}_{tt} \right) + \frac{\partial F}{\partial f_s} \frac{\partial f_s}{\partial u_n} \frac{\partial u_n}{\partial e^{cr}_{nn}} \dot{e}^{cr}_{nn}. \tag{3.54}$$

Collecting like terms for $\dot{e}^{cr}_{nn}$, $\dot{e}^{cr}_{tt}$, and $\dot{e}_{nn}$ results in a simplified form for $\dot{F}$

$$\dot{F} = \frac{\partial F}{\partial \sigma_{nn}} \frac{\partial \sigma_{nn}}{\partial e_{nn}} \dot{e}_{nn} + \frac{\partial F}{\partial \sigma_{nn}} \frac{\partial \sigma_{nn}}{\partial e_{tt}} \dot{e}_{tt} + \left(\frac{\partial F}{\partial \sigma_{nn}} \frac{\partial \sigma_{nn}}{\partial e^{cr}_{nn}} + \frac{\partial F}{\partial f_s} \frac{\partial f_s}{\partial u_n} \frac{\partial u_n}{\partial e^{cr}_{nn}} \right) \dot{e}^{cr}_{nn}. \tag{3.55}$$

Next, applying the consistency condition $\dot{F} = 0$ and solving for $\dot{e}^{cr}_{nn}$ results in one of our objectives of finding $\dot{e}^{cr}_{nn} = \dot{e}^{cr}_{nn}\left(\dot{e}_{nn}, \dot{e}_{tt}\right)$ as follows:

$$\dot{e}^{cr}_{nn} = \frac{\Psi_n}{\Psi} \dot{e}_{nn} + \frac{\Psi_t}{\Psi} \dot{e}_{tt}, \tag{3.56}$$

where Ψ_n, Ψ_t, and Ψ are defined as

$$\Psi_n = -\frac{\partial F}{\partial \sigma_{nn}} \frac{\partial \sigma_{nn}}{\partial e_{nn}} \tag{3.57}$$

$$\Psi_t = -\frac{\partial F}{\partial \sigma_{nn}} \frac{\partial \sigma_{nn}}{\partial e_{tt}} \tag{3.58}$$

$$\Psi = \frac{\partial F}{\partial \sigma_{nn}} \frac{\partial \sigma_{nn}}{\partial e^{cr}_{nn}} + \frac{\partial F}{\partial f_s} \frac{\partial f_s}{\partial u_n} \frac{\partial u_n}{\partial e^{cr}_{nn}}. \tag{3.59}$$

Finally, substituting eqs. 3.56 through 3.59 into eqs. 3.40 and 3.41 results in the stress rate functions that we originally set out to discover as follows:

$$\dot{\sigma}_{nn} = C_{11}\left(1 - \Psi^*_n\right)\dot{e}_{nn} + \left(C_{12} - C_{11}\Psi^*_t\right)\dot{e}_{tt} \tag{3.60}$$

$$\dot{\sigma}_{tt} = C_{12}\left(1 - \Psi^*_n\right)\dot{e}_{nn} + \left(C_{22} - C_{12}\Psi^*_t\right)\dot{e}_{tt} \tag{3.61}$$

$$\dot{\sigma}_{nt} = 0, \tag{3.62}$$

where Ψ_n^* and Ψ_t^* are

$$\Psi_n^* = \Psi_n/\Psi \tag{3.63}$$

$$\Psi_t^* = \Psi_t/\Psi. \tag{3.64}$$

In order to update the stress in a numerical procedure, the incremental form of the governing equations are more useful. Also, putting the constitutive equations in matrix form provides the tangent crack stiffness matrix. The incremental matrix form of eqs. 3.60 through 3.62 for the failure model becomes,

$$\begin{Bmatrix} \Delta\sigma_{nn} \\ \Delta\sigma_{tt} \\ \Delta\sigma_{nt} \end{Bmatrix} = \begin{bmatrix} C_{11}\left(1-\Psi_n^*\right) & \left(C_{12}-C_{11}\Psi_t^*\right) & 0 \\ C_{12}\left(1-\Psi_n^*\right) & \left(C_{22}-C_{12}\Psi_t^*\right) & 0 \\ 0 & 0 & 0 \end{bmatrix} \begin{Bmatrix} \Delta e_{nn} \\ \Delta e_{tt} \\ 0 \end{Bmatrix}. \tag{3.65}$$

The tangent crack stiffness contained in the 3x3 matrix of eq. 3.65 can be applied to derive hourglass forces for the softening element for use in a one-point Gauss quadrature scheme as detailed in Section 4.3.2. Note that the crack tangent stiffness matrix is symmetric even though it appears otherwise.

Next, we must consider the conditions imposed on the normal stress rate $\dot{\sigma}_{nn}$. For a positive increment of total strain normal to the crack e_{nn}, a reduction of σ_{nn} must be enforced. Finally, we must ensure that the stress rates remain bounded or $\Psi \neq 0$. With these statements and using eqs. 3.60 and 3.61 the following conditions must be satisfied

$$\Psi_n^* > 1 \tag{3.66}$$

$$\Psi \neq 0. \tag{3.67}$$

The stress is updated by adding the current stress increments to the stress at the previous increment as follows:

$$\{\sigma^{cr}\}^{n+1} = \{\sigma^{cr}\}^n + \{\Delta\sigma^{cr}\}^{n+1}, \tag{3.68}$$

where $\{\Delta\sigma^{cr}\}^{n+1}$ is updated using eq. 3.65. The crack opening displacement increment Δu_n is computed by substituting in the incremental form of eq. 3.56 into the incremental form of eq. 3.53 with use of eqs. 3.63 and 3.64 as follows:

$$\Delta u_n = \frac{\partial u_n}{\partial e^{cr}_{nn}} \Delta e^{cr}_{nn} = h_c \Delta e^{cr}_{nn} = h_c \left(\Psi^*_n \Delta e_{nn} + \Psi^*_t \Delta e_{tt} \right). \tag{3.69}$$

The current crack opening displacement is then updated by adding the current crack opening displacement increment to the previous crack opening displacement with

$$u^{n+1}_n = u^n_n + \Delta u^{n+1}_n. \tag{3.70}$$

In summary, we have assumed a specific form for the decohesion function that is consistent with mode-I failure or failure that depends on the traction normal to the crack surface. A representation for the crack strain was also assumed that depends on the crack opening u_n and the characteristic element size h_c. However, the form for the softening function was kept general. A set of constitutive equations were then derived to update the crack opening displacement and stress components. Next, let's derive specific equations for both linear and nonlinear softening functions.

3.3.2 Linear Softening

Now we assume specific decohesion and softening functions for a brittle material undergoing mode-I failure. It turns out that only an update for Ψ is required if a different softening function is assumed. As a result, there is no change to Ψ_n or Ψ_t required from Section 3.3. The complete set of specific equations that are required to derive the specific Ψ_n, Ψ_t, and Ψ are

$$\sigma_{nn} = C_{11} \left(e_{nn} - e^{cr}_{nn} \right) + C_{12} e_{tt} \tag{3.71}$$

$$F = \frac{\sigma_{nn}}{\tau_{nf}} - f^l_s \tag{3.72}$$

$$f^l_s = 1 - \frac{u_n}{u_0} \tag{3.73}$$

$$e^{cr}_{nn} = \frac{u_n}{h_c} \rightarrow u_n = e^{cr}_{nn} h_c. \tag{3.74}$$

Note that the superscript l on f_s^l represents the linear softening function. The softening function decays starting from one at $u_n = 0$ to zero at $u_n = u_0$, where u_0 is the crack opening displacement when $\tau_n = 0$. Next, the differentials in Ψ_n, Ψ_t, and Ψ can be defined using the specific eqs. 3.71 through 3.74 of the failure model as follows:

$$\frac{\partial F}{\partial \sigma_{nn}} = \frac{1}{\tau_{nf}} \tag{3.75}$$

$$\frac{\partial \sigma_{nn}}{\partial e_{nn}} = C_{11} \tag{3.76}$$

$$\frac{\partial \sigma_{nn}}{\partial e_{tt}} = C_{12} \tag{3.77}$$

$$\frac{\partial \sigma_{nn}}{\partial e_{nn}^{cr}} = -C_{11} \tag{3.78}$$

$$\frac{\partial F}{\partial f_s^l} = -1 \tag{3.79}$$

$$\frac{\partial f_s^l}{\partial u_n} = -\frac{1}{u_0} \tag{3.80}$$

$$\frac{\partial u_n}{\partial e_{nn}^{cr}} = h_c. \tag{3.81}$$

Substituting eqs. 3.75 through 3.81 into eqs. 3.57 through 3.59 and simplifying we obtain the specific form of Ψ_n, Ψ_t, and Ψ for linear softening as follows:

$$\Psi_n = -\frac{C_{11}}{\tau_{nf}} \tag{3.82}$$

$$\Psi_t = -\frac{C_{12}}{\tau_{nf}} \tag{3.83}$$

$$\Psi^l = \frac{h_c}{u_0} - \frac{C_{11}}{\tau_{nf}}, \tag{3.84}$$

where the superscript l in Ψ^l represents Ψ for linear softening. Next, we apply the constraints imposed in eqs. 3.66 and 3.67 as follows:

$$\Psi_n^* = \frac{\Psi_n}{\Psi^l} > 1 \rightarrow \frac{h_c}{u_0} > 0 \tag{3.85}$$

$$\Psi^l \neq 0 \rightarrow 1 - \frac{\tau_{nf} h_c}{C_{11} u_0} > 0 \rightarrow h_c < \frac{C_{11} u_0}{\tau_{nf}}. \tag{3.86}$$

The constraint in eq. 3.85 is always satisfied because all of the parameters are assumed positive. As a result, a negative stress increment will always arise. Finally, the constraint imposed on the element size h_c is a result of precluding snapback and is a common result. The constraint imposed on the element size can also be expressed in terms of the fracture energy due to the specific softening function used. The fracture energy is determined by integrating $\tau_n = \tau_n(u_n)$ over the interval $[0, u_0]$ as follows:

$$G_{f_I} = G_f = \int_0^{u_0} \tau_n du_n = \int_0^{u_0} \tau_{nf} f_s^l du_n = \frac{1}{2} u_0 \tau_{nf}. \tag{3.87}$$

Because G_f and τ_{nf} are considered material properties, we can estimate u_0 if the fracture energy is known with

$$u_0 = \frac{2G_f}{\tau_{nf}}. \tag{3.88}$$

Subsituting in eq. 3.88 into the constraint on the element size in eq. 3.86 we obtain

$$h_c < \frac{2C_{11}G_f}{\tau_{nf}^2}. \tag{3.89}$$

Once eqs. 3.82 through 3.84 are substituted into eqs. 3.65 and 3.69, the updates for the crack opening displacement and the stress components become explicit with application of eqs. 3.68 and 3.70. Next, let's consider a failure model that uses a nonlinear softening function.

3.3.3 Nonlinear Softening

A linear softening function is useful for investigating the performance of the algorithm in mode-I model problems (see Section 5.2) because the resulting slope of the load-deflection curve is constant. This allows convenient study of mesh orientation bias and convergence. However, the shape of the load-deflection curve in some experiments (see Section 5.3) is nonlinear. As a result, to simulate experiments more accurately, a nonlinear softening function is often useful.

We choose an exponential decay function as follows:

$$f_s^{nl} = \exp\left(-\alpha \frac{u_n}{u_0}\right), \tag{3.90}$$

where α is a positive constant that determines the value of f_s^{nl} for $u_n = u_0$, and u_0 is a parameter used to obtain the appropriate fracture energy. The only modification to the specific equations for nonlinear softening is for $\partial f_s^{nl}/\partial u_n$ with

$$\frac{\partial f_s^{nl}}{\partial u_n} = -\frac{\alpha}{u_0} \exp\left(-\alpha \frac{u_n}{u_0}\right). \tag{3.91}$$

Substituting in eq. 3.91 into eq. 3.59, results in the specific form of Ψ for nonlinear softening,

$$\Psi^{nl} = \frac{\alpha h_c}{u_0} \exp\left(-\alpha \frac{u_n}{u_0}\right) - \frac{C_{11}}{\tau_{nf}}. \tag{3.92}$$

For nonlinear softening, the crack opening displacement and stress increments now depend on the crack opening u_n because Ψ^{nl} now depends on u_n. Substituting eq. 3.92 into eq. 3.69 results in

$$\Delta u_n = \frac{h_c \left(C_{11}\Delta e_{nn} + C_{12}\Delta e_{tt}\right)}{C_{11} - \dfrac{\alpha h_c \tau_{nf}}{u_0} \exp\left(-\alpha \dfrac{u_n}{u_0}\right)}. \tag{3.93}$$

For simplicity we use an explicit update for the crack opening displacement increment at the current increment $n+1$ as follows:

$$\Delta u_n^{n+1} = \frac{h_c \left(C_{11}\Delta e_{nn}^{n+1} + C_{12}\Delta e_{tt}^{n+1}\right)}{C_{11} - \dfrac{\alpha h_c \tau_{nf}}{u_0} \exp\left(-\alpha \dfrac{u_n^n}{u_0}\right)}, \tag{3.94}$$

where u_n^n is the crack opening displacement at the previous increment n. The crack opening displacement at the current increment u_n^{n+1} is then updated using eq. 3.70. The stress update follows that of eqs. 3.65 and 3.68. The resulting constitutive equations remain explicit and therefore no iterations are required.

Next, we apply the constraints imposed in eqs. 3.66 and 3.67 as follows:

$$\Psi_n^* = \frac{\Psi_n}{\Psi^{nl}} > 1 \rightarrow \frac{\alpha h_c}{u_0} \exp\left(-\alpha \frac{u_n}{u_0}\right) > 0 \tag{3.95}$$

$$\Psi^{nl} \neq 0 \rightarrow \frac{C_{11}}{\tau_{nf}} - \frac{\alpha h_c}{u_0} \exp\left(-\alpha \frac{u_n}{u_0}\right) > 0 \rightarrow h_c < \frac{C_{11} u_0}{\tau_{nf} \exp\left(-\alpha \frac{u_n}{u_0}\right)}. \tag{3.96}$$

The constraint imposed in eq. 3.95 is always satisfied because the exponential function is always positive and α, h_c, and u_0 are assumed positive constants. The smallest constraint on h_c imposed in eq. 3.96 is for $u_n = 0$ and it is the same constraint required for linear softening.

Following eq. 3.87, the fracture energy becomes

$$G_f = \int_0^{u_0} \tau_n du_n = \int_0^{u_0} \tau_{nf} f_s^{nl} du_n = \frac{u_0 \tau_{nf}}{\alpha} \left[1 - \exp(-\alpha)\right]. \tag{3.97}$$

As in the previous section, if G_f is known, then u_0 can be estimated by applying eq. 3.97 as follows:

$$u_0 = \frac{\alpha G_f}{\tau_{nf} \left[1 - \exp(-\alpha)\right]}. \tag{3.98}$$

3.3.4 Concluding Remarks

In the previous section, a set of constitutive equations were presented to compute the stress in an element undergoing failure. The symmetry in the stress tensor is contained in Ψ_n and Ψ_t, which allows Ψ to take a general form. The form of the softening function is contained in Ψ and as a result Ψ_n and Ψ_t will remain unchanged if a different softening function is used. For implementation of the failure model into an existing finite element code, it is recommended that the stress and crack opening displacement relations that contain Ψ_n^* and Ψ_t^* be used to simplify the implementation. As a result, only an update to Ψ is required if a different softening function is used. This also helps simplify the hourglass force implementation as discussed further in Section 4.3.2.

Chapter 4

Algorithm

This chapter provides the numerical algorithm that employs the following components: (i) standard finite element formulation, (ii) failure model proposed in Chapter 3, (iii) new hourglass control methods, (iv) crack tracking algorithm, and (v) the complete numerical algorithm.

First, the strong form of the governing equations is presented followed by the weak form. The resulting set of finite element equations are then provided. Next, new hourglass control methods are derived that exactly reproduce four-point quadrature when only one integration point is employed and do not require hourglass coefficients when applied to square, rectangular, or parallelogram quadrilateral elements. The crack tracking algorithm is presented next which provides the correct crack path. Finally, the complete numerical algorithm is detailed for explicit time integration.

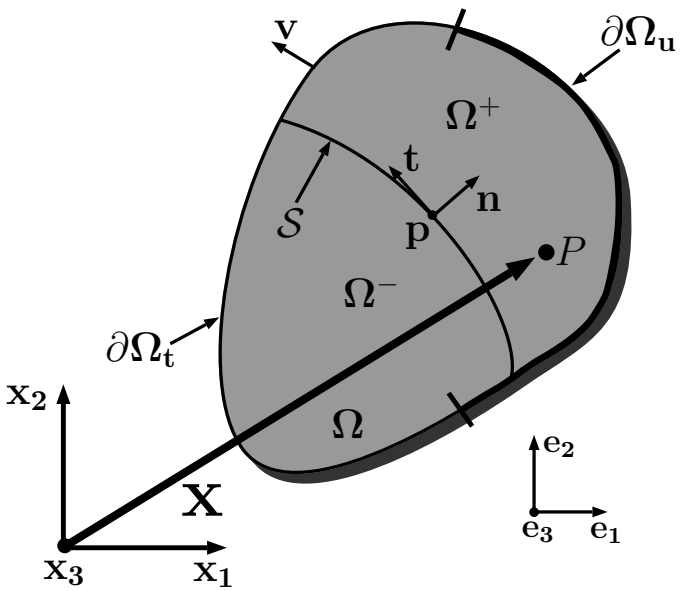

Figure 4.1: Solid Continuum Domain

4.1 Governing Equations

4.1.1 Kinematics

Consider a solid material domain $\Omega \in \mathbb{R}^3$ with positive density $\rho \in \mathbb{R}$ and boundary $\partial\Omega$ with displacement and traction boundary conditions applied to $\partial\Omega_u$ and $\partial\Omega_t$, respectively, such that $\partial\Omega = \partial\Omega_u \cup \partial\Omega_t$ as shown in Figure 4.1. The material domain is assumed to follow small deformation kinematics. As a result, the reference and deformed configurations are the same. The location of a point P in Ω is defined with the position vector $\mathbf{x} \in \Omega$, where $\mathbf{x}$ is defined using the Cartesian basis vectors $\mathbf{x} = x_1\mathbf{e_1} + x_2\mathbf{e_2} + x_3\mathbf{e_3}$. Let the possibility exist for a discontinuity to form due to a crack opening with displacement $[[\mathbf{u}]]$ such that a new surface $\mathcal{S}$ is formed creating two sub-domains Ω^- and Ω^+. The crack boundary $\mathcal{S}$ is defined by the normal vector $\mathbf{n}$ and tangential vectors $\mathbf{t}$ and $\mathbf{p}$, respectively, where $\mathbf{n} \cdot \mathbf{t} = 0$ and $\mathbf{n} \times \mathbf{t} = \mathbf{p}$. Following the strong discontinuity formulation presented in the works

of Oliver [46, 47] and Sanchez [45], the displacement field at $\mathbf{x}$ and at time t can be described in terms of regular (continuous) $\bar{\mathbf{u}}(\mathbf{x},t)$ and discontinuous $H_{\mathcal{S}}(\mathbf{x})[[\mathbf{u}]](\mathbf{x},t)$ components as follows:

$$\mathbf{u}(\mathbf{x},t) = \bar{\mathbf{u}}(\mathbf{x},t) + H_{\mathcal{S}}(\mathbf{x})[[\mathbf{u}]](\mathbf{x},t), \tag{4.1}$$

where $H_{\mathcal{S}}(\mathbf{x})$ is the Heaviside step function defined from

$$H_{\mathcal{S}}(\mathbf{x}) = \begin{cases} 1 & \forall \quad \mathbf{x} \in \Omega^{+} \\ 0 & \forall \quad \mathbf{x} \in \Omega^{-} \end{cases} \tag{4.2}$$

The strain is computed by taking the symmetric part of the gradient of the displacement field from eq. 4.1 as follows:

$$\mathbf{e}(\mathbf{x},t) = (\nabla \mathbf{u})^{\mathrm{S}} = (\nabla \bar{\mathbf{u}})^{\mathrm{S}} + H_{\mathcal{S}} \left(\nabla [[\mathbf{u}]]\right)^{\mathrm{S}} + \delta_{\mathcal{S}} \left([[\mathbf{u}]] \otimes \mathbf{n}\right)^{\mathrm{S}}, \tag{4.3}$$

where $\delta_{\mathcal{S}}$ is the Dirac delta function. The first two terms of eq. 4.3 represent the regular or continuous strain $\bar{\mathbf{e}}(\mathbf{x},t)$. Hence we can write the total strain as follows:

$$\mathbf{e}(\mathbf{x},t) = \bar{\mathbf{e}}(\mathbf{x},t) + \left(\nabla [[\mathbf{u}]]\right)^{\mathrm{S}} + \delta_{\mathcal{S}} \left([[\mathbf{u}]] \otimes \mathbf{n}\right)^{\mathrm{S}}. \tag{4.4}$$

Because $\delta_{\mathcal{S}}$ is singular it must be regularized. The regularization gives a function that can be evaluated pointwise. We follow the method proposed in [48] where the discontinuity is assumed with finite dimension L_c over the domain Ω^{L_c}. The characteristic length L_c is equal to the size of the crack band dimension or the characteristic element size h_c as discussed in Chapter 3. A regularized version of the Dirac delta function is expressed as,

$$\delta_{\mathcal{S}}^{L_c} = \begin{cases} \dfrac{1}{L_c} & \forall \quad \mathbf{x} \in \Omega^{L_c} \\ 0 & \forall \quad \mathbf{x} \in \Omega / \Omega^{L_c} \end{cases} \tag{4.5}$$

4.1.2 Constitutive Equations

The stress update in the material follows that of the failure model for mode-I cracks derived in Chapter 3. However, the model is generalized to three-dimensions here. The stress in the continuous material is computed from Hooke's law as follows,

$$\boldsymbol{\sigma} = \mathbb{E} : \mathbf{e}^e \quad \forall \quad \mathbf{x} \in \Omega/\mathcal{S}. \tag{4.6}$$

where the elastic strain $\mathbf{e}^e$ is computed from

$$\mathbf{e}^e(\mathbf{x}, t) = (\nabla \mathbf{u})^{\mathrm{S}} \quad \forall \quad \mathbf{x} \in \Omega/\mathcal{S}, \tag{4.7}$$

Recall that $\boldsymbol{\sigma}$ is the Cauchy stress. If failure has initiated or if the decohesion function $F > 0$, then the stress is updated based on a stress increment tensor $\Delta\boldsymbol{\sigma}^{\boldsymbol{cr}}$ as follows:

$$\boldsymbol{\sigma}^{\boldsymbol{cr}} = \boldsymbol{\sigma}_n^{\boldsymbol{cr}} + \Delta\boldsymbol{\sigma}^{\boldsymbol{cr}} \quad \forall \quad \mathbf{x} \in \mathcal{S}, \tag{4.8}$$

where $\boldsymbol{\sigma}_n^{\boldsymbol{cr}}$ is the stress from the previous increment. The decohesion function defined in Section 3.3 is the following:

$$F = \frac{\tau_n}{\tau_{nf}} - f_s = \frac{\sigma_{nn}}{\tau_{nf}} - f_s, \tag{4.9}$$

where f_s is defined either for linear or nonlinear softening using eqs. 3.73 or 3.90, respectively. The components of the stress increment tensor in the crack basis is built to accommodate mode-I failure in the crack basis as follows:

$$[\Delta\sigma^{cr}] = \begin{bmatrix} \Delta\sigma_{nn} & 0 & 0 \\ 0 & \Delta\sigma_{tt} & 0 \\ 0 & 0 & 0 \end{bmatrix}, \tag{4.10}$$

where the stress increment components $\Delta\sigma_{nn}$ and $\Delta\sigma_{tt}$ are defined using equation 3.65.

4.1.3 Initial Boundary Value Problem Statement

The governing equations that predict the response of a solid material domain Ω with boundary $\partial\Omega$ at time t as shown in Figure 4.1 are provided. Without the consideration of thermodynamic effects, the governing equations are the conservation of linear and angular momentum

$$\rho\ddot{\mathbf{u}} = \nabla \cdot \boldsymbol{\sigma} + \rho\mathbf{f} \qquad \forall \quad \mathbf{x} \in \Omega, \quad t \geq 0 \tag{4.11}$$

$$\boldsymbol{\sigma} = \boldsymbol{\sigma}^T \qquad \forall \quad \mathbf{x} \in \Omega, \quad t \geq 0, \tag{4.12}$$

where $\ddot{\mathbf{u}}(\mathbf{x}, t)$ is the acceleration of a material point P with density $\rho(\mathbf{x}, t)$ located at $\mathbf{x}$ and $\mathbf{f}(\mathbf{x}, t)$ is the body force per unit mass acting at point P for all $\mathbf{x} \in \Omega$ and $t \geq 0$.

Because the governing equation involves a partial differential equation (PDE) of order two with respect to time, the initial displacement $\mathbf{u}(\mathbf{x}, 0) = \mathbf{u}_0(\mathbf{x})$ and velocity $\dot{\mathbf{u}}(\mathbf{x}, 0) = \dot{\mathbf{u}}_0(\mathbf{x})$ must be specified for all points $\mathbf{x} \in \Omega$. These requirements represent the initial conditions. In addition, the requirements for all points on the boundary $\mathbf{x} \in \partial\Omega$ for all time $t \geq 0$ must be specified. These set of requirements are the boundary conditions. In this instance, the displacement boundary conditions are applied to all $\mathbf{x} \in \partial\Omega_u$ such that $\mathbf{u}(\mathbf{x}, t) = \mathbf{g}(\mathbf{x}, t)$. The traction boundary conditions are applied to all $\mathbf{x} \in \partial\Omega_t$ such that $\boldsymbol{\sigma}(\mathbf{x}, t) \cdot \mathbf{v} = \mathbf{h}(\mathbf{x}, t)$, where $\mathbf{v}$ is the unit normal vector of $\partial\Omega_t$. The initial and boundary conditions are summarized below:

$$\begin{aligned}
\mathbf{u}(\mathbf{x}, 0) &= \mathbf{u}_0(\mathbf{x}) && \forall \quad \mathbf{x} \in \Omega \\
\dot{\mathbf{u}}(\mathbf{x}, 0) &= \dot{\mathbf{u}}_0(\mathbf{x}) && \forall \quad \mathbf{x} \in \Omega \\
\mathbf{u}(\mathbf{x}, t) &= \mathbf{g}(\mathbf{x}, t) && \forall \quad \mathbf{x} \in \partial\Omega_u \\
\boldsymbol{\sigma}(\mathbf{x}, t) \cdot \mathbf{v} &= \mathbf{h}(\mathbf{x}, t) && \forall \quad \mathbf{x} \in \partial\Omega_t.
\end{aligned}$$

The strong form of the initial boundary value problem can now be stated. Given $\rho(\mathbf{x}, t)$, $\mathbf{f}(\mathbf{x}, t)$, $\dot{\mathbf{u}}_0(\mathbf{x})$, $\mathbf{u}_0(\mathbf{x})$, $\mathbf{g}(\mathbf{x}, t)$, and $\mathbf{h}(\mathbf{x}, t)$, find $\mathbf{u}(\mathbf{x}, t)$ such that the following

equations are satisfied:

$$\rho\ddot{\mathbf{u}} = \nabla \cdot \boldsymbol{\sigma} + \rho\mathbf{f} \qquad \forall \quad \mathbf{x} \in \Omega, \quad t \geq 0 \tag{4.13}$$

$$\mathbf{u}(\mathbf{x}, 0) = \mathbf{u}_0(\mathbf{x}) \qquad \forall \quad \mathbf{x} \in \Omega \tag{4.14}$$

$$\dot{\mathbf{u}}(\mathbf{x}, 0) = \dot{\mathbf{u}}_0(\mathbf{x}) \qquad \forall \quad \mathbf{x} \in \Omega \tag{4.15}$$

$$\mathbf{u}(\mathbf{x}, t) = \mathbf{g}(\mathbf{x}, t) \qquad \forall \quad \mathbf{x} \in \partial\Omega_u \tag{4.16}$$

$$\boldsymbol{\sigma}(\mathbf{x}, t) \cdot \mathbf{v} = \mathbf{h}(\mathbf{x}, t) \qquad \forall \quad \mathbf{x} \in \partial\Omega_t, \tag{4.17}$$

where the stress in the material is computed as follows:

$$\boldsymbol{\sigma} = \mathbb{E} : \mathbf{e}^e \qquad \forall \quad \mathbf{x} \in \Omega/\mathcal{S} \tag{4.18}$$

$$\boldsymbol{\sigma} = \boldsymbol{\sigma}^{cr} \qquad \forall \quad \mathbf{x} \in \mathcal{S} \tag{4.19}$$

$$\boldsymbol{\sigma} \cdot \mathbf{n} = \boldsymbol{\tau} = \boldsymbol{\sigma}^{cr} \cdot \mathbf{n} \qquad \forall \quad \mathbf{x} \in \mathcal{S} \tag{4.20}$$

$$\mathbf{e}^e = (\nabla \mathbf{u})^{\mathrm{S}} \qquad \forall \quad \mathbf{x} \in \Omega/\mathcal{S}. \tag{4.21}$$

The stress in the crack basis $\boldsymbol{\sigma}^{cr}$ is updated following eqs. 4.8 through 4.10.

4.2 Finite Element Formulation

The finite element formulation given is a standard formulation following that given by Hughes [4]. However, rather than forming a stiffness matrix, nodal forces are computed directly from the stress that is computed explicitly. This allows a general constitutive model to be applied.

4.2.1 Weak Form

The algorithms that are used to simulate the response of the material body Ω are based on a set of finite element equations that are valid for a subdomain of Ω denoted Ω_e or the domain of a single finite element. However, before these finite element

equations can be derived, the weak form of eq. 4.13 must be available. In simple terms, the weak form is obtained by forming a residual version of the strong form of eq. 4.13 and then integrating over the problem domain Ω the product of the residual with a weight function or variation of the solution $\mathbf{w}(\mathbf{x}, t)$ as follows:

$$\int_{\Omega} \mathbf{w} \cdot (\rho \ddot{\mathbf{u}} - \nabla \cdot \boldsymbol{\sigma} - \rho \mathbf{f})\, d\Omega \tag{4.22}$$

The evaluation of the second term of eq. 4.22 requires further attention. By applying the product rule of differentiation, the second term can be expressed as

$$-\int_{\Omega} \mathbf{w} \cdot \nabla \cdot \boldsymbol{\sigma} d\Omega = \int_{\Omega} \nabla \mathbf{w} : \boldsymbol{\sigma} d\Omega - \int_{\Omega} \nabla \cdot (\mathbf{w} \cdot \boldsymbol{\sigma})\, d\Omega. \tag{4.23}$$

The divergence theorem can be applied to the last term in eq. 4.23 resulting in

$$\int_{\Omega} \nabla \cdot (\mathbf{w} \cdot \boldsymbol{\sigma})\, d\Omega = \int_{\partial\Omega} \mathbf{w} \cdot \boldsymbol{\sigma} \cdot \mathbf{n} d\partial\Omega = \int_{\partial\Omega} \mathbf{w} \cdot \boldsymbol{\tau} d\partial\Omega. \tag{4.24}$$

But $\mathbf{w}$ is required to be zero on $\partial\Omega_u$ therefore

$$\int_{\partial\Omega} \mathbf{w} \cdot \boldsymbol{\tau} d\partial\Omega = \int_{\partial\Omega_t} \mathbf{w} \cdot \boldsymbol{\tau} d\partial\Omega_t. \tag{4.25}$$

Subsituting eqs. 4.23 through 4.25 into eq. 4.22, the weak form of eq. 4.13 becomes

$$\int_{\Omega} \mathbf{w} \cdot \rho \ddot{\mathbf{u}} d\Omega = -\int_{\Omega} \nabla \mathbf{w} : \boldsymbol{\sigma} d\Omega + \int_{\partial\Omega_t} \mathbf{w} \cdot \boldsymbol{\tau} d\partial\Omega_t + \int_{\Omega} \mathbf{w} \cdot \rho \mathbf{f} d\Omega. \tag{4.26}$$

For simplicity, let's assume that no body forces such as gravity act on Ω or $\mathbf{f} = \mathbf{0}$. The final weak form simplifies to

$$\int_{\Omega} \mathbf{w} \cdot \rho \ddot{\mathbf{u}} d\Omega = -\int_{\Omega} \nabla \mathbf{w} : \boldsymbol{\sigma} d\Omega + \int_{\partial\Omega_t} \mathbf{w} \cdot \boldsymbol{\tau} d\partial\Omega_t. \tag{4.27}$$

4.2.2 Discrete Finite Element Equations

The weak form ultimately involves a sum of integrals over Ω_e, the local element domain, that are evaluated using shape functions and their derivatives over an isoparametric element in the parent $\{\xi, \eta\}$ domain. These integrals ultimately become

sums over the quadrature points in the parent domain after Gauss quadrature is implemented. The global effect of all the element domain quantities are captured through an assembly process where the nodal force contributions from each element are summed and placed into a global nodal force vector. For simplicity, the finite element equations will be formulated in two dimensions with coordinates $\{x_1, x_2\}$ and basis vectors $\{\mathbf{e}_1, \mathbf{e}_2\}$. Also, here we assume that $\{x, y\} = \{x_1, x_2\}$.

The first step in the process of deriving the local element integrals from the weak form is to express Galerkin approximations to the weight function $\mathbf{w}$ and the solution $\mathbf{u}$ using element shape functions. Then the components of $\mathbf{w}$ and $\mathbf{u}$ are represented as follows:

$$w_i^h(\mathbf{x}, t) = \sum_{A=1}^{N_n} N_A(\mathbf{x}) w_{iA}(t) \tag{4.28}$$

$$u_i^h(\mathbf{x}, t) = \sum_{A=1}^{N_n} N_A(\mathbf{x}) u_{iA}(t), \tag{4.29}$$

where $N_A(\mathbf{x})$ are the shape functions, $w_{iA}(t)$ and $u_{iA}(t)$ are the values of $w_i^h(\mathbf{x}_A, t)$ and $u_i^h(\mathbf{x}_A, t)$ at the nodes, and the numbered subscripts on w_{iA} and u_{iA} represent the components in the $\mathbf{e}_i$ direction. The general procedure is to factor out the summations and the w_{iA} terms from the integrals that will allow the derivation of the internal force vector, external force vector, and the mass matrix. First, let's convert eq. 4.27 into indicial notation as follows[1]:

$$E_1 = E_2 + E_3, \tag{4.30}$$

where

$$E_1 = \int_\Omega \rho w_i \ddot{u}_i d\Omega \tag{4.31}$$

[1] $\mathbf{T} : \mathbf{S} = \mathbf{T}^{\mathrm{S}} : \mathbf{S}$, where $\mathbf{T}$ is a nonsymmetric tensor, $\mathbf{S}$ is a symmetric tensor, and $\mathbf{T}^{\mathrm{S}}$ is the symmetric part of $\mathbf{T}$. This relation is used in the term E_2.

$$E_2 = -\int_\Omega w_{i,j}\sigma_{i,j}d\Omega \tag{4.32}$$

$$E_3 = \int_{\partial\Omega} w_i\tau_i d\partial\Omega. \tag{4.33}$$

Now eqs. 4.28 and 4.29 are substituted into eq. 4.30 to obtain

$$E_1 = \delta_{ij}\int_\Omega \rho \sum_{A=1}^{Nn} N_A(\mathbf{x})w_{iA}(t)\sum_{B=1}^{Nn} N_B(\mathbf{x})\ddot{u}_{jB}(t)d\Omega \tag{4.34}$$

$$E_2 = -\int_\Omega \sum_{A=1}^{Nn} N_{A,j}(\mathbf{x})w_{iA}(t)\sigma_{ij}(\mathbf{x},t)d\Omega \tag{4.35}$$

$$E_3 = \int_{\partial\Omega} \sum_{A=1}^{Nn} N_A(\mathbf{x})w_{iA}(t)\tau_i(\mathbf{x},t)d\partial\Omega. \tag{4.36}$$

Simplifying eqs. 4.34 through 4.36 results in,

$$E_1 = \sum_{A=1}^{Nn} w_{iA}(t)\sum_{B=1}^{Nn}\delta_{ij}\left(\int_\Omega \rho N_A(\mathbf{x})N_B(\mathbf{x})d\Omega\right)\ddot{u}_{jB}(t) \tag{4.37}$$

$$E_2 = -\sum_{A=1}^{N_n} w_{iA}(t)\int_\Omega N_{A,j}(\mathbf{x})\sigma_{ij}(\mathbf{x},t)d\Omega \tag{4.38}$$

$$E_3 = \sum_{A=1}^{Nn} w_{iA}(t)\int_{\partial\Omega} N_A(\mathbf{x})\tau_i(\mathbf{x},t)d\partial\Omega. \tag{4.39}$$

By substituting E_1, E_2, and E_3 into eq. 4.30 and observing that the result is satisfied for all w_{iA} subject to the conditions that $w_{iA} = 0$ on $\partial\Omega_u$, the discrete finite element equations reduce to

$$[M]\{\ddot{u}\} = \{F\}^I + \{F\}^E, \tag{4.40}$$

where $[M]$ is the mass matrix, $\{F\}^I$ is the internal nodal force vector, and $\{F\}^E$ is the external nodal force vector. The mass matrix and nodal force vectors can be thought of as a sum of integral contributions over each element area A^e as follows:

$$[M] = \sum\int_{A^e}[m]dA^e \tag{4.41}$$

$$\{F\}^I = \sum\int_{A^e}\{f\}^I dA^e \tag{4.42}$$

$$\{F\}^E = \sum\int_{A^e}\{f\}^E dA^e, \tag{4.43}$$

where the components of the local element mass matrix $[m]$ and local element internal and external nodal force vectors $\{f\}^I$ and $\{f\}^E$ are

$$m_{pq} = \delta_{ij} \int_A \rho N_A(\mathbf{x}) N_B(\mathbf{x}) dA \tag{4.44}$$

$$f_p^I = -\int_A B_{ik}^A(\mathbf{x}) \sigma_k^v(\mathbf{x}, t) dA \tag{4.45}$$

$$f_p^E = \int_{\partial\Omega_t} N_A(\mathbf{x}) \tau_i(\mathbf{x}, t) dA. \tag{4.46}$$

Note that the indices p and q are used for convenience to populate computational arrays. They represent positions within the finite element arrays and this convention is used in [4]. The indices p and q are

$$p = N_{dof}(A-1) + i, \qquad \text{for } A = 1...N_{en}, i = 1...N_{dof} \tag{4.47}$$

$$q = N_{dof}(B-1) + j, \qquad \text{for } B = 1...N_{en}, j = 1...N_{dof}. \tag{4.48}$$

where N_{en} are the number of nodes per element and N_{dof} is the number of degrees of freedom per node. Note that for the 4-node quad $N_{en} = 4$ and with nodal displacements in the $\mathbf{e}_1$ and $\mathbf{e}_2$ directions $N_{dof} = 2$. The matrix $[B]^A$ is filled with shape function derivatives as follows:[2].

$$\left[B^A\right] = \begin{bmatrix} N_{A,x} & 0 & N_{A,y} \\ 0 & N_{A,y} & N_{A,x} \end{bmatrix}, A = 1..4 \tag{4.49}$$

The respective stress and strain vectors are

$$\{\sigma^v\} = \begin{Bmatrix} \sigma_{xx} \\ \sigma_{yy} \\ \sigma_{xy} \end{Bmatrix} \tag{4.50}$$

$$\{e^v\} = \begin{Bmatrix} e_{xx} \\ e_{yy} \\ 2e_{xy} \end{Bmatrix}, \tag{4.51}$$

[2] $[B]^A$ is actually the transpose of the matrix usually used in common textbooks.

where the strain components are computed using eqs. 2.21 through 2.23. Given the stress and strain vectors defined in eqs. B.9 and B.10, the elasticity matrix $[C]$, a matrix version of the fourth order elasticity tensor $\mathbb{E}$, can be defined. With assumptions of isotropy, the number of elastic constants reduces to two. For $\mathbf{x} \in \Omega/\mathcal{S}$, $[C]$ is defined below for plane stress and plane strain, respectively.

$$[C] = \frac{Y}{1-\nu^2}\begin{bmatrix} 1 & \nu & 0 \\ \nu & 1 & 0 \\ 0 & 0 & \frac{1-\nu^2}{2(1+\nu)} \end{bmatrix} \quad (\text{Plane} - \text{Stress}) \tag{4.52}$$

$$[C] = \frac{Y}{(1+\nu)(1-2\nu)}\begin{bmatrix} 1-\nu & \nu & 0 \\ \nu & 1-\nu & 0 \\ 0 & 0 & \frac{1}{2}-\nu \end{bmatrix} \quad (\text{Plane} - \text{Strain}) \tag{4.53}$$

where Y is Young's modulus and ν is Poisson's ratio. For $\mathbf{x} \in \Omega/\mathcal{S}$, the stress is computed as follows:

$$\{\sigma^v\} = [C]\{e^v\} \tag{4.54}$$

The discrete finite element equations are now in terms of the global coordinates $\mathbf{x}$ because the shape functions and their derivatives are evaluated at $\mathbf{x}$ and the limits of the integrals are also in the global coordinates. Figure 2.1 shows an arbitrary quadrilateral element in the global $\{x, y\}$ domain and $\{\xi, \eta\}$ parent domain. Isoparametric mapping will be applied next to transform the finite element equations to a more user friendly domain.

4.2.3 Isoparametric Mapping and Gauss Quadrature

The isoparametric element in the $\{\xi, \eta\}$ coordinate system with four quadrature points is shown in Figure 4.2(a) and with one integration point in Figure 4.2(b). The shape functions were provided in eqs. 2.1 through 2.4, the shape function derivatives in $\{\xi, \eta\}$ were provided in eqs. 2.5 through 2.12, and the shape function derivatives

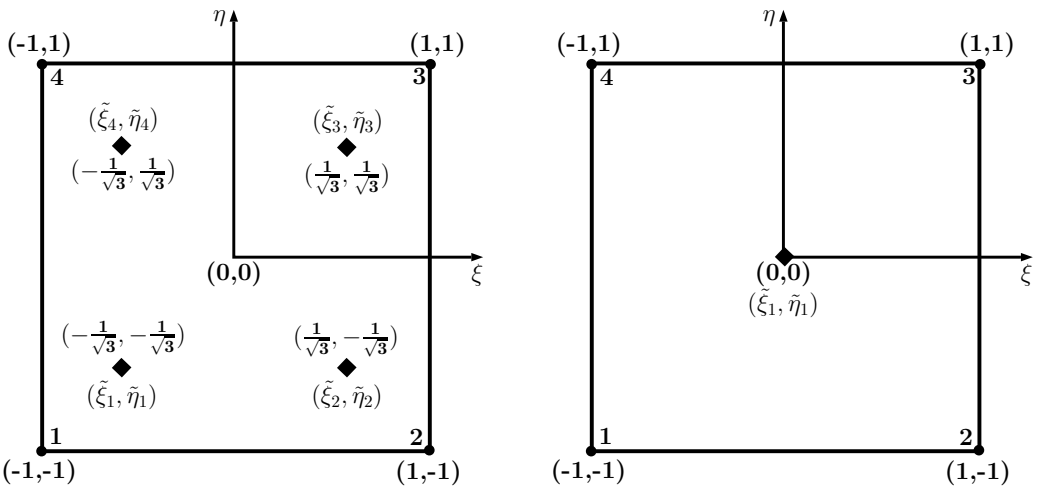

(a) Four Integration Points (b) One Integration Point

Figure 4.2: 4-node Quadrilateral Isoparametric Element

in $\{x, y\}$ that are required to evaluate $[B]^A$ are shown in eqs. 2.24 through 2.25. The important equations are repeated for convenience below.

$$N_{A,x} = \frac{N_{A,\xi} y_{,\eta} - N_{A,\eta} y_{,\xi}}{J}, \qquad \text{for } A = 1..N_{en}$$
$$N_{A,y} = \frac{-N_{A,\xi} x_{,\eta} + N_{A,\eta} x_{,\xi}}{J}, \qquad \text{for } A = 1..N_{en},$$

where J is the determinant of the Jacobian and is written as,

$$J = x_{,\xi} y_{,\eta} - y_{,\xi} x_{,\eta}.$$

The derivatives of the global coordinates with respect to the local coordinates can be computed by summing over the nodes the product of the shape function derivatives and the nodal coordinates as follows:

$$x_{,\xi} = \sum_{i=1}^{4} N_{i,\xi} x_i^e$$
$$y_{,\xi} = \sum_{i=1}^{4} N_{i,\xi} y_i^e$$

$$x_{,\eta} = \sum_{i=1}^{4} N_{i,\eta} x_i^e$$
$$y_{,\eta} = \sum_{i=1}^{4} N_{i,\eta} y_i^e,$$

where $\{x_i^e, y_i^e\}$ are the global nodal coordinates. The shape function derivatives in $\{\xi, \eta\}$ are shown below.

$$N_{1,\xi} = \frac{1}{4}(\eta - 1), N_{2,\xi} = \frac{1}{4}(1 - \eta), N_{3,\xi} = \frac{1}{4}(1 + \eta), N_{4,\xi} = \frac{1}{4}(-1 - \eta)$$

$$N_{1,\eta} = \frac{1}{4}(\xi - 1), N_{2,\eta} = \frac{1}{4}(-1 - \xi), N_{3,\eta} = \frac{1}{4}(1 + \xi), N_{4,\eta} = \frac{1}{4}(1 - \xi).$$

The local element mass matrix and internal nodal force vector in the $\{\xi, \eta\}$ domain can be evaluated using $J(\xi, \eta)$ as follows:

$$m_{pq} = \delta_{ij} t_e \rho \int_{-1}^{1} \int_{-1}^{1} N_A(\xi, \eta) N_B(\xi, \eta) J(\xi, \eta) d\xi d\eta \tag{4.55}$$
$$f_p^I = -t_e \int_{-1}^{1} \int_{-1}^{1} B_{ik}^A(\xi, \eta) \sigma_k^v(\xi, \eta, t) J(\xi, \eta) d\xi d\eta, \tag{4.56}$$

where t_e is the constant thickness out of plane and a constant density ρ is assumed for simplicity. Applying Gauss quadrature at the coordinates $\{\tilde{\xi}, \tilde{\eta}\}$ and using a Gauss weight W for the l^{th} quadrature point results in the approximation of the local element mass matrix and internal nodal force vector,

$$m_{pq} \approx \delta_{ij} t_e \rho \sum_{l=1}^{N_{int}} N_A(\tilde{\xi}, \tilde{\eta}) N_B(\tilde{\xi}, \tilde{\eta}) J(\tilde{\xi}, \tilde{\eta}) W_l \tag{4.57}$$
$$f_p^I \approx -t_e \sum_{l=1}^{N_{int}} B_{ik}^A(\tilde{\xi}, \tilde{\eta}) \sigma_k^v(\tilde{\xi}, \tilde{\eta}, t) J(\tilde{\xi}, \tilde{\eta}) W_l, \tag{4.58}$$

where $W = 4 \ \forall \, l$ for one integration point and $W = 1 \ \forall \, l$ for four integration points. The quadrature point coordinates are shown in Figure 4.2.

4.2.4 Time Integration

The finite element or Galerkin equations that are to be solved are from eq. 4.40 and repeated below.

$$[M]\{\ddot{u}\} = \{F\}^I + \{F\}^E$$

The global mass matrix $[M]$ and the global force vectors $\{F\}^I$ and $\{F\}^E$ are computed by assembling all of the local element contributions. A lumped mass matrix $[M]^D$ is used in the algorithm where $[M]^D$ is formed by adding the rows of $[M]$ and placing the values along the diagonal of an empty matrix $[M]^D$.

Let $\{u\}^k$, $\{v\}^k$, and $\{a\}^k$ be numerical approximations to $\{u(t^k)\}$, $\{\dot{u}(t^k)\}$, and $\{\ddot{u}(t^k)\}$, respectively. The time t^k at time increment k is defined with $t^k = k\Delta t$ for $k = 0, 1...N_s$, where Δt is the time step and N_s is the number of time increments. Let the inverses of the lumped masses be stored in a vector $\{m\}^d$, where each element of $\{m\}^d$ represents the inverse of the row sum of the consistent mass matrix $[M]$. The i^{th} component of the acceleration, velocity, and displacement are approximated for the k or $k+1$ time increment using the following explicit time integrator:

$$a_i^k = m_i^d \left[\left(F_i^I\right)^k + \left(F_i^E\right)^k \right] \tag{4.59}$$

$$v_i^{k+1} = v_i^k + \Delta t a_i^k \tag{4.60}$$

$$u_i^{k+1} = u_i^k + \Delta t v_i^{k+1}. \tag{4.61}$$

The prescribed displacement boundary conditions are imposed by simply overwriting u_i^{k+1} in the appropriate positions. The time integration scheme provided is conditionally stable. A necessary, but not sufficient condition for stability requires that the time step be no larger than the time t_h it takes a wave of speed c to travel a distance h_{ct}, where h_{ct} is a good estimate for the smallest element dimension in the discretization. The transit time is $t_h = h_{ct}/c$. The stability requirement goes as follows:

$$\Delta t \leq N_{CFL} t_h \leq N_{CFL} \frac{h_c}{c} \leq N_{CFL} \frac{h_c}{\sqrt{Y/\rho}}, \tag{4.62}$$

where Y is Young's modulus and $N_{CFL} \equiv 1$ and is known as the Courant-Friedrichs-Lewy number or CFL number. The stability condition imposed on Δt is referred to as the CFL condition. The actual wave speed in the material might be difficult to estimate. As a result, a safety factor N_{sf} is typically used to prevent instabilities as follows:

$$\Delta t \leq N_{sf} N_{CFL} \frac{h_c}{\sqrt{Y/\rho}}, \tag{4.63}$$

where $N_{sf} \leq 1$. An example could be $N_{sf} = 0.8$.

4.2.5 Viscous Damping

The discrete finite element equations in 4.40 predict dynamic wave propagation where waves will travel back and forth across Ω as they reflect off the boundary $\partial\Omega$. However, the experiments that we seek to simulate, are quasi-static. As a result, the wave mechanics part of the solution is not that important in this instance. Viscous nodal damping can easily be added to force the solution to a quasi-static state much more rapidly thereby reducing simulation run times. Without going through the derivation, a damping term in the finite element equations can be added as follows:

$$[M]\{\ddot{u}\} + [C]\{\dot{u}\} = \{F\}^I + \{F\}^E. \tag{4.64}$$

The viscous damping matrix $[C]$ is commonly expressed as a scalar product of the mass matrix $[M]$ or $[C] = c[M]$, where c is the viscous damping coefficient. Substituting $[C]$ into eq. 4.64 and solving for the acceleration results in

$$\{\ddot{u}\} = [M]^{-1}\left(\{F\}^I + \{F\}^E - [C]\{\dot{u}\}\right) \tag{4.65}$$

$$= [M]^{-1}\left(\{F\}^I + \{F\}^E - c[M]\{\dot{u}\}\right) \tag{4.66}$$

$$= [M]^{-1}\left(\{F\}^I + \{F\}^E\right) - c\{\dot{u}\}. \tag{4.67}$$

The resulting time integration scheme becomes

$$a_i^k = m_i^d \left[\left(F_i^I\right)^k + \left(F_i^E\right)^k \right] - cv_i^k \tag{4.68}$$

$$v_i^{k+1} = v_i^k + \Delta t a_i^k \tag{4.69}$$

$$u_i^{k+1} = u_i^k + \Delta t v_i^{k+1}, \tag{4.70}$$

where no sum on i is implied. Comparing the time integration schemes with and without damping shows that only one extra term is required during the computation of a_i^k as shown in eq. 4.68. The critical time step may be affected by damping [49], but this analysis is beyond the scope of this dissertation. For now we will let the safety factor N_{sf} take care of such possibilities.

4.3 Hourglass Control

In order to compute the local element internal nodal force vector, the stress at each quadrature point and every element must be computed for every time step in explicit dynamic solvers. For iterative methods that solve the static problem, the constitutive model must be evaluated for each iteration for every quadrature point and element. Initially, reduced integration was used to alleviate locking when the material becomes incompressible. Here we note the importance of reducing the number of constitutive model evaluations as much as possible. Reduced integration serves this purpose. For the 4-node quadrilateral element, reduced integration involves evaluating the internal force vector using one integration point located at the center of the element. In comparison, full integration requires four integration points or quadruple the number of constitutive evaluations. For 3D applications, the computational savings is even more dramatic. However, using reduced integration leads to the activation of zero energy modes which results in errors in the solution and distortions in the mesh that have an hourglass (HG) shape. Methods that correct these errors are called hourglass control methods (HGM). A common HGM used today in many commercial and

government finite element codes was developed by Flanagan and Belytschko (FB) in 1981 [50]. This method derives a set of hourglass forces that are added to the local element nodal force vectors to remove the hourglass mode. However, an hourglass control coefficient is required which quite often requires a trial and error approach to optimize. For many problem types such as elasticity, the results are not too sensitive to the errors introduced by the HGM. However, for modeling softening, the HGM must be more precisely defined.

A set of two new hourglass control methods are derived to alleviate the errors and ambiguity generated by existing methods for a hardening element and a softening element. Here we define a *hardening* element to be an element whose stress increases with an increase in total strain. In contrast, a *softening* element undergoes a reduction in stress with an increase in total strain.

4.3.1 Hardening Element

Derivation of Exact Hourglass Forces

The procedure for deriving the exact hourglass forces that reproduce full integration is straightforward although algebraically cumbersome. This is the most direct approach to understanding what information gets lost when going from full or four-point quadrature to reduced or one-point quadrature. A similar and quite thorough analysis that considers the stiffness matrix to be additively composed into a stiffness matrix obtained from one-point integration and a stabilization matrix is provided in Liu et. al. [51] for several element types. Full integration is required to get the optimal accuracy, but not needed to maintain the rate of convergence with mesh refinement in continuous problems. The idea is to add this missing information back to the nodal force vector when using reduced integration with simple equations. An algebraic manipulation package *Maple* [52] was used to perform the symbolic quadrature operations.

The procedure is first to evaluate the 8×8 stiffness matrix following Gauss quadrature symbolically using four integration points for a single element. Next, the procedure is repeated with only one integration point. Subtracting these two results generates a Gauss quadrature stiffness error matrix. The exact hourglass corrective forces are derived by multiplying the stiffness error matrix by the 8×1 local element displacement vector. The resulting exact hourglass forces are algebraically simple for square, rectangular, and parallelogram shaped elements. However, for an arbitrary 4-node quad, the resulting equations are algebraically too complicated to be practically used in a code. Because many meshes are structured and contain simple element geometries, this method is still applicable to many problems.

The local element stiffness matrix $[k]^e$ for a unit thickness single element is computed by the following integral over the element area in the $\{x, y\}$ coordinate system as follows:

$$k^e_{pq} = e_i^T \iint [B]^A [D] \{[B]^B\}^T dA e_j. \tag{4.71}$$

Similarly, the same integral over the parent domain $\{\xi, \eta\}$ is

$$k^e_{pq} = e_i^T \int_{-1}^{1} \int_{-1}^{1} [B]^A [D] \{[B]^B\}^T J d\xi d\eta e_j. \tag{4.72}$$

The corresponding Gauss quadrature formula that approximates the preceding integral can be written as follows:

$$k^e_{pq} \approx e_i^T \sum_{l=1}^{N_{int}} [B]^A [D] \{[B]^B\}^T J W_l e_j, \tag{4.73}$$

where $[B]^A/[B]^B$ are defined by eq. 4.49, $[D]$ is a generalized material stiffness matrix that can be used either for a hardening element or a softening element, J with eq. 2.26 and $W = 4 \ \forall \ l$ for one integration point and $W = 1 \ \forall \ l$ for four integration points. Note also that $p = N_{dof}(A-1) + i$ for $A = 1..4$ and $q = N_{dof}(B-1) + j$ for $B = 1..4$ where N_{dof} is the number of degrees of freedom per node which equals two in this instance. Also, $[B]^A$ and $[B]^B$ are evaluated for the A^{th} and B^{th} shape

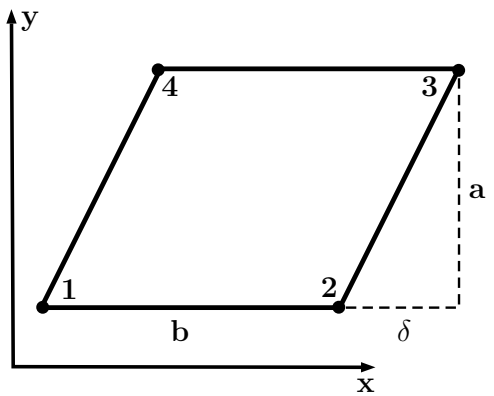

Figure 4.3: Hourglass Control Element Geometry

function at the l^{th} quadrature point in the parent domain, respectively. Finally, e_i^T and e_i are the i^{th} component of the basis vectors $\mathbf{e}_1$ and $\mathbf{e}_2$, where $i = 1..2$ and $j = 1..2$. The reason why the basis vectors show up here is that for each A and B a 2×2 submatrix is formed. The e_j term chooses the proper column of the submatrix and the e_i^T term chooses the proper row of this column to define the correct k_{pq}^e term. For example, the k_{11}^e, k_{12}^e, k_{21}^e, and k_{22}^e terms of the stiffness matrix would use $A = 1$, $B = 1$, $i = 1..2$, and $j = 1..2$. Another way to look at it is that the A and the B indices choose which submatrix to compute, while the i and the j indices choose which elements of the submatrix to extract. Of course, these terms must be summed over the quadrature points. Now, we form the quadrature error matrix that will provide exactly what the differences are between full and reduced integration as follows:

$$[E]^e = [k]_4^e - [k]_1^e, \tag{4.74}$$

where $[k]_4^e$ is the stiffness matrix computed symbolically using four integration points and $[k]_1^e$ is the stiffness matrix computed symbolically using one integration point. The exact hourglass force vector for a single element becomes,

$$\{f\}^{hg} = [E]^e\{u\}, \tag{4.75}$$

where $\langle u \rangle = \langle u_1, v_1, u_2, v_2, u_3, v_3, u_4, v_4 \rangle$.

Consider the element shown in Figure 4.3 of height a, width b, offset δ and thickness t_e. The corresponding hourglass forces that exactly reproduce full integration for an arbitrary material stiffness matrix $[D]$ are as follows:

$$\{f^{hg}\} = t_e \begin{Bmatrix} f_1^{hg} \\ f_2^{hg} \\ -f_1^{hg} \\ -f_2^{hg} \\ f_1^{hg} \\ f_2^{hg} \\ -f_1^{hg} \\ -f_2^{hg} \end{Bmatrix}, \tag{4.76}$$

where f_1^{hg} and f_2^{hg} are defined as

$$f_1^{hg} = \frac{1}{12}\left[\frac{a}{b}D_{11} + \left(\frac{b}{a} + \frac{\delta^2}{ba}\right)D_{33}\right]\bar{u} - \frac{1}{12}\frac{\delta}{b}\left(D_{33} + D_{12}\right)\bar{v} \tag{4.77}$$

$$f_2^{hg} = -\frac{1}{12}\frac{\delta}{b}\left(D_{33} + D_{12}\right)\bar{u} + \frac{1}{12}\left[\frac{a}{b}D_{33} + \left(\frac{b}{a} + \frac{\delta^2}{ba}\right)D_{22}\right]\bar{v}. \tag{4.78}$$

In addition the terms $\bar{u}$ and $\bar{v}$ are functions of the nodal displacements in the x and y directions written respectively as

$$\bar{u} = u_1 - u_2 + u_3 - u_4 \tag{4.79}$$

$$\bar{v} = v_1 - v_2 + v_3 - v_4. \tag{4.80}$$

The material stiffness matrix $[D]$ is assumed to have the following form:

$$[D] = \begin{bmatrix} D_{11} & D_{12} & 0 \\ D_{12} & D_{22} & 0 \\ 0 & 0 & D_{33} \end{bmatrix}. \tag{4.81}$$

To obtain $\{f^{hg}\}$ for a rectangle set $\delta = 0$ and for a square set $\delta = 0$ and $a = b$. If the material stiffness $[D]$ is equal to the material stiffness for plane stress or eq. 4.52,

then the resulting hourglass force components become

$$f_1^{hg} = \frac{Yt_e}{24\left(\nu^2-1\right)}\left[K_1\left(u_1-u_2+u_3-u_4\right)-K_3\left(v_1-v_2+v_3-v_4\right)\right] \tag{4.82}$$

$$f_2^{hg} = \frac{Yt_e}{24\left(\nu^2-1\right)}\left[-K_3\left(u_1-u_2+u_3-u_4\right)+K_2\left(v_1-v_2+v_3-v_4\right)\right], \tag{4.83}$$

with K_1 and K_2 defined as

$$K_1 = \frac{b}{a}\left(\nu-1\right)-2\frac{a}{b}+\frac{\delta^2}{ab}\left(\nu-1\right) \tag{4.84}$$

$$K_2 = \frac{a}{b}\left(\nu-1\right)-2\frac{b}{a}-\frac{2\delta^2}{ab} \tag{4.85}$$

$$K_3 = \frac{\delta}{b}\left(\nu+1\right). \tag{4.86}$$

Comparisons to the FB Hourglass Approach

Next, we focus on comparing the algebraic equations that result from the FB method to the hourglass forces that were just derived. Normally, the hourglass coefficient used in the FB method isn't known a priori. This section provides a way compute the optimum hourglass coefficient for the FB method. If the hourglass forces from the FB method [50] are derived symbolically for the parallelogram element in Figure 4.3, the resulting FB hourglass force vector $\{f_{FB}^{hg}\}$ becomes

$$\{f_{FB}^{hg}\} = \frac{\left(\nu-1\right)Yt_e}{128\left(1+\nu\right)\left(2\nu-1\right)}\begin{Bmatrix} \kappa_{fb}\frac{a}{b}\left(u_1-u_2+u_3-u_4\right) \\ \kappa_{fb}\frac{b^2+\delta^2}{ab}\left(v_1-v_2+v_3-v_4\right) \\ -\kappa_{fb}\frac{a}{b}\left(u_1-u_2+u_3-u_4\right) \\ -\kappa_{fb}\frac{b^2+\delta^2}{ab}\left(v_1-v_2+v_3-v_4\right) \\ \kappa_{fb}\frac{a}{b}\left(u_1-u_2+u_3-u_4\right) \\ \kappa_{fb}\frac{b^2+\delta^2}{ab}\left(v_1-v_2+v_3-v_4\right) \\ -\kappa_{fb}\frac{a}{b}\left(u_1-u_2+u_3-u_4\right) \\ -\kappa_{fb}\frac{b^2+\delta^2}{ab}\left(v_1-v_2+v_3-v_4\right) \end{Bmatrix}, \tag{4.87}$$

where κ_{fb} is the hourglass coefficient used in the FB method. Now comparing the exact hourglass force vector shown in eqs. 4.76 through 4.78 with the FB hourglass forces shown in eq. 4.87, we can make a few interesting observations. First, the FB approach will always contain error for nonsquare elements no matter what hourglass coefficent is used. This is because it uses one hourglass coefficient per spatial dimension κ_{fb}. If $\delta = 0$ is substituted into the exact hourglass forces in eq. 4.84 through 4.86, then $K_3 = 0$ and we essentially obtain two separate coefficients that operate on f_1^{hg} and f_2^{hg}. As a result, in order for the FB method to reproduce full integration it would need two hourglass coefficients κ_1 and κ_2, but it only uses one. Further, for the parallelogram element, notice how the exact hourglass force components have coupled displacements u_i and v_i which arises for $\delta \neq 0$. However, for the FB hourglass force components u_i and v_i are never coupled.

We compare the two methods for a simple reason. That is because it is possible to make a trivial modification to the FB approach such that it becomes exact for the square and rectangular element. This modification is to add a κ_i to FB where $i = 1..N_{sd}$, where N_{sd} is the number of spatial dimensions. By enforcing the condition where $\{f^{hg}\} = \{f_{FB}^{hg}\}$, it is possible to derive the optimum hourglass coefficients κ_1 and κ_2 such that FB becomes exact. The optimum hourglass coefficients are shown below for a square and rectangular element. Note that in order for the FB method to be exact for a parallelogram element, both κ_1 and κ_2 would need to depend on the nodal displacements. As a result, each element would need to have its own hourglass coefficients. We introduce this modification because the FB method is so widely used in the finite element community and improving it is rather simple. The key point however is that FB still works for an arbitrary element geometry, whereas, the exact hourglass forces are only exact for specific element geometries.

We also note that another type of coefficient could be introduced into the proposed hourglass control method denoted an *antilocking* coefficient. It is known that full integration may introduce locking into an element. Because the proposed approach

is equivalent to full integration, it may be susceptible to locking for incompressible materials. By introducing another coefficient, the antilocking effects of reduced integration could be obtained.

$$\kappa_1 = \kappa_2 = \frac{16\,(\nu-3)\,(2\nu-1)}{3\,(\nu-1)^2} \qquad \text{(square)} \tag{4.88}$$

$$\kappa_1 = \frac{16\,(2\nu-1)}{3\,(\nu-1)^2}\left[\frac{b^2}{a^2}\,(\nu-1)-2\right] \tag{4.89}$$

$$\kappa_2 = \frac{16\,(2\nu-1)}{3\,(\nu-1)^2}\left[\frac{a^2}{b^2}\,(\nu-1)-2\right] \quad \text{(rectangle)} \tag{4.90}$$

4.3.2 Softening Element

For an element undergoing softening, a similar hourglass force derivation procedure that was used for the hardening element is applied. However, the material stiffness $[D]$ must be defined for an element undergoing softening. Recall that in Section 3.3, the tangent crack stiffness (eq. 3.65) in the $\{\mathbf{n},\mathbf{t}\}$ basis was derived as follows:

$$[C^{cr}] = \begin{bmatrix} C_{11}\,(1-\Psi_n^*) & (C_{12}-C_{11}\Psi_t^*) & 0 \\ C_{12}\,(1-\Psi_n^*) & (C_{22}-C_{12}\Psi_t^*) & 0 \\ 0 & 0 & 0 \end{bmatrix}, \tag{4.91}$$

where $\Psi_n^* = \Psi_n/\Psi$ and $\Psi_t^* = \Psi_t/\Psi$. Recall that $[C^{cr}]$ is symmetric. The terms Ψ_n, Ψ_t, and Ψ are parameters that relate the normal crack strain rate $\dot{e}_{nn}^{cr}$ to the total normal strain rates $\dot{e}_{nn}$ and $\dot{e}_{tt}$ that were derived using the consistency condition of the decohesion function $\dot{F}=0$ as follows:

$$\dot{e}_{nn}^{cr} = \Psi_n^*\dot{e}_{nn} + \Psi_t^*\dot{e}_{tt}. \tag{4.92}$$

The definition of Ψ_n^* and Ψ_t^* for linear and nonlinear softening were provided in eqs. 3.82 through 3.84 and 3.92, respectively. Recall that Ψ is dependent on the specific softening function chosen while Ψ_n and Ψ_t are valid for any softening function. The parameters C_{11}, C_{22}, and C_{12} are the elements of the elasticity matrix defined in eqs.

4.52 and 4.53. The form of the stiffness in eq. 4.91 arises because the crack stiffness is only dependent on $\dot{e}_{nn}$ and $\dot{e}_{tt}$ and not on $\dot{e}_{nt}$. Also recall that the crack stiffness was designed to produce a reduction in stress with an increase in total strain.

The nodal forces are computed in the global coordinate system. However, the crack stiffness matrix is defined in the local crack coordinate system. As a result, the nodal displacements are mapped to the $\{\mathbf{n}, \mathbf{t}\}$ basis where the hourglass forces are computed. The hourglass forces computed in the crack basis are then mapped to the global basis and subsequently used to compute the total local element internal nodal force vector. First, the nodal displacements are mapped to the crack coordinate system as follows:

$$u_i^n = n_1 u_i + n_2 v_i \tag{4.93}$$

$$v_i^t = -n_2 u_i + n_1 v_i, \tag{4.94}$$

where n_1 and n_2 define the orientation of the $\{\mathbf{n}, \mathbf{t}\}$ axes (i. e. the failure orientation in this instance), u_i and v_i are the nodal displacements in the x and y directions for the local element node number i, where $i = 1..4$, and u_i^n and v_i^t are the nodal displacements in the $\mathbf{n}$ and $\mathbf{t}$ directions. The hourglass forces for a softening element in the crack basis are computed using eqs. 4.77 and 4.78 with $[D] = [C^{cr}]$ and using the nodal displacements u_i^n and v_i^t resulting in

$$f_n^{hgs} = \frac{1}{12b}\left(aC_{11}^{cr}\bar{u}^n - \delta C_{12}^{cr}\bar{v}^t\right) \tag{4.95}$$

$$f_t^{hgs} = \frac{1}{12b}\left[-\delta C_{12}^{cr}\bar{u}^n + \frac{1}{a}\left(b^2 + \delta^2\right)C_{22}^{cr}\bar{v}^t\right], \tag{4.96}$$

where

$$\bar{u}^n = u_1^n - u_2^n + u_3^n - u_4^n \tag{4.97}$$

$$\bar{v}^t = v_1^t - v_2^t + v_3^t - v_4^t. \tag{4.98}$$

The hourglass forces are then mapped to the global coordinate system as follows:

$$f_1^{hgs} = n_1 f_n^{hgs} - n_2 f_t^{hgs} \tag{4.99}$$

$$f_2^{hgs} = n_2 f_n^{hgs} + n_1 f_t^{hgs}. \tag{4.100}$$

The local element hourglass force vector then follows similarly from eq. 4.76. Based on the results of using the proposed hourglass control method for the softening element in crack propagation problems, we note that it is only necessary to include the non-softening portion of the hourglass forces provided in eqs. 4.95 and 4.96. The non-softening portion of the hourglass forces can be determined by setting $\partial f_s / \partial u_n = 0$ in the failure model. This results in $\Psi_n^* = 1$ and $\Psi_t^* = C_{12}/C_{11}$. As a result, $C_{11}^{cr} = C_{12}^{cr} = 0$ and $C_{22}^{cr} = C_{22} - C_{12}^2/C_{11}$. The hourglass force method used for cracked elements then reduces to

$$f_n^{hgs} = 0 \tag{4.101}$$

$$f_t^{hgs} = \frac{1}{12b}\left[\frac{1}{a}\left(b^2 + \delta^2\right)\left(C_{22} - \frac{C_{12}^2}{C_{11}}\right)\bar{v}^t\right]. \tag{4.102}$$

We again note that based on simulation results, we use only the vertical component of the hourglass forces and from eq. 4.100, the hourglass forces in the global coordinate system reduce to

$$f_1^{hgs} = 0 \tag{4.103}$$

$$f_2^{hgs} = n_1 f_t^{hgs}. \tag{4.104}$$

The reason why only the vertical portion of f_t^{hgs} must be used is not yet understood. Note that for plane stress, $C_{22} - C_{12}^2/C_{11} = Y$, where Y is Young's modulus. Also, for a two-dimensional state of stress, the orientation of the principal axes β (i.e. the failure angle in this instance), the principal basis vectors, and principal stresses can

be computed analytically as follows:

$$\beta = \frac{1}{2}\tan^{-1}\left(\frac{2\sigma_{xy}}{\sigma_{xx}-\sigma_{yy}}\right) \tag{4.105}$$

$$n_1 = \cos(\beta) \tag{4.106}$$

$$n_2 = \sin(\beta) \tag{4.107}$$

$$t_1 = \cos\left(\beta + \frac{\pi}{2}\right) \tag{4.108}$$

$$t_2 = \sin\left(\beta + \frac{\pi}{2}\right) \tag{4.109}$$

$$\sigma_{nn} = \frac{1}{2}\left(\sigma_{xx}+\sigma_{yy}\right) + \sqrt{\frac{1}{4}\left(\sigma_{xx}-\sigma_{yy}\right)^2 + \sigma_{xy}^2} \tag{4.110}$$

$$\sigma_{tt} = \frac{1}{2}\left(\sigma_{xx}+\sigma_{yy}\right) - \sqrt{\frac{1}{4}\left(\sigma_{xx}-\sigma_{yy}\right)^2 + \sigma_{xy}^2} \tag{4.111}$$

Again if hourglass forces for the square or rectangular element are desired, appropriate assumptions for a, b, and δ are applied. In practice, for either the hardening or softening element, for elements that are not square, rectangular, or a parallelogram a simple approach is followed to estimate the proper a, b, and δ where average values are computed using the local element coordinates as follows:

$$a \approx \frac{1}{2}\left(|y_3 - y_2| + |y_4 - y_1|\right) \tag{4.112}$$

$$b \approx \frac{1}{2}\left(|x_2 - x_1| + |x_3 - x_4|\right) \tag{4.113}$$

$$\delta \approx \frac{1}{2}\left(|x_3 - x_2| + |x_4 - x_1|\right). \tag{4.114}$$

4.4 Crack Tracking Algorithm

Even though the failure model was formulated to preclude spurious shear stress accumulating in the cracked element, the algorithm must also contain another ingredient such that the crack path remains mesh objective. A separate approach that provides the correct crack path is necessary because the predicted crack path tends to naturally follow the element edges. This leads to an inability in predicting curved crack

trajectories in which the crack must traverse the mesh at an angle. Even when there is no spurious shear stress in the solution, the crack path can still be incorrect. This happens because the stress field around the crack tip is misaligned with respect to the crack orientation determined from the failure model. This phenomenon is shown in Figure 4.4. The stress field should be oriented such that the peak stresses around the crack are straight up and down. However, the stresses are slightly rotated which ultimately causes the crack to propagate along the element edges.

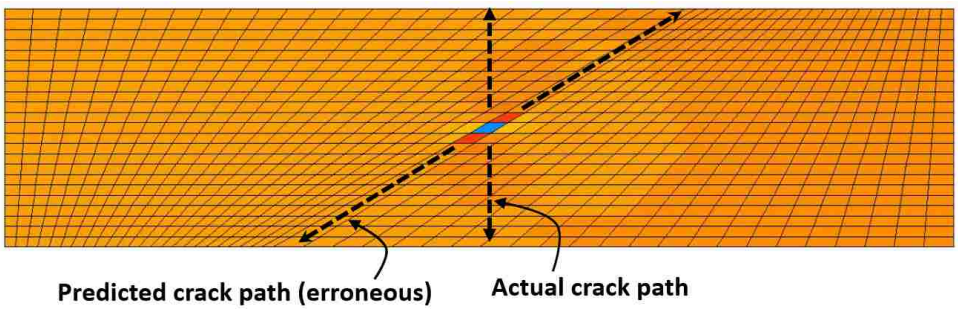

Figure 4.4: Stress Field Misalignment Around Crack Tip

The finite element approaches that have been successfully used to provide the correct crack path are of two primary categories: (1) nonlocal damage, stress, or strain measure and (2) a crack tracking algorithm. Some examples of the first for modeling concrete include the work of Bazant and Lin [12], Jirasek and Zimmermann [23], and Geers et. al. [53]. Although using a nonlocal measure can preclude some mesh dependence on the crack path, it requires additional computational expense. This is because the nonlocal measure is typically computed by taking an average of some variable, usually strain, over a neighborhood of points centered around the integration point. In addition, the mesh objectivity with respect to orientation of the elements of such methods is not well characterized especially for quadrilateral elements.

A more direct approach is to explicitly determine the crack path and allow failure to occur exclusively on this predicted path. This approach is applied in crack

tracking algorithms. Crack tracking algorithms do not necessarily preclude stress misalignment in a direct sense. Rather, the elements that would normally initiate failure during stress misalignment are not allowed to fail. Only elements that lie on the predicted crack path are allowed to fail and this restriction essentially realigns the stress field around the crack. However, crack tracking algorithms are susceptible to error because they can only be as good as the predicted crack orientation. For failure models that assume that the crack orientation is related to the principal stress basis, spurious shear can alter the predicted crack orientation and therefore lead to incorrect crack paths. Examples of local crack tracking algorithms can be found in Cervera and Chiumenti [54] and Cervera et. al. [55]. An example of a tracking algorithm that uses a nonlocal strain measure to define the crack direction can be found in Grassl and Jirásek [56].

The crack tracking algorithm that is proposed next was developed independently of the references cited previously. However, the algorithm is most similar to that proposed by Cervera et. al. [55]. In [55], a local stress measure is used to compute the crack orientation and subsequently a set of crack segments is determined for triangular elements. A set of algorithm flags is established that allows elements to initiate failure that intersect the computed crack segments. However [55] uses an isotropic continuum damage model and it isn't clear how spurious shear stress is handled in cracked elements. Further, mesh orientation objectivity with respect to the crack path isn't really demonstrated.

The following crack tracking algorithm proposed isn't necessarily the only way that it can be implemented within a code. There might be a more efficient computational way to construct the arrays and we leave it up to the reader to find other such possibilities. We begin by introducing a patch of nine quadrilateral finite elements where a crack initiates first in the element B as shown in Figure 4.5. This crack starts an individual crack branch. The patch contains eight adjacent elements defined by the Southwest element (SW), South (S), and so on. Because the location of the crack

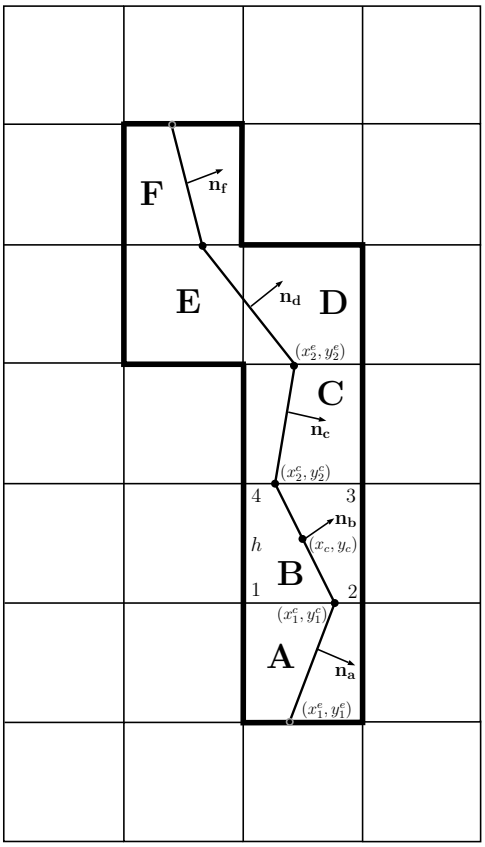

Figure 4.5: Tracking a Crack Through a Mesh

is immaterial for obtaining the smeared crack strain, we choose the crack segment to go through the center of initiated element (element B in this instance). The coordinates of element B of the first initiated element are defined with (x_c, y_c) and the orientation of the initiated crack is defined with the crack normal vector $\mathbf{n_b}$. The intersection of the line segment representing the initiated crack with the element edges are denoted the cracked element edge coordinates (CEECS). The CEECS of the first initiated crack are defined with (x_1^c, y_1^c) and (x_2^c, y_2^c). The local node numbering convention for all elements is shown for the center element in Figure 4.5. The starting crack coordinates (SCCS) are the coordinates of the crack root that start each crack segment after the first initiated crack and they are either (x_1^e, y_1^e) or (x_2^e, y_2^e). This

convention helps generalize the CEECS equations into three categories as shown in Appendix A. For subsequent cracked elements traveling away from the first initiated crack, a similar approach is applied to define the crack normals and CEECS. For example, for a crack traveling northward, the CEECS that must be updated are denoted as (x_2^e, y_2^e), where e denotes corresponding CEECS of the adjacent element. For cracks traveling southward, the CEECS that must be updated are (x_1^e, y_1^e).

For simplicity and consistency with a single crack forming in an element, one point integration is assumed. Here the mesh is assumed regular defined by horizontal (x) and vertical (y) lines. With reference to Figure 4.5, the following algorithm is followed:

1. We identify element B as having a crack. Elements C (above) and A (below) are identified as specific elements to be tested for crack initiation to indicate when the crack propagates.

2. Suppose element C next indicates a crack initiation with normal $\mathbf{n}_c$ which, in general, is not the same as $\mathbf{n}_b$. We adjust the location of this crack segment so that it is continuous with the crack segment in element B. Now element D (above C) is identified as an element to be followed for crack initiation.

3. Suppose element A is the next one to show crack initiation. A process similar to Step 2 is followed and the element below element A is identified as one to be checked for crack initiation with continued load steps.

4. Now if element D is the next element to initiate a crack segment with normal $\mathbf{n}_d$, the crack segment is made continuous with that in element C. However, now the crack segment passes through portions of two elements: element D and element E. Elements D and E are called cross-over elements and are forced to have identical characteristic crack lengths h_c, where $h_c = h_d + h_e$. The element dimensions for elements D and E are h_d and h_e, respectively. If no

change is made to the characteristic crack length for cross-over elements, the dissipated fracture energy is too large or the rate of unloading is to small. The adjustment to h_c causes the cross-over elements to unload at about the same rate as a single element that is adjacent to the cross-over (e.g. element C).

5. Element F is now designated as the element to be followed for crack continuation.

Let's now introduce a computational array of integers E_{adj} of dimension $N_{ele} \times 8$ that contains the adjacent element numbers associated with each element in the mesh, where N_{ele} is the number of elements. For example, the eight adjacent element numbers associated with element number 10, would be stored in the 10^{th} row of E_{adj} with adjacent element numbers stored along the columns as follows: SW, S, SE, E, NE, N, NW, W, and SW. This array is used to conveniently determine which elements are next in line to fail based on the CEECS of the current crack as discussed later. This array is formed during preprocessing.

Next, we introduce another computational array of integers C_{cond} of dimension $N_{ele} \times 3$. This array is used to apply flags that control which elements are allowed to fail and which require cross-over scaling. The first column of C_{cond} stores a value of 1 in the e_n row for elements that have initiated a crack branch where e_n is the element number. Taking the sum of all elements in the first column of C_{cond} equals the total number of independent crack branches or separate initiated cracks. However, to save computational expense, an accumulated sum of the total initiated number of cracks N_{cr} is determined and stored. Once the total number of allowed crack branches N_{crall} are formed, then the algorithm no longer allows new cracks to initiate. The second column of C_{cond} is used to store the crack condition number. The crack condition number is either 0, 1, or 2. A crack condition number of 0 (default) indicates the element has not yet cracked and isn't slated for cracking in the next strain increment. A crack condition number of 1 indicates that the crack tracking

algorithm has identified potential adjacent elements that intersect an evolving crack and these elements are now allowed to fail if the failure model deems it is appropriate. If the crack condition number is 2, then the crack is active and evolving. The third column of C_{cond} is used to store the cross-over flag I_{cross}. If $I_{cross} = 0$ (default), then the current crack is not part of a cross-over. However, if $I_{cross} = 1$, then the cracked element is within a cross-over and h_c is adjusted such that it equals the sum of the characteristic element dimensions that are within the cross-over.

Finally, an array of doubles C_{dbl} of dimension $N_{ele} \times 8$ is formed and the following components are stored in columns 1 through 8, respectively, as follows: N_1, N_2, T_1, T_2, x_1^e, y_1^e, x_2^e, and y_2^e, where N_1 is the $\mathbf{e}_1$ component of the crack normal vector $\mathbf{n}$, N_2 is the $\mathbf{e}_2$ component of the crack normal vector $\mathbf{n}$, T_1 is the $\mathbf{e}_1$ component of the crack tangential vector $\mathbf{t}$, T_2 is the $\mathbf{e}_2$ component of the crack tangential vector $\mathbf{t}$, and the CEECS are stored in (x_1^e, y_1^e) and (x_2^e, y_2^e).

Once failure initiation is detected, which is easily known once the decohesion function $F > 0$, the crack tracking algorithm must decide what failure scenario to engage from the following options: (1) the crack is newly initiated, (2) the crack is in an adjacent element, or (3) the crack is evolving. The framework of these choices is placed inside the failure model subroutine in the form of if-elseif statements. The first option or a newly initiated crack always occurs first because it is assumed that a propagating crack requires a single point of failure to start things off.

To identify scenario (1), the state of the crack condition array C_{cond} and the number of initiated cracks N_{cr} is examined. If $\mathrm{C}_{cond}(e_n, 1) = 0$ and $N_{cr} < N_{crall}$, then the crack is newly initiated and the following actions are completed: (1a) increment the current number of initiated cracks N_{cr}, (1b) set $\mathrm{C}_{cond}(e_n, 1) = 1$, (1c) set the CEECS compute flag $C_{ceecs} = 1$, (1d) set $\mathrm{C}_{cond}(e_n, 2) = 2$, (1e) compute the CEECS, (1f) extract the adjacent elements that intersect current crack, (1g) set $\mathrm{C}_{cond}(N_{adj}, 2) = 1$ where N_{adj} are the element numbers of the adjacent elements that are intersected by the initiated crack and are slated next for cracking, and (1h) update crack informa-

tion array C_{dbl}. In step (1c), the CEECS compute flag C_{ceecs} is an integer between 1 and 3 that is used to identify which set of CEECS equations are to be used. The CEECS equations are derived and stated in Appendix A.

Failure scenario (2) is identified by checking the value of C_{cond}. If $\mathrm{C}_{cond}(e_n, 2) = 1$, then the adjacent element that was flagged in scenario (1) has now cracked. As a result, the following actions are performed: (2a) set $\mathrm{C}_{cond}(e_n, 2) = 2$, (2b) determine the CEECS compute flag and starting crack coordinates SCCS, (2c) compute the CEECS, (2d) extract the adjacent elements that intersect current crack, (2e) set $\mathrm{C}_{cond}(N_{adj}, 2) = 1$, and (2f) update the crack information array C_{dbl}.

Finally, scenario (3) is identified by checking the value of C_{cond}. If $\mathrm{C}_{cond}(e_n, 2) = 2$, then the crack is evolving and the stress in the element is updated according to eq. 3.65. No other actions are necessary. See Appendix A for more details.

4.5 Complete Mesh Objective Algorithm

This section presents the complete numerical algorithm that unites the finite element equations, time integration scheme, constitutive equations, and crack tracking algorithm. The algorithm presented was programmed in FORTRAN 90/95 using a serial implementation. What will not be covered is array initialization, file input/output, and the preprocessing steps that are common in the finite element method such as reading in the mesh, applying boundary conditions, etc.

In addition, the following standard finite element computational arrays are used: A_{IECM} of dimension $N_{en} \times N_{ele}$, A_{LM} of dimension $N_{el} \times N_{ele}$, and A_{XY} of dimension $N_{node} \times N_{sd}$ where N_{en} is the number of nodes per element, $N_{el} = N_{dof}(N_{en}-1)+N_{dof}$, N_{dof} is the number of degrees of freedom per node, N_{node} is the total number of nodes, and N_{sd} is the number of spatial dimensions. In this instance $N_{dof} = 2$, $N_{sd} = 2$, $N_{en} = 4$, and $N_{el} = 8$. The array A_{IECM} is the element connectivity array that defines the global node numbers associated with each element, A_{LM} is the global

equation array that maps the global equation number to the global node number, and A_{XY} is the nodal coordinate array that defines the coordinates of each node. For a more detailed description of the computational arrays see [4]. The stress components are stored in arrays S_{xx}, S_{yy}, S_{xy} of dimension $N_{int} \times N_{ele}$, where N_{int} is the number of integration points and N_{ele} is the number of elements. The total strain components are stored in arrays E_{xx}, E_{yy}, E_{xy} of dimension $N_{int} \times N_{ele}$. The crack opening displacement is stored in array U_n of dimension $N_{int} \times N_{ele}$.

Before entering the main load/displacement increment loop, the crack tracking algorithm arrays C_{cond} and C_{dbl} and the number of initiated cracks N_{cr} are initialized to zero. The acceleration, velocity, displacement, internal/external force vectors are also initialized.

Upon entering the main load/displacement increment loop, the following steps are performed k times until the desired time $t = k\Delta t$ is reached:

1. For $i = 1$ to $N_{dof} \cdot N_{node}$, compute the i^{th} component of the acceleration vector at the previous time step k using eq. 4.68

$$a_i^k = m_i^d \left[\left(F_i^I\right)^k + \left(F_i^E\right)^k \right] - cv_i^k$$

2. For $i = 1$ to $N_{dof} \cdot N_{node}$, compute the i^{th} component of the velocity vector at the current time step $k+1$ using eq. 4.69

$$v_i^{k+1} = v_i^k + \Delta t a_i^k$$

3. For $i = 1$ to $N_{dof} \cdot N_{node}$, compute the i^{th} component of the displacement vector at the current time step $k+1$ using eq. 4.70

$$u_i^{k+1} = u_i^k + \Delta t v_i^{k+1}$$

4. Apply displacement boundary conditions by overwriting $\mathbf{u}^{k+1}$ in proper locations (ignoring applied tractions)

5. For $i_n = 1$ to N_{int} and $e_n = 1$ to N_{ele}, update the stress components and crack opening displacement $\mathrm{S}_{xx}(i_n, e_n)$, $\mathrm{S}_{yy}(i_n, e_n)$, $\mathrm{S}_{xy}(i_n, e_n)$, and $\mathrm{U}_n(i_n, e_n)$ as follows:

   (a) Compute the current total strain vector $\langle e^v \rangle = \langle e_{xx}, e_{yy}, 2e_{xy} \rangle$ using eqs. 2.21 through 2.23

$$\mathrm{E}_{xx}(i_n, e_n) = \sum_{i=1}^{4} N_{i,x} u_i$$
$$\mathrm{E}_{yy}(i_n, e_n) = \sum_{i=1}^{4} N_{i,y} v_i$$
$$2\mathrm{E}_{xy}(i_n, e_n) = \sum_{i=1}^{4} [N_{i,y} u_i + N_{i,x} v_i]$$

   (b) Compute the current stress components assuming material is elastic using eq. 4.54

$$\mathrm{S}_{xx}(i_n, e_n) = C_{11}\mathrm{E}_{xx}(i_n, e_n) + C_{12}\mathrm{E}_{yy}(i_n, e_n)$$
$$\mathrm{S}_{yy}(i_n, e_n) = C_{12}\mathrm{E}_{xx}(i_n, e_n) + C_{22}\mathrm{E}_{yy}(i_n, e_n)$$
$$\mathrm{S}_{xy}(i_n, e_n) = C_{33}2\mathrm{E}_{xy}(i_n, e_n)$$

   (c) Compute the crack orientation β, principal basis vector components n_1, n_2, t_1, t_2, and principal stresses σ_{nn}, σ_{tt} using eqs. 4.105 through 4.111

$$\beta = \frac{1}{2}\tan^{-1}\left(\frac{2\sigma_{xy}}{\sigma_{xx} - \sigma_{yy}}\right)$$
$$n_1 = \cos(\beta)$$
$$n_2 = \sin(\beta)$$
$$t_1 = \cos\left(\beta + \frac{\pi}{2}\right)$$

$$t_2 = \sin\left(\beta + \frac{\pi}{2}\right)$$
$$\sigma_{nn} = \frac{1}{2}\left(\sigma_{xx} + \sigma_{yy}\right) + \sqrt{\frac{1}{4}\left(\sigma_{xx} - \sigma_{yy}\right)^2 + \sigma_{xy}^2}$$
$$\sigma_{tt} = \frac{1}{2}\left(\sigma_{xx} + \sigma_{yy}\right) - \sqrt{\frac{1}{4}\left(\sigma_{xx} - \sigma_{yy}\right)^2 + \sigma_{xy}^2}$$

(d) Evaluate the softening function f_s using either eq. 3.73 or 3.90

$$f_s^l = 1 - \frac{u_n^k}{u_0} \qquad (\text{linear} - \text{softening})$$
$$f_s^{nl} = \exp\left(-\alpha \frac{u_n^k}{u_0}\right) \qquad (\text{nonlinear} - \text{softening})$$

(e) Evaluate the decohesion function using eq. 3.37

$$F = \frac{\sigma_{nn}}{\tau_{nf}} - f_s$$

(f) If $F < \epsilon$ ($\epsilon \approx 1 \times 10^{-5}$) then the step is elastic, update the crack opening displacement, and exit constitutive model subroutine

$$\mathrm{U}_n(i_n, e_n) = \mathrm{U}_n^k(i_n, e_n)$$

(g) Else

If $\mathrm{C}_{cond}(e_n, 1) = 0$ and $N_{cr} < N_{crall}$ then a new crack has initiated and the following steps are performed

i. Increment the current number of initiated cracks $N_{cr} = N_{cr} + 1$

ii. Set $\mathrm{C}_{cond}(e_n, 1) = 1$

iii. Set the CEECS compute flag $C_{ceecs} = 1$

iv. Set $\mathrm{C}_{cond}(e_n, 2) = 2$

v. Compute the CEECS

vi. Extract the adjacent element numbers that intersect current crack

vii. Set $\mathrm{C}_{cond}(N_{adj}, 2) = 1$

viii. Update crack information array C_{dbl}.

(h) If $C_{cond}(e_n, 2) = 1$ then an adjacent element has cracked

i. Set $C_{cond}(e_n, 2) = 2$

ii. Determine CEECS compute flag and starting crack coordinates SCCS

iii. Compute the CEECS

iv. Extract the adjacent element numbers that intersect current crack

v. Set $C_{cond}(N_{adj}, 2) = 1$

vi. Update crack information array C_{dbl}.

(i) If $C_{cond}(e_n, 2) = 2$ then the crack is evolving

i. Compute the current total strain increment components using the stored strain components at the previous step k

$$\Delta e_{xx} = E_{xx}(i_n, e_n) - E^k_{xx}(i_n, e_n)$$
$$\Delta e_{yy} = E_{yy}(i_n, e_n) - E^k_{yy}(i_n, e_n)$$
$$\Delta e_{xy} = E_{xy}(i_n, e_n) - E^k_{xy}(i_n, e_n)$$

ii. Transform the global strain increments Δe_{xx}, Δe_{yy} to local crack basis increments Δe_{nn}, Δe_{tt} as follows:

$$\Delta e_{nn} = \Delta e_{xx} n_1^2 + \Delta e_{yy} n_2^2 + 2\Delta e_{xy} n_1 n_2$$
$$\Delta e_{tt} = \Delta e_{xx} t_1^2 + \Delta e_{yy} t_2^2 + 2\Delta e_{xy} t_1 t_2$$

iii. If $C_{\text{cond}}(e_n, 3) = 1$, then cracked element is part of a cross-over, update the characteristic crack dimension h_c

iv. Compute the crack opening displacement increment using eq. 3.69

$$\begin{aligned}
\Delta u_n &= h_c \left(\Psi_n^* \Delta e_{nn} + \Psi_t^* \Delta e_{tt}\right) \\
\Psi_n &= -\frac{C_{11}}{\tau_{nf}} \\
\Psi_t &= -\frac{C_{12}}{\tau_{nf}} \\
\Psi^l &= \frac{h_c}{u_0} - \frac{C_{11}}{\tau_{nf}} && (\text{linear} - \text{softening}) \\
\Psi^{nl} &= -\frac{\alpha}{u_0} \exp\left(-\alpha \frac{\mathrm{U}^k(i_n, e_n)}{u_0}\right) && (\text{nonlinear} - \text{softening})
\end{aligned}$$

v. Compute the current crack opening displacement using eq. 3.70

$$\mathrm{U}_n(i_n, e_n) = \mathrm{U}_n^k(i_n, e_n) + \Delta u_n$$

vi. Compute stress increments $\Delta\sigma_{nn}$, $\Delta\sigma_{tt}$, and $\Delta\sigma_{nt}$ depending on state of crack

A. If $\mathrm{U}_n(i_n, e_n) \geq u_0$ then the the following stress and crack opening increments are not allowed

$$\begin{aligned}
\Delta\sigma_{nn} &= 0 \\
\Delta\sigma_{nt} &= 0 \\
\mathrm{U}_n(i_n, e_n) &= \mathrm{U}_n^k(i_n, e_n)
\end{aligned}$$

B. Else compute $\Delta\sigma_{nn}$, $\Delta\sigma_{tt}$, and $\Delta\sigma_{nt}$ using eq. 3.65

$$\begin{aligned}
\Delta\sigma_{nn} &= C_{11}\left(1 - \Psi_n^*\right)\Delta e_{nn} + \left(C_{12} - C_{11}\Psi_t^*\right)\Delta e_{tt} \\
\Delta\sigma_{tt} &= C_{12}\left(1 - \Psi_n^*\right)\Delta e_{nn} + \left(C_{22} - C_{12}\Psi_t^*\right)\Delta e_{tt} \\
\Delta\sigma_{nt} &= 0
\end{aligned}$$

vii. Transform the stress increments $\Delta\sigma_{nn}$, $\Delta\sigma_{tt}$, and $\Delta\sigma_{nt}$ back to the

global basis[3]

$$\Delta\sigma_{xx} = \Delta\sigma_{nn}n_1^2 + \Delta\sigma_{tt}t_1^2$$
$$\Delta\sigma_{yy} = \Delta\sigma_{nn}n_2^2 + \Delta\sigma_{tt}t_2^2$$
$$\Delta\sigma_{xy} = \Delta\sigma_{nn}n_1n_2 + \Delta\sigma_{tt}t_1t_2$$

viii. Compute the current stress components in the global basis and exit constitutive model subroutine

$$\mathrm{S}_{xx}(i_n, e_n) = \mathrm{S}^k_{xx}(i_n, e_n) + \Delta\sigma_{xx}$$
$$\mathrm{S}_{yy}(i_n, e_n) = \mathrm{S}^k_{yy}(i_n, e_n) + \Delta\sigma_{yy}$$
$$\mathrm{S}_{xy}(i_n, e_n) = \mathrm{S}^k_{xy}(i_n, e_n) + \Delta\sigma_{xy}$$

6. Update global internal nodal force vector, for $e_n = 1$ to N_{ele}

   (a) If $N_{int} = 1$ and $\mathrm{C}_{cond}(e_n, 2) = 0$ or $\mathrm{C}_{cond}(e_n, 2) = 1$ compute local element hourglass force vector $\{f\}_{hg}$ for uncracked element using eqs. 4.76 through 4.78

   (b) Else if $N_{int} = 1$ and $\mathrm{C}_{cond}(e_n, 2) = 2$ then compute local element hourglass force vector $\{f\}_{hgs}$ for softening element using eqs. 4.101 through 4.104

   (c) Compute the local element internal force vector $\{f\}_{int}$ using eq. 4.58

   (d) If $N_{int} = 1$ and $\mathrm{C}_{cond}(e_n, 2) = 0$ or $\mathrm{C}_{cond}(e_n, 2) = 1$ apply the hourglass force vector $\{f\}_{hg}$ to the local element force vector $\{f\}_{int} = \{f\}_{int} - \{f\}_{hg}$

   (e) If $N_{int} = 1$ and $\mathrm{C}_{cond}(e_n, 2) = 2$ apply the hourglass forces for softening $\{f\}_{hgs}$ to the local element force vector $\{f\}_{int} = \{f\}_{int} - \{f\}_{hgs}$

   (f) Map local element internal force vector components into global force vector $\{F\}^I$

7. Update variables for next increment.

[3]Because $\Delta\sigma_{nt} = 0$ the shear terms vanish.

4.6 Implementation

One advantage of the proposed algorithm is that it can be implemented easily into an existing finite element code. This is because the failure model and crack tracking portions can be included into a single constitutive model subroutine. As a result, one subroutine can be written that accepts the current strain increments (or global nodal displacements) and returns the updated stress for the next increment as well as update the necessary crack tracking arrays C_{cond} and C_{dbl}. The primary difficulty in the implementation is establishing the logic for the crack tracking algorithm. However, use of the adjacent element array E_{adj} greatly simplifies the coding and streamlines the searches required to update the crack path.

A recommended subroutine structure is to develop four crack tracking subroutines that are called within the failure model subroutine as follows: (1) *Compute-CEECS* - computes the cracked element edge coordinates that are necessary to identify the next elements slated for failure, (2) *Extract-Adjacent-Elements* - determines which elements that are adjacent to evolving cracks that are allowed to fail next, (3) *Get-Crack* - determines the crack condition flag and starting crack coordinates (SCCS) required to update the CEECS, and (4) *Update-Crack-Info* - updates C_{cond} and C_{dbl}. The crack tracking subroutines can be relatively simple that consist of no more than 30 lines of code each.

A slight modification would be necessary in the host code's hourglass control subroutine that would update the local element force vector given the hourglass control force vector for softening. The existing hourglass control approach used in most host codes for the hardening element should be sufficient. However, use of the proposed hardening hourglass control scheme might be of use as it doesn't require an hourglass coefficient and it has also demonstrated applicability to arbitrary shaped elements.

For implementation into a three-dimensional code, some alterations of the pro-

posed algorithm would be required. First, a good eigenvalue and eigenvector subroutine is required to determine the $\{\mathbf{n}, \mathbf{t}, \mathbf{p}\}$ basis and the principal stresses. Next, the strain and stress vectors now require the additional components for a three-dimensional state of stress and strain. As a result, the generalized stress transformation relations are used to map back and forth from the crack and global bases. Finally, the failure model would need to add dependence on the total strain increment Δe_{pp}. The additional shear stress increments along the crack surface are assumed zero or $\Delta\sigma_{np} = \Delta\sigma_{tp} = 0$.

The failure model, crack tracking algorithm, and hourglass control schemes can also be applied to static solvers that use iterative schemes to compute the nodal displacements such that equilibrium is achieved such as Jacobian free Newton-Krylov methods. However, these methods may require special treatment of how failure is allowed to initiate to obtain stability such as the approach used in Wellman [57].

Chapter 5

Results

This chapter presents the results obtained using the algorithm provided in Section 4.5. First, the efficacy of the hourglass control scheme for the hardening element is investigated by comparing solutions obtained with full integration and the hourglass control scheme provided in [50].

Next, a two-dimensional model problem of a bar pulled in tension with a crack initiating in the center is examined to evaluate the proposed algorithm. Several different meshes are chosen to evaluate the sensitivity of the crack path and load deflection curve to the orientation and size of the finite element mesh. Finally, the effects of the characteristic element size are studied.

A double-edge notched (DEN) direct tension concrete experiment is simulated next to investigate the ability of the algorithm to propagate straight cracks that are initiated from geometric discontinuities. A couple of mesh orientations are investigated.

Finally, a DEN shear-tension concrete experiment is examined to investigate the algorithm's ability to model curved crack trajectories. This experiment is composed of a dual-stage load path that consists of first loading the specimen in shear. Then the shear is held fixed while the specimen is stretched in tension.

5.1 Hourglass Control for Hardening Element

Consider a two-dimensional unit bar with sides equal to 1 and thickness $t_e = 1$ as shown in Figure 5.1. The left side is fixed in the x and y directions such that $u(0, y, t) = v(0, y, t) = 0$. The right side is fixed in the y-direction and the displacement in the x-direction at $x = 1$ is incremented such that $u(1, y, t) = u_{end}(t) = v_c t$ where $v_c = 0.0001$. The traction along the top and bottom is equal to zero. The Poisson's ratio, density, Young's modulus, and damping coefficient are respectively equal to $\nu = 0.3$, $\rho = 1$, $Y = 1$, and $c = 4$. Let's also assume that the initial velocity everywhere is zero. The imposed boundary conditions will cause the bar to expand axially and contract laterally. Let's consider two discretizations one with rectangular elements and the other with elements that are slanted at a varying angle as respectively shown in Figures 5.2(a) and 5.2(b). The simulation is run until the end of the bar reaches a displacement of 0.02. For each mesh, three sets of simulations are completed as follows: (1) four-point quadrature, (2) one-point quadrature using the

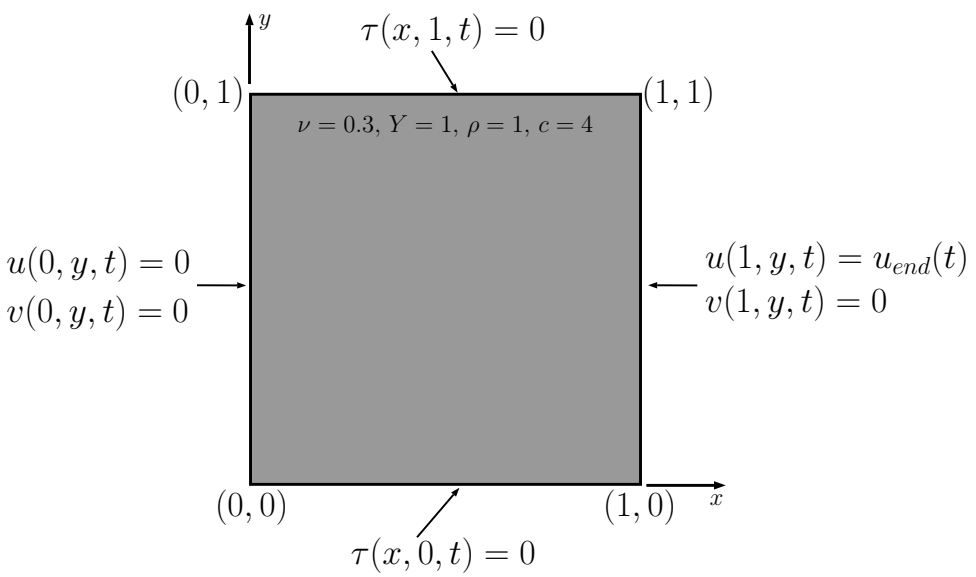

Figure 5.1: Unit Bar Pulled in Tension

HGC method by Flanagan and Belytschko [50] and denoted FB, and (3) one-point quadrature using the HGC method proposed in Section 4.3.1. For each simulation set in (2), several runs are performed that increment the hourglass coefficient κ between 10 and 15 at intervals of 0.25. Similarly, a fictitious hourglass coefficient κ_f is used to perturb the solution for the new HGC method with κ_f incremented at 0.025 between 0.8 and 1.2. Recall that the proposed HGC method does not require an actual hourglass coefficient.

An error vector $\mathbf{e}^{hgc}$ is established by comparing the solution vector obtained using four-point integration to the solution obtained from one-point integration written as $\mathbf{e}_{hgc} = \mathbf{u}^4(x, y, t_{end}) - \mathbf{u}^1(x, y, t_{end})$, where t_{end} is the problem end time. With the mesh size fixed, the vector L2-norm is used to establish a scalar error metric as follows:

$$E_{hgc} = \left(\sum_{i=1}^{2N_{node}} \left| e_i^{hgc} \right| \right)^{1/2} . \tag{5.1}$$

The error norm is plotted against the normalized hourglass coefficient for both the rectangular and slanted meshes in Figure 5.3. The FB hourglass coefficient κ was normalized by dividing by the hourglass coefficient that produced the smallest error or 12.3 for the square mesh and 12.0 for the slanted mesh. The fictitious hourglass coefficient κ_f was not normalized.

The results for the rectangular mesh plotted in Figure 5.3(a) show that the proposed HGC method for the hardening element provides essentially zero error. However, the FB hourglass control method cannot reproduce full-integration as noted in a nonzero minimum error at a normalized hourglass coefficient of 1. This response occurs because FB only uses one hourglass coefficient. If eqs. 4.89 and 4.90 are used to find the hourglass coefficients that reproduce full-integration for a modified FB with two hourglass coefficients, then $\kappa_1 = 15.56$ and $\kappa_2 = 10.06$.

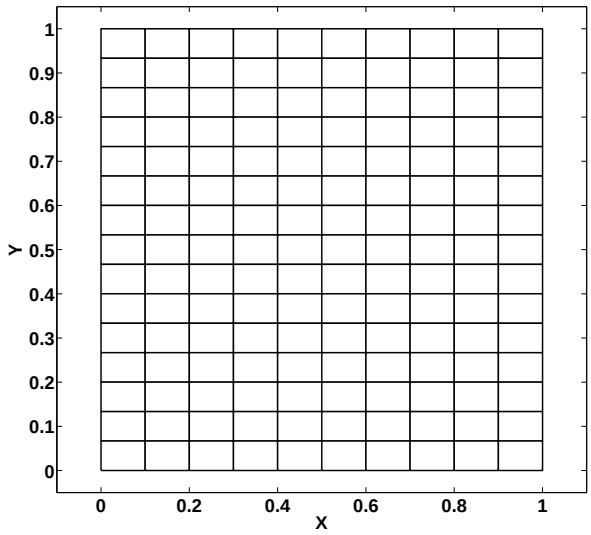

(a) Rectangular Mesh

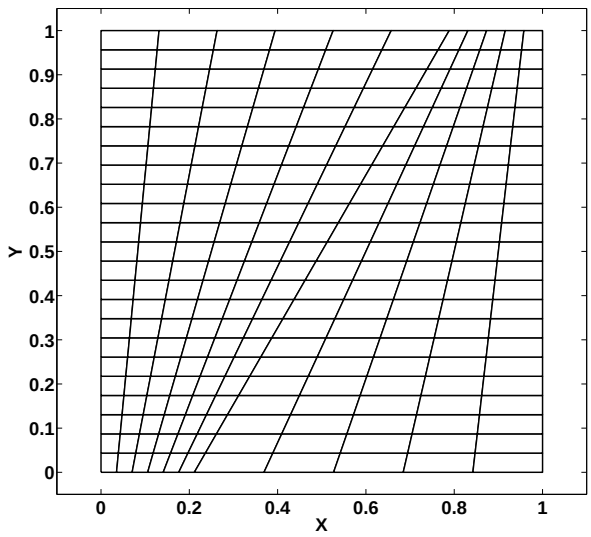

(b) Slanted Mesh

Figure 5.2: Meshes Used in Hourglass Control Studies

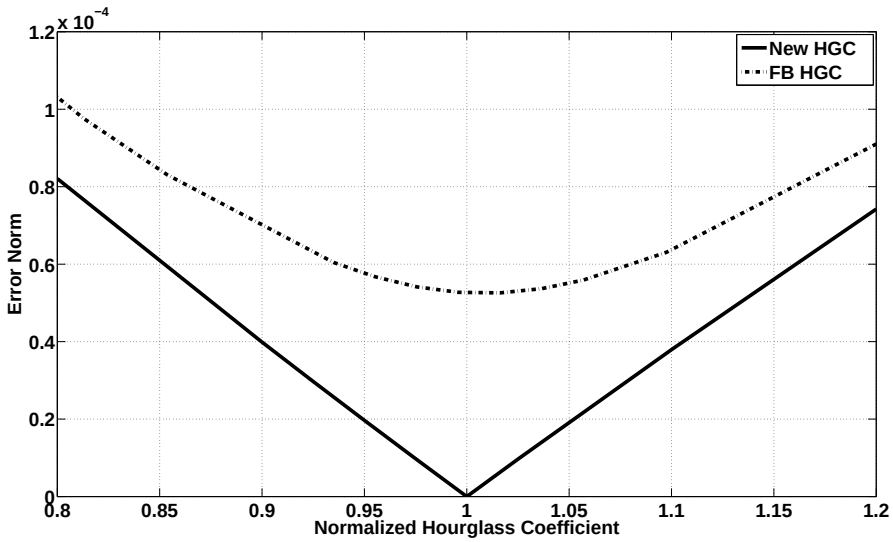

(a) Rectangular Mesh

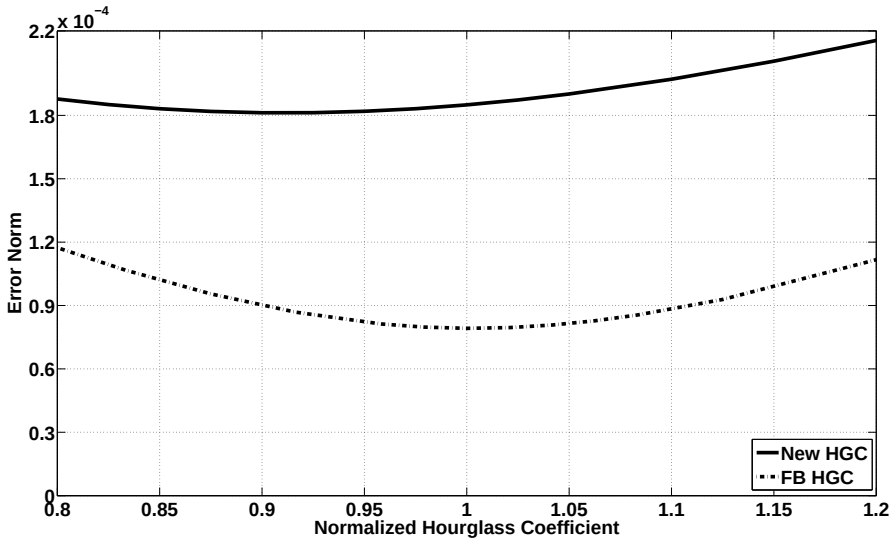

(b) Slanted Mesh

Figure 5.3: One-point Integration Error: Hardening Element

Finally, the error norm for the slanted mesh is shown in Figure 5.3(b). For the slanted mesh, now the proposed HGC method contains more error than FB. This is not surprising because the proposed HGC method assumes that the elements are either square, rectangular, or parallelograms. These results show that if the mesh is composed of structured square, rectangular, or parallelogram elements, then the propose HGC method will provide no integration error. However, for arbitrary element geometries, the error in the FB HGC method is expected to be smaller. However, for the problems considered here, the proposed hourglass scheme worked equally well to the FB method. The general comment is that the differences in the results (e.g. load-deflection curves) between the FB and proposed methods are nearly indistinguishable.

The HGC method proposed for the hardening element can be thought of as an alternative to other approaches. The primary benefit of the proposed hourglass method is that an hourglass coefficient isn't necessary. In addition, the method reproduces four-point quadrature using simple analytical equations for structured meshes. Some computational speedup due to the smaller number of floating point operations has been observed. Estimated speedup is on the order of 5% based on compute time measurements. For static iterative solvers, the reduced integration error might provide further benefits by reducing the number of iterations to obtain convergence. These observations were noted in crack propagation simulations that employed a Jacobian free Newton-Krylov solver using the proposed HGC method.

5.2 Mode-I Failure Model Problem

This section is devoted to investigating the performance of the proposed algorithm for modeling mode-I failure in a two-dimensional bar. This particular problem provides an indication of how the algorithm will perform in more general problems that involve propagating cracks at an angle through a finite element mesh. The effects of mesh

size and orientation are investigated followed by studies of the proposed hourglass control scheme and characteristic crack dimension.

5.2.1 Effects of Mesh Orientation and Size

We choose a model problem that allows a focused examination of the effects of both mesh size and orientation as shown in Figure 5.4. A slender bar is chosen such that the shear stress near the ends of the bar are minimal for a nonzero Poisson's ratio. The left end of the bar is held fixed in the x and y directions while at the right end of the bar, the displacement is prescribed with $u(1, y, t) = v_c t$ with $v_c = 0.0001$. The bar is allowed to laterally contract at $x = 1$. The top and bottom surfaces are traction free.

A crack is initiated in the center of the bar by reducing the tensile strength τ_{nf} of the center element. The crack is then allowed to propagate across the bar in a manner predicted by the crack tracking algorithm. The material properties are shown in Figure 5.4 where $\nu = 0.2$, $Y = 1$, $\rho = 1$, $\tau_{nf} = 0.011$, $c = 4$, and the tensile strength of the element that initiates failure $\tau_{nf}^{f} = 0.01$. The following meshes are considered with maximum slant angle γ as follows: (1) $\gamma = 0$, (2) $\gamma = 30^o$, (3) $\gamma = 60^o$ where the maximum slant angle γ occurs in the center of the bar. For each rotation, three different meshes each containing $N_x \times N_y$ elements in the x and y direction, respectively as follows: (i) 11×5, (ii) 23×11 and (iii) 47×23. One-point integration is used with the proposed hourglass control methods. For comparison purposes, the results obtained using a standard decohesion failure model are also shown where noted. The particular standard decohesion failure model used is listed in Appendix B. The performance metrics are the load-deflection curves and the predicted crack path.

To investigate the effects of mesh orientation and size, for each mesh size, the load-deflection curves are plotted for all mesh slant angles as shown in Figure 5.5.

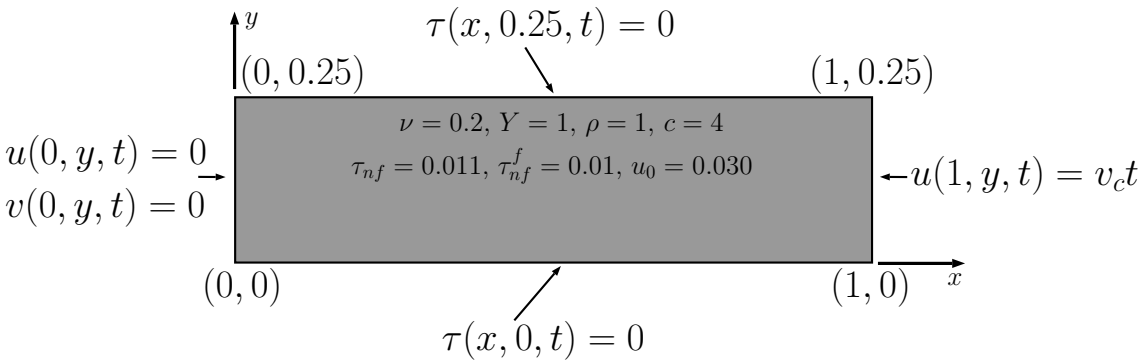

Figure 5.4: Slender Bar Pulled in Tension

The results provided in Figure 5.5 show that there is essentially no sensitivity to the orientation of the mesh. The differences in the predicted peak load are attributed to the mesh size and not the mesh orientation because as the mesh is refined, these differences become smaller. The predicted crack paths are shown with a black line in Figure 5.6 for the 47×23 mesh for all mesh orientations. The crack paths shown in Figure 5.6 are formed by plotting the cracked element edge coordinates (CEECS) and connecting them with a line segment. The results show that the predicted crack path is mesh objective.

To compare the proposed failure model with a standard decohesion model, the load deflection curves for the 23×11 mesh are plotted for $\gamma = 30$ and $\gamma = 60^o$ in Figure 5.7. Notice that the standard model cannot even predict softening in the bar. This is due to the accumulation of parasitic shear stress that leads to shear locking. The results get progressively worse as the mesh orientation is increased. This shows that the standard approach contains significant mesh orientation bias as compared to the proposed approach. A detailed comparison between the standard and proposed failure models is conducted in Appendix B.

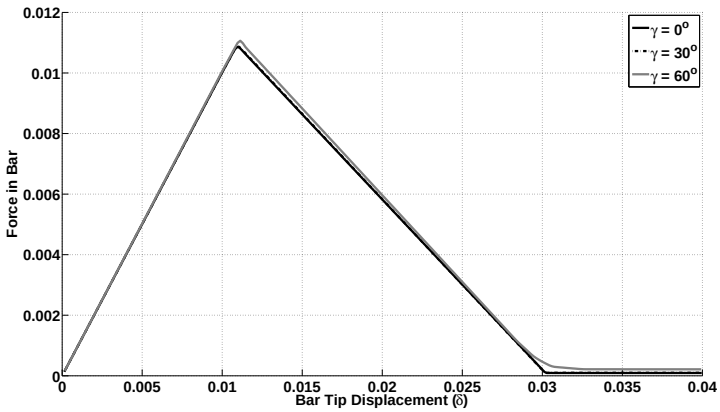

(a) 11 × 5 mesh

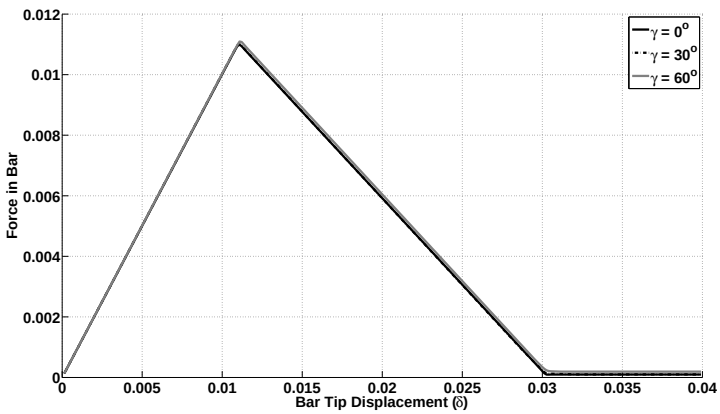

(b) 23 × 11 mesh

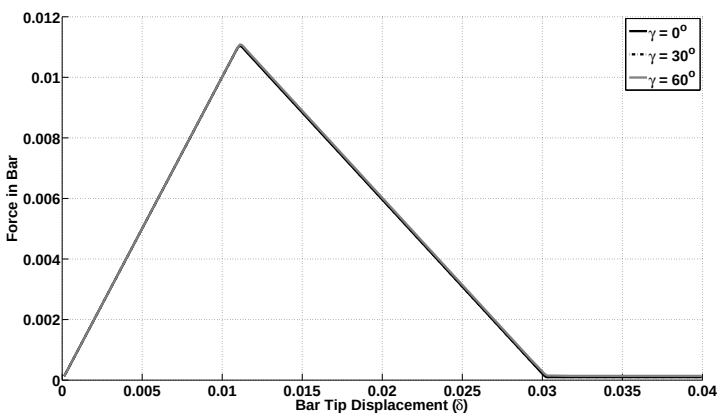

(c) 47 × 23 mesh

Figure 5.5: Effect of Mesh Orientation on Load Deflection Curve

Examining the mesh distortion during the the later stages of the failure process is also a valuable metric to gage how well the algorithm is performing. What we seek is to have the crack open up in the proper direction without distorting the mesh. For the present problem, this means that the crack should open horizontally. Figure 5.8 compares the final state of the mesh at $U_{end} = 0.04$ for a displacement scaling factor of 5 for the proposed and standard model failure for $\gamma = 30$ and $\gamma = 60^o$. Notice that in Figure 5.8(a), the standard model provides a distorted crack opening. For $\gamma = 60^o$, the standard model cannot introduce a crack opening due to the extent of shear locking as shown in Figure 5.8(c). In contrast, the proposed model provides essentially the same crack opening regardless of mesh orientation as shown in Figures 5.8(b) and 5.8(d)

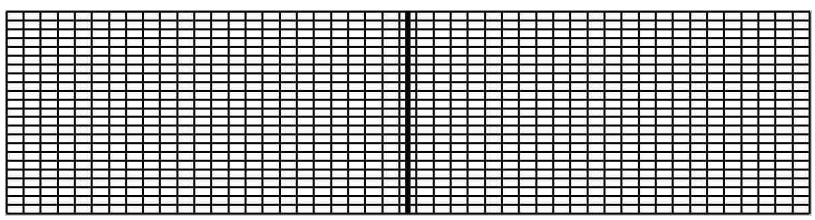

(a) $\gamma = 0^o$

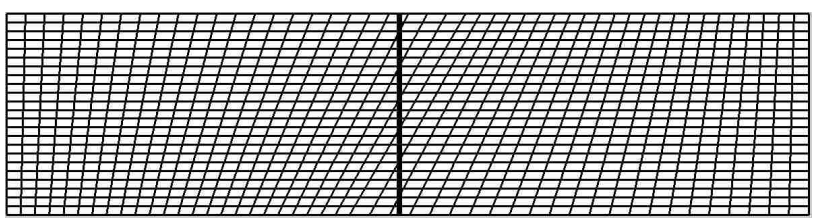

(b) $\gamma = 30^o$

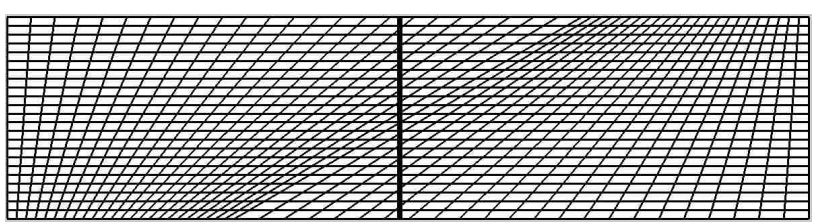

(c) $\gamma = 60^o$

Figure 5.6: Predicted Crack Paths

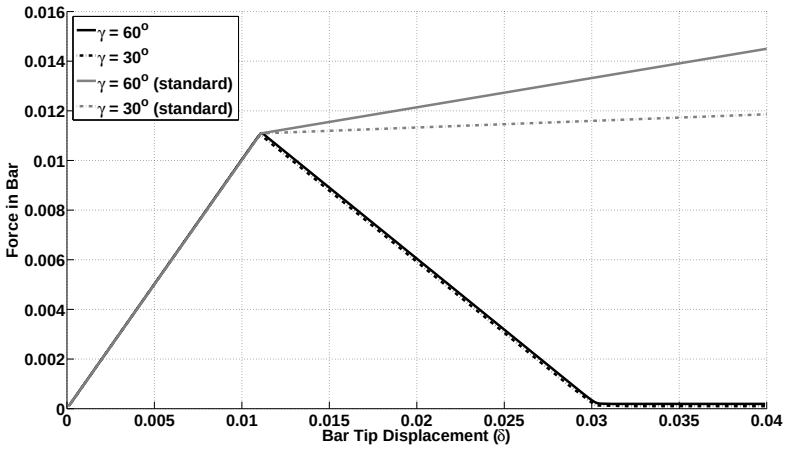

Figure 5.7: Proposed Model vs. Standard Model

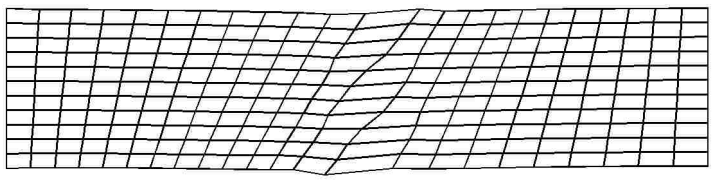

(a) Standard Model: $\gamma = 30^o$

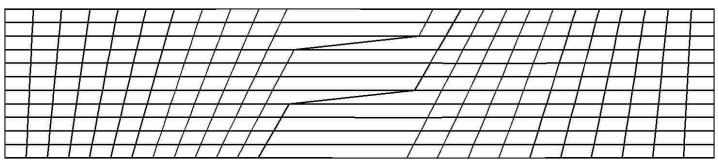

(b) Proposed Model: $\gamma = 30^o$

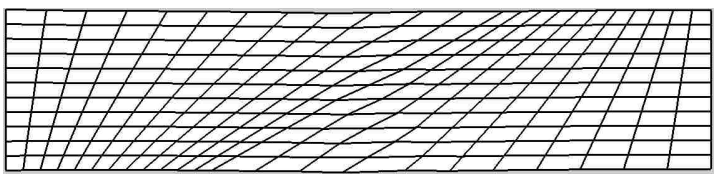

(c) Standard Model: $\gamma = 60^o$

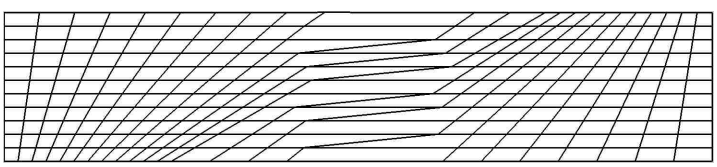

(d) Proposed Model: $\gamma = 60^o$

Figure 5.8: Final Mesh State at Full Crack Opening

5.2.2 Effects of Characteristic Crack Dimension

The characteristic crack dimension h_c plays an important role in crack propagation problems. When crack cross-overs occur, it is important to adjust h_c such that the crack dimension is equal to the sum of the element dimensions h that compose the cross-over. We denote adjusting h_c for cross-over cracks as *cross-over scaling* or COS. This section will examine the effects of cross-over scaling and its role in obtaining mesh objectivity.

First, let's examine more closely the implications of adjusting h_c. In this instance for linear softening, the key crack tangent modulus component from Section 3.3 is restated here as

$$C_{11}^{cr} = C_{11}\left(1 - \Psi_n^*\right) = C_{11}\left(1 - \frac{\Psi_n}{\Psi_l}\right) = C_{11}\left(1 - \frac{1}{1-\kappa}\right), \tag{5.2}$$

where

$$\kappa = \frac{h_c \tau_{nf}}{u_0 C_{11}}. \tag{5.3}$$

For softening and no snapback where snapback is defined to be the case where $C_{11}^{cr} > 0$, we require $\Psi^* > 1$ or $\kappa < 1$, which leads to the following inequality obtained in eq. 3.86,

$$h_c < \frac{C_{11} u_0}{\tau_{nf}}.$$

If κ is increased, subject to the constraint on h_c, then the magnitude of the softening slope is also increased. For the cross-over case, the characteristic crack length is the sum of the element dimensions that compose the cross-over. An increase in h_c automatically adjusts the increase in softening slope and the dissipated fracture energy for the two elements is equivalent to the fracture energy dissipated in one element. As a result, the energy dissipated in the cross-over becomes consistent to the energy dissipated in adjacent cracked elements that consist of only one element. As will be seen in the results that follow, this rather simple modification has extensive and important implications.

We will consider the 23×11 mesh from Section 5.2.1 with orientations of $\gamma = 30$ and $\gamma = 60^o$. Two cases will be considered for each orientation: (a) with COS for crack cross-overs such that h_c is the total width of the cross-over and (b) without COS.

The results are shown in Figure 5.9. Notice that when the dimension of the crack is adjusted properly for cross-overs in case (a), the 30 and 60^o meshes obtain essentially the same load-deflection curve indicating that the stress in the bar is decaying to zero. However, when the crack dimension is not adjusted for cross-over cracks, then there is mesh orientation bias. The mesh orientation bias becomes increasingly worse as the mesh orientation increases for case (b). This suggests that without cross-over scaling, mesh objectivity cannot be achieved.

A stiffening response is obtained for case (b) indicating that normal stress is accumulating in the bar as the crack opens. Figure 5.10 compares the normal stress σ_{xx} in the bar for $\delta = 0.04$. Notice that with COS turned on, the normal stress in the bar is uniform and close to zero. However, with COS turned off, large normal stresses are centered around crack cross-overs. This suggests that there is an inconsistency in the rate of unloading between cross-over elements and adjacent cracked elements. By increasing h_c for all elements within the cross-over, this causes the cross-over elements to unload at the same rate as adjacent elements and as a result there is no spurious normal stress accumulation. This was the final piece of the puzzle that provided complete mesh objectivity.

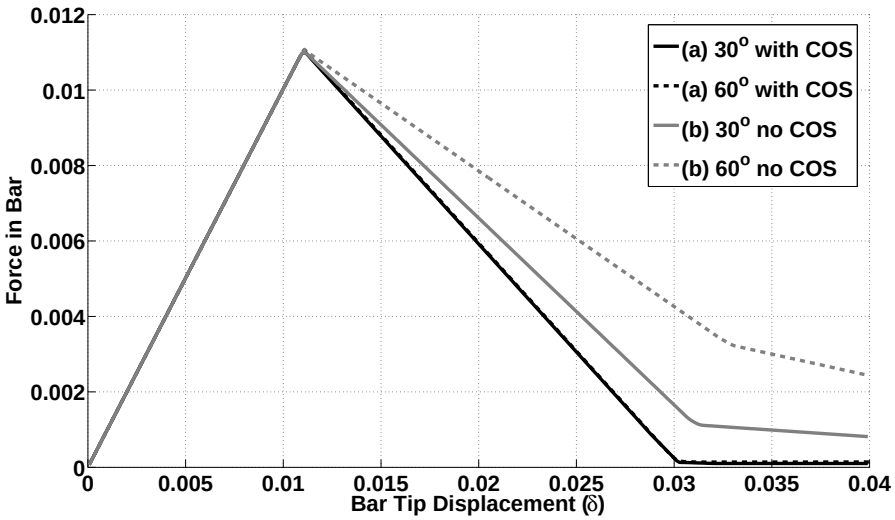

Figure 5.9: Effects of Characteristic Crack Dimension h_c

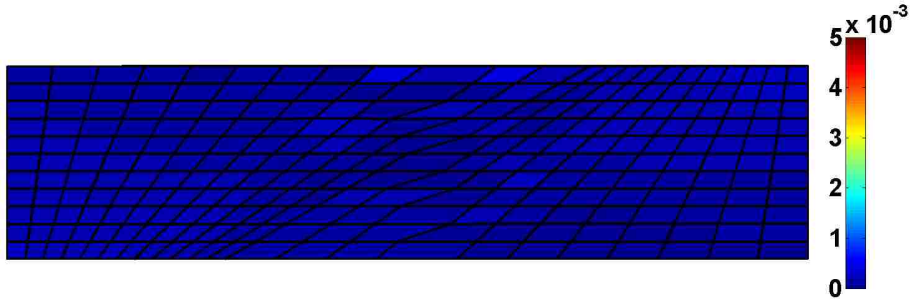

(a) with COS

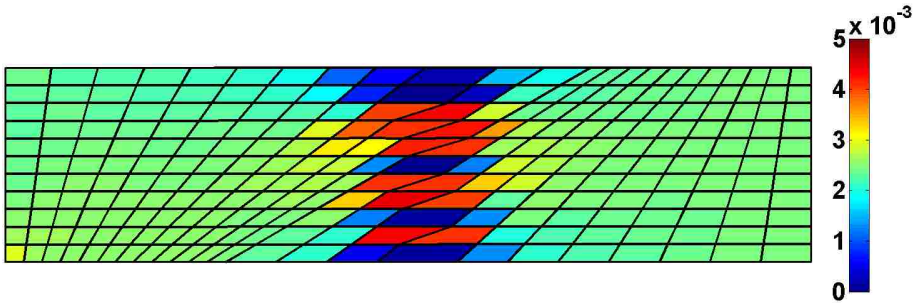

(b) without COS

Figure 5.10: Spurious Normal Stress Without Cross-over Scaling

5.3 Double-Edge-Notch Direct-Tension

So far we have dealt with initiating a crack by reducing the tensile strength of one element, which causes a crack to propagate through the mesh. Now we turn to real experiments where a crack initiates due to a stress concentration brought on by a geometric discontinuity. A detailed and thorough research effort to characterize brittle material failure of double-edge-notch (DEN) concrete specimens was conducted by Nooru-Mohamed [58] in the early 1990s. Here we simulate experiments from [58] that focus on $0.2 \times 0.2 \times 0.050$ m concrete specimens possessing two 0.025×0.005 m notches as illustrated in Figure 5.11.

The first loading case examined in this section is of direct tension where the specimen is pulled axially in tension under displacement control. Platens that are glued to the top and bottom surfaces are used to apply the controlled displacement. The tensile force and the crack opening displacement are both monitored throughout the duration of the experiment. The displacement δ_c, shown in Figure 5.11, is defined as the crack opening displacement. Finite element simulations of the experiment were conducted by applying a uniform displacement over the bottom edge of

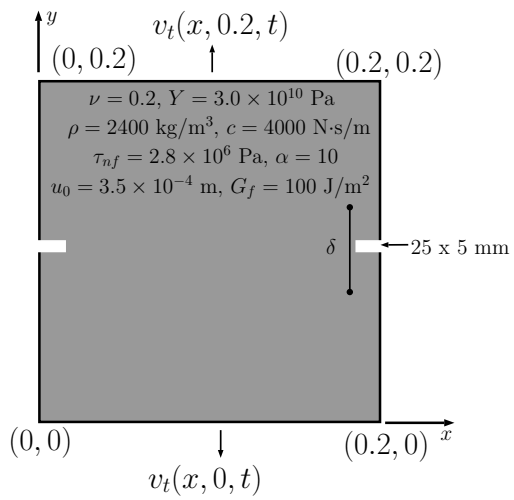

Figure 5.11: DEN Direct-Tension Problem Setup

$v(x, 0, t) = -v_c t$ and over the top edge of $v(x, 0.2, t) = v_c t$ with $v_c = 0.00025$ m/s. The horizontal displacement along the bottom and top edges were set to zero or $u(x, 0, t) = u(x, 0.2, t) = 0$. Traction free boundary conditions were assumed on the left and right edges or $\boldsymbol{\tau}(0, y, t) = \boldsymbol{\tau}(0.2, y, t) = 0$.

The elastic material properties assumed were $\rho = 2400$ kg/m^3, $Y = 3.0 \times 10^{10}$ Pa, and $\nu = 0.2$. Viscous damping is applied assuming a damping coefficient of $c = 4000$ N $\cdot$ s/m. Nonlinear softening was used with $\tau_{nf} = 2.8 \times 10^6$ Pa, $\alpha = 10$, and $u_0 = 3.5 \times 10^{-4}$ m. Note that a fracture energy of $G_f = 100$ J/m^2 was used to compute u_0 using eq. 3.98.

Two 41×41 meshes with $\gamma = 0$ and $\gamma = 30^o$ were used to discretize the concrete specimen. Each mesh consisted of 1671 quadrilateral elements and 1764 nodes. Note that the oriented mesh is shown later in Figure 5.13(b). One-point quadrature was used with the proposed hourglass control methods for hardening and softening. The crack tracking algorithm with cross-over scaling was also used. Another simulation was ran with hourglass control for softening (HGCS) turned off for the 30^o mesh to illustrate the importance of hourglass control for mesh objectivity.

The resulting load-deflection curves are shown in Figure 5.12 with the experimental data. We first note that the load-deflection curves for the 0 and 30^o meshes are nearly the same. This demonstrates that the proposed algorithm is obtaining results that are not sensitive to the orientation of the mesh. Next, notice that the load-deflection curve for the 30^o mesh without hourglass control is different than the other curves that use hourglass control for cracked elements. This shows that without hourglass control employed for cracked elements, there is some mesh orientation sensitivity.

We next discuss the differences between the predicted load-deflection curve and the experimental data of which we assume is accurate. First, the predicted load of the specimen during load-up between $\delta = 0$ and $\delta = 0.01$ mm is smaller than what was measured in the experiment. Upon initial loading for $\delta < 0.002$ mm,

the predicted load matches that of the experiment which would correspond to elastic material behavior. However, as the peak load is reached, the predicted curve becomes somewhat shifted in δ as compared to the measured response. This may be attributed to a more localized region of failure initiation in the specimen during the experiment as compared to what was assumed in the simulation. In the simulation, failure initiates in a single element within the root of each notch, which is rather large. This element fails well before the peak load is reached and this plays an important role in the shape of the load-deflection curve prior to the peak load. If a greater portion of the material is assumed to initiate failure, this perhaps generates a softer response as compared to the experiments.

For large δ, the shape of the load-deflection curve as measured in the experiments is no longer an exponential function. Because the failure model assumes an exponential function for all δ, it isn't surprising that the predicted load-deflection curve diverges from experimental data for large δ. A simple modification to the softening function that provides a nonzero contribution for large δ would offer more accurate results. However, the key point is that using a simple algorithm and relying on material properties alone, the key features observed in experimental data are predicted reasonably well without mesh orientation bias.

The normal stress contours are provided for both meshes for a few different simulation steps in Figure 5.13. The scale has been left off for clarity, but the minimum normal stress equal to zero is represented with a blue color and the maximum stress equal to $\tau_{nf} = 2.8 \times 10^6$ Pa is represented with red. The left column shows normal stress contours for $\gamma = 0^o$ and the right column shows normal stress contours for $\gamma = 30^o$. The results at the same simulation step are shown for comparison. Note that the displacements have been scaled by 400 to highlight the crack opening. The results show that the normal stress contours are very similar for the two meshes further demonstrating mesh objectivity. In addition, the displacement δ obtained from the two meshes are essentially the same as noted in the captions for Figure

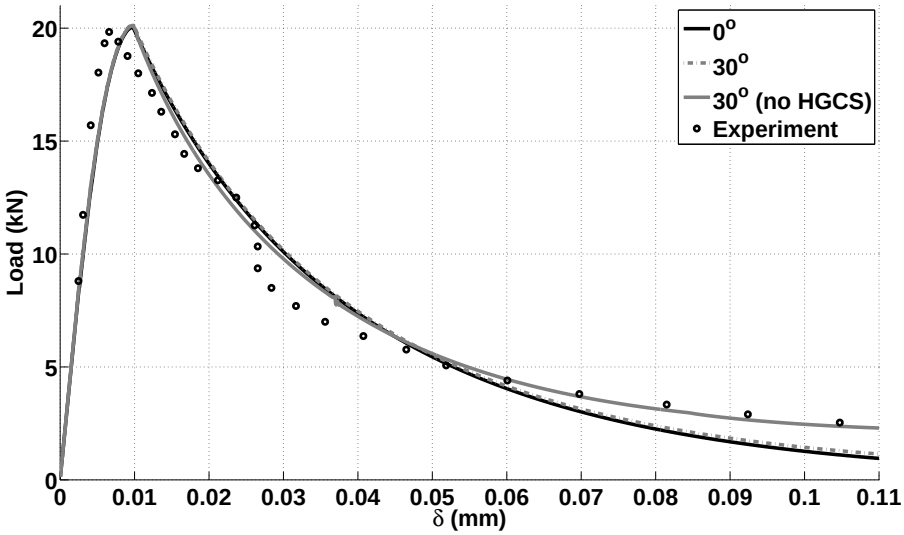

Figure 5.12: Load-deflection Curve - DEN Direct Tension

5.13. For the 30^o mesh, there are a few uncracked elements along the crack that have slightly higher normal stress than the bulk material. The locations of these *hotspots* are near crack cross-overs. It is suspected that even though cross-over scaling dramatically reduces the effects associated with crack cross-overs, the approach employed isn't exact. As a result, there will be some elements that may contain slightly higher normal stresses. However, this only mildly affects the resulting load-deflection curve. Future research could improve the cross-over scaling methods such that these hotspots are completely removed. It is noted that stress contours are typically not provided for crack propagation problems in the literature especially for different mesh orientations.

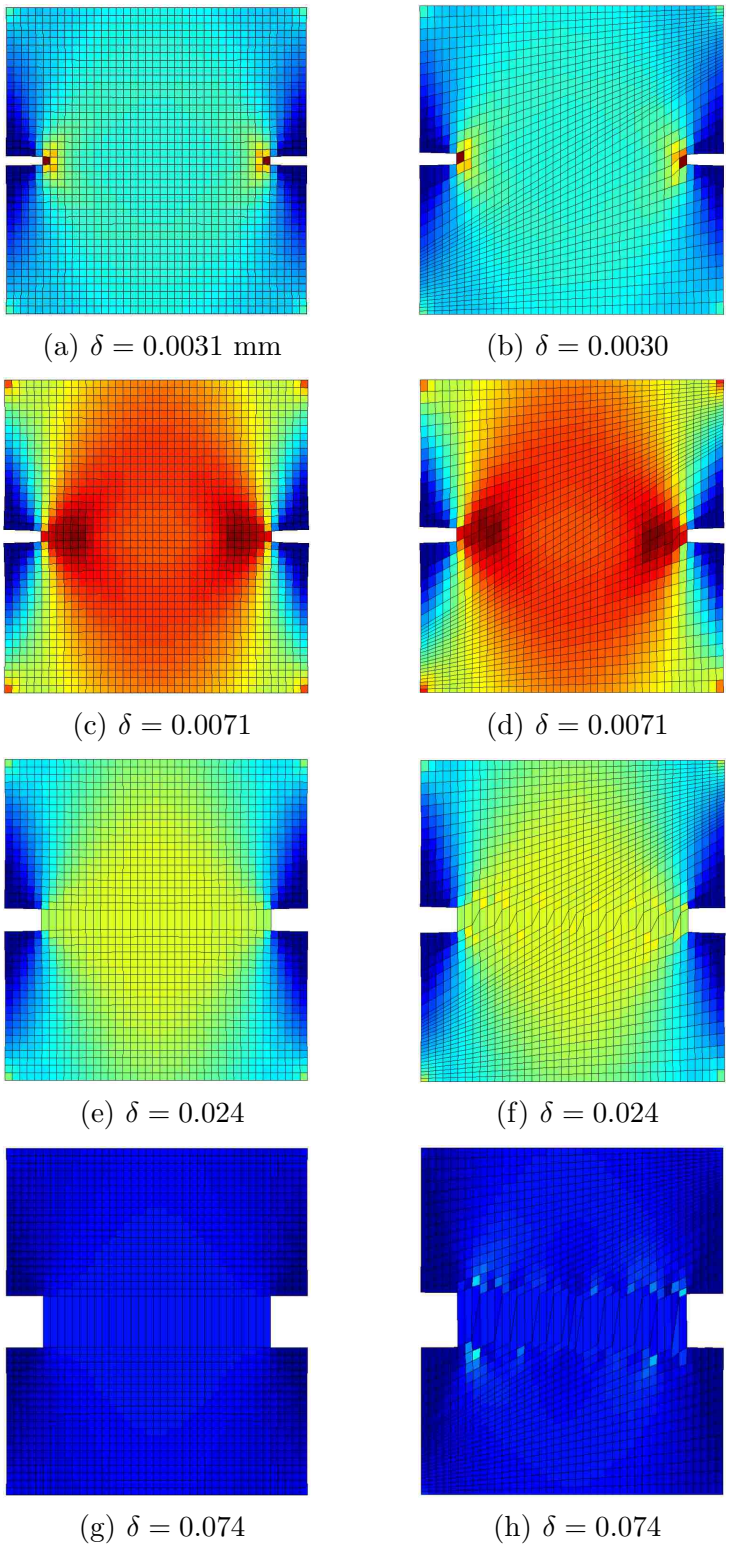

(a) $\delta = 0.0031$ mm (b) $\delta = 0.0030$

(c) $\delta = 0.0071$ (d) $\delta = 0.0071$

(e) $\delta = 0.024$ (f) $\delta = 0.024$

(g) $\delta = 0.074$ (h) $\delta = 0.074$

Figure 5.13: Normal Stress - DEN Direct Tension Simulations (scale factor = 400)

5.4 Double-Edge-Notch Shear-Tension

In the previous section, the loading conditions were such that a crack propagated straight across the DEN specimen. In this section, we examine the algorithm's ability to predict curved crack trajectories by adding a shear loading stage. The experiments were conducted under load path 4 as described in [58]. The DEN specimen geometry is identical to that of Section 5.3. The only difference is the boundary conditions imposed on the specimen.

The loading of the specimen consists of two loading stages. In the first stage, controlled lateral displacements u_s are applied uniformly to the top-left and bottom-right surfaces of the specimen as shown in Figure 5.14 such that the specimen is put into a state of lateral shear. The axial displacements are then controlled such that the net force acting on the specimen in the y-direction is zero. The lateral force is monitored while the lateral displacements are being applied. After the desired lateral force F_s is obtained, the second loading stage begins.

In the second loading stage, the lateral force F_s is held constant while the speci-

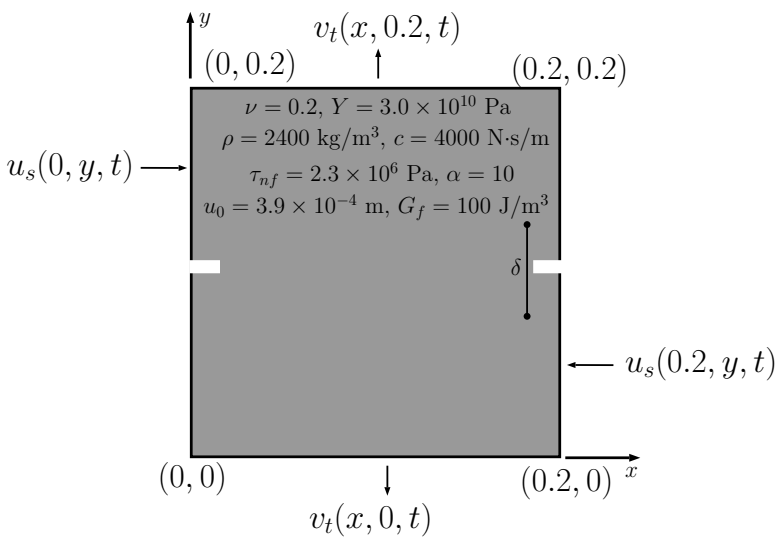

Figure 5.14: DEN Shear-Tension Problem Setup

men is pulled in tension. The lateral displacements are adjusted such that the lateral force is held at F_s while the top and bottom surfaces are placed under displacement control. As the specimen cracks, the lateral displacements are appropriately adjusted to provide a constant lateral force.

This presents a challenging set of boundary conditions for the finite element simulations. Because the effective stiffness of the specimen is nonlinear due to the formation of cracks, an iterative method must be added to the main load increment loop that computes u_s such that a constant lateral force is maintained as the specimen cracks. A secant algorithm was chosen that is essentially Newton's method that approximates the derivative of the residual with respect to the lateral displacement. A residual is formed by taking the difference between the lateral force set point F_s and the calculated lateral force obtained by summing the normal stress-area products of all the elements that compose the lateral surfaces. The iterations continue until the residual is less than a specified tolerance.

The loading of the specimen goes as follows in the finite element simulations. Lateral displacements $u_s(0, y, t) = v_s t$ and $u_s(0.2, y, t) = -v_s t$ are prescribed with $v_s = 0.0002$ m/s for $0.105 \leq y \leq 0.2$ and $0 \leq y \leq 0.095$ m, respectively. At the same time, axial displacements $v_t(x, 0, t)$ and $v_t(x, 0.2, t)$ are proportionally prescribed such that the net axial force is close to zero. Because the stiffness of the material is nearly constant during the first loading stage, a proportionality constant that relates v_t to u_s is used to keep the axial force close to zero. Once the lateral force is greater than the set point F_s, then the axial displacements $v_t(x, 0, t)$ and $v_t(x, 0.2, t)$ are incremented starting from where they left off from the first loading stage. The secant algorithm iterations are then performed for all subsequent time steps that control the magnitude of $u_s(0, y, t)$ and $u_s(0.2, y, t)$ for every increment in the axial displacements v_t such that a constant lateral force is maintained. Note that it is assumed that $u_s(0, y, t) = -u_s(0.2, y, t)$.

The material properties used in the DEN direct-tension simulations in Section

5.3 were carried over with the exception of the tensile strength. In [58], it was observed that in experiments which used four platens, the measured tensile strength was smaller than experiments that only used two platens. Note that the extra two platens are placed along the lateral edges for $0.105 \leq y \leq 0.2$ and $0 \leq y \leq 0.095$ m, respectively. In the DEN shear-tension experiments, four platens were used. As a result, the tensile strength was scaled based on direct tension experiments obtained using four platens to $\tau_{nf} = 2.3 \times 10^6$ Pa with a corresponding $u_0 = 3.9 \times 10^{-4}$ m.

The material properties used here were $\rho = 2400$ kg/m^3, $Y = 3.0 \times 10^{10}$ Pa, and $\nu = 0.2$. Viscous damping was applied assuming a damping coefficient of $c = 4000$ N $\cdot$ s/m. Nonlinear softening was used with $\tau_{nf} = 2.3 \times 10^6$ Pa, $\alpha = 10$, and $u_0 = 3.9 \times 10^{-4}$ m.

Various meshes were chosen to investigate sensitivity to mesh size. Square meshes of 23×23, 41×41, and 82×82 were chosen. Two different lateral shear loads of 5 and 10 kN were studied. Note that for the 23×23 mesh, the notch size was 0.026×0.009 m, which is larger than the actual notch size of 0.025×0.005 m.

The resulting load deflection curves for lateral shear forces $F_s = 5$ and 10 kN are shown in Figures 5.15 and 5.16, respectively. The experimental data is also provided. Note that for the 10 kN case, there are two experimental data sets shown which represent two separate experiments of similar concrete materials. Observing Figure 5.15, the predicted load-up is stiffer than the experimental result. This is in contrast to the DEN direct-tension experiments in which the predicted load-up response was softer than what was measured. This might suggest that the material damage that occurs in the experiment during nucleation and propagation of microcracks is more diffuse than what is assumed in the simulation. The simulation assumes that failure initiates only in two locations located near the notch root. As a result, the quantity of microcracks within the actual experiment could be much larger of which would create a softer loading response. It is emphasized that failure initiation occurs before the peak load is reached. Recall that the discrete failure model is an approximation to

the complex nucleation of microcracks that do not necessary occur on a single failure plane. Therefore, it isn't too surprising that there is some error in the predicted load-up response of which includes this complex material failure process. The key point is that even with an approximate failure model and a relatively coarse mesh, the features observed in the experiments can be predicted with relatively little mesh dependence.

The predicted stress contours suggest that for the most part, the stress distribution within the concrete specimen is mesh objective. In Figures 5.17 and 5.18, the normal stresses for the 82×82 mesh are shown in the left column and the normal stresses for the 41×41 mesh are shown in the right column for a shear load of $F_s = 5$ kN. The minimum scale value was set to -2.3×10^6 Pa and is represented with blue colors. The maximum scale was set to 2.3×10^6 Pa and is represented with red colors. A state of zero stress is represented by green. The normal stress contours provided in Figure 5.17 highlight the propagation of the crack as shown in the localized region of high normal stress at the crack tip. Note that the displacements have been scaled by a factor of 200 to highlight the crack opening.

For the 82×82 mesh, there is a small region of large normal stress (σ_{yy}) near the notch. The coarser 41×41 mesh does not possess as strong of stress magnitudes within these areas. It is suspected that this feature is caused from not allowing the crack to propagate away from the notch towards the left and right sides of the specimen. The crack gets essentially pinned or stuck and as a result stress accumulates near the notch. We suspect that it is the higher stresses within this region that causes the load-deflection curve to shift upward as the mesh is refined. The fact that the stress distributions in the 41×41 and 82×82 meshes are similar further suggests that the shift in the load-deflection curve is a result of the larger localized stresses in the notch area. These effects get worse as the lateral load increases. We do not believe that the shift in the load deflection curve is caused by mesh bias due to the crack propagation. Fixing this is a matter of fine-tuning the

crack tracking algorithm to allow additional cracks to form around the notch.

Observing the normal stresses (σ_{xx}) in Figure 5.18 shows a transfer of stress into the center of the DEN specimen once the crack begins to propagate. This suggests that once the microcrack forms, the center portion of the specimen goes into compression due to applied lateral compressive load. As the microcrack continues to propagate and open, the material that is adjacent to the crack goes into tension. If cracks were allowed to form in this region, then other microcracks would initiate and the stresses in these areas would decrease.

The shear stress (σ_{xy}) is plotted in Figure 5.19. Upon crack initiation at each notch, there is a large shear stress where the crack orientation is greatest. As the crack propagates, this shear stress increases in expanse. It is noted that the shear stress where the crack normal is nearly parallel to the y-axis or vertical is close to zero. Large shear stresses accumulate in areas where the crack normal contains the largest orientation. This would be consistent to what is allowed in the failure model. Once the crack orientation $\mathbf{n}$ is parallel to the y-axis, then we would expect that the shear in the global basis σ_{xy} to be close to zero. This is what we observe in Figure 5.19. Note that the large shear stresses near the notch could also be an artifact of the crack getting pinned as discussed earlier.

Finally, Figure 5.20 shows the predicted crack paths for the 41×41 mesh for both lateral shear loads. Notice that the crack predicted for the 10 kN lateral force contains more curvature than that predicted for the 5 kN lateral force, which is consistent with the experiments. The predicted crack curvature for the 5 kN case is slightly too large compared to experiment. However, this is primarily due to the crack branching that occurs in the experiment. The initial crack curvature near the notch in the experiment is consistent to that predicted from the simulation.

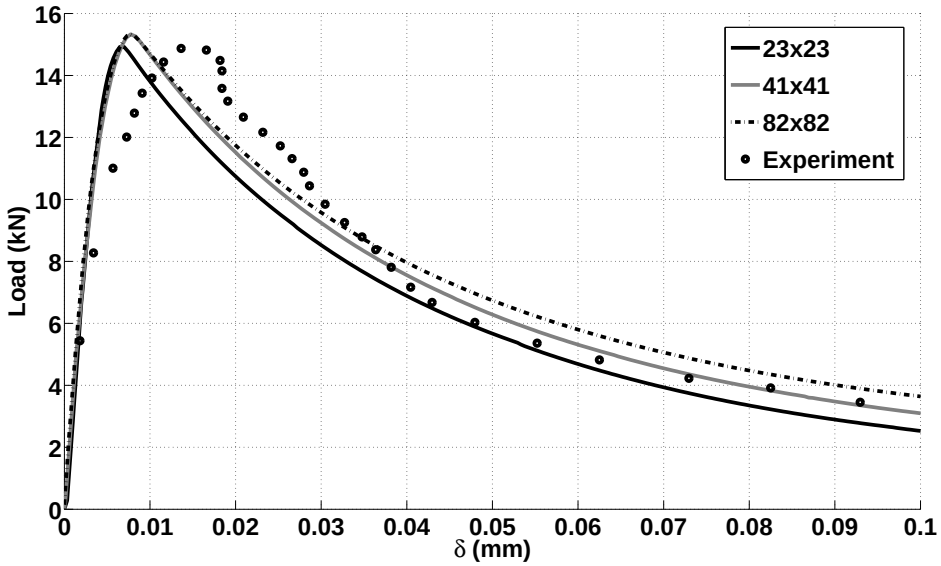

Figure 5.15: Load-deflection Curve - Shear-Tension ($F_s = 5$ kN)

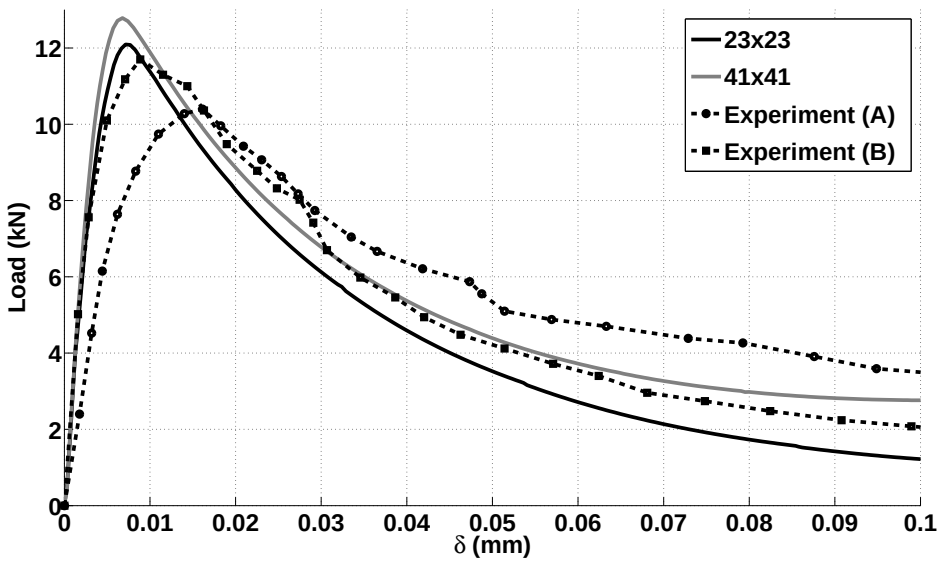

Figure 5.16: Load-deflection Curve - Shear-Tension ($F_s = 10$ kN)

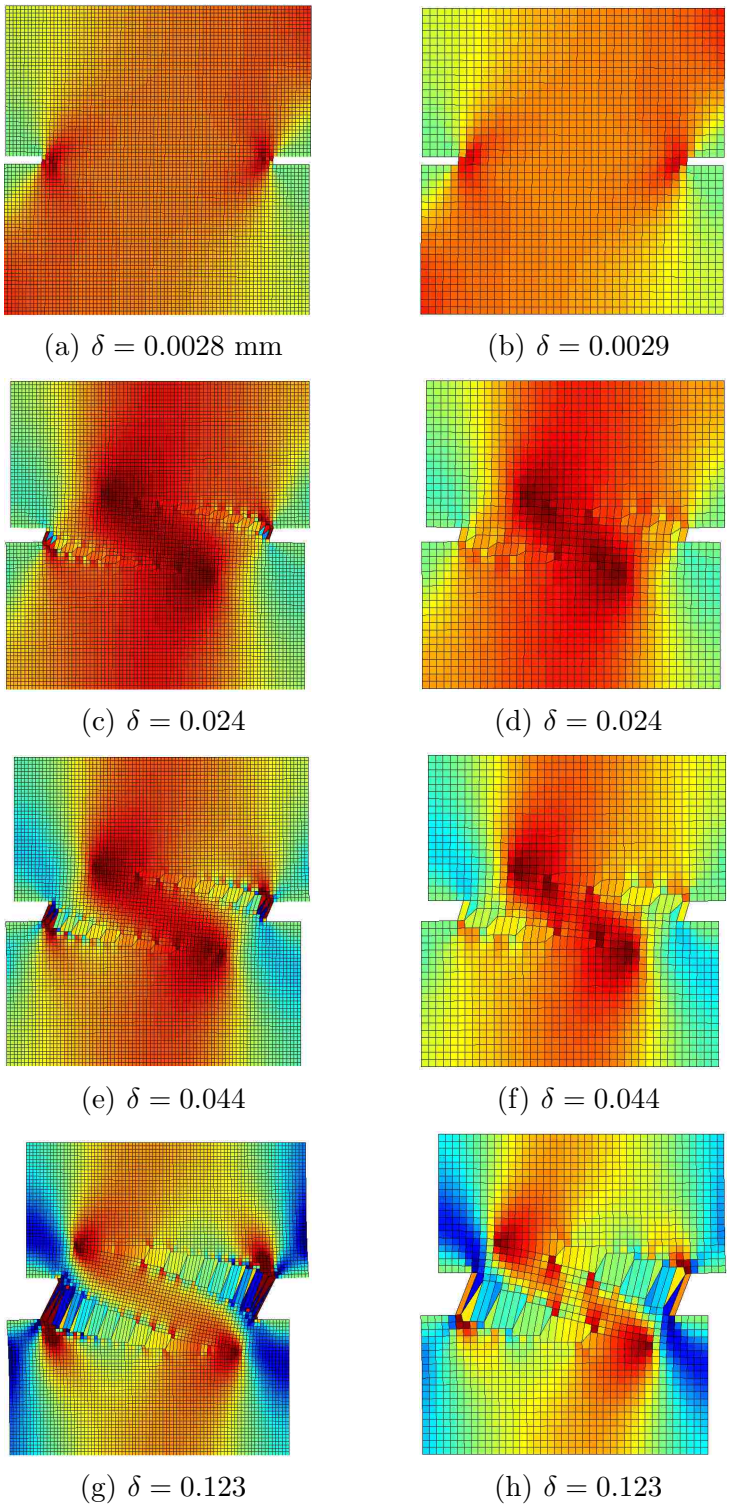

(a) $\delta = 0.0028$ mm (b) $\delta = 0.0029$

(c) $\delta = 0.024$ (d) $\delta = 0.024$

(e) $\delta = 0.044$ (f) $\delta = 0.044$

(g) $\delta = 0.123$ (h) $\delta = 0.123$

Figure 5.17: Normal Stress (σ_{yy}) - DEN Shear-Tension Simulations (scale = 200)

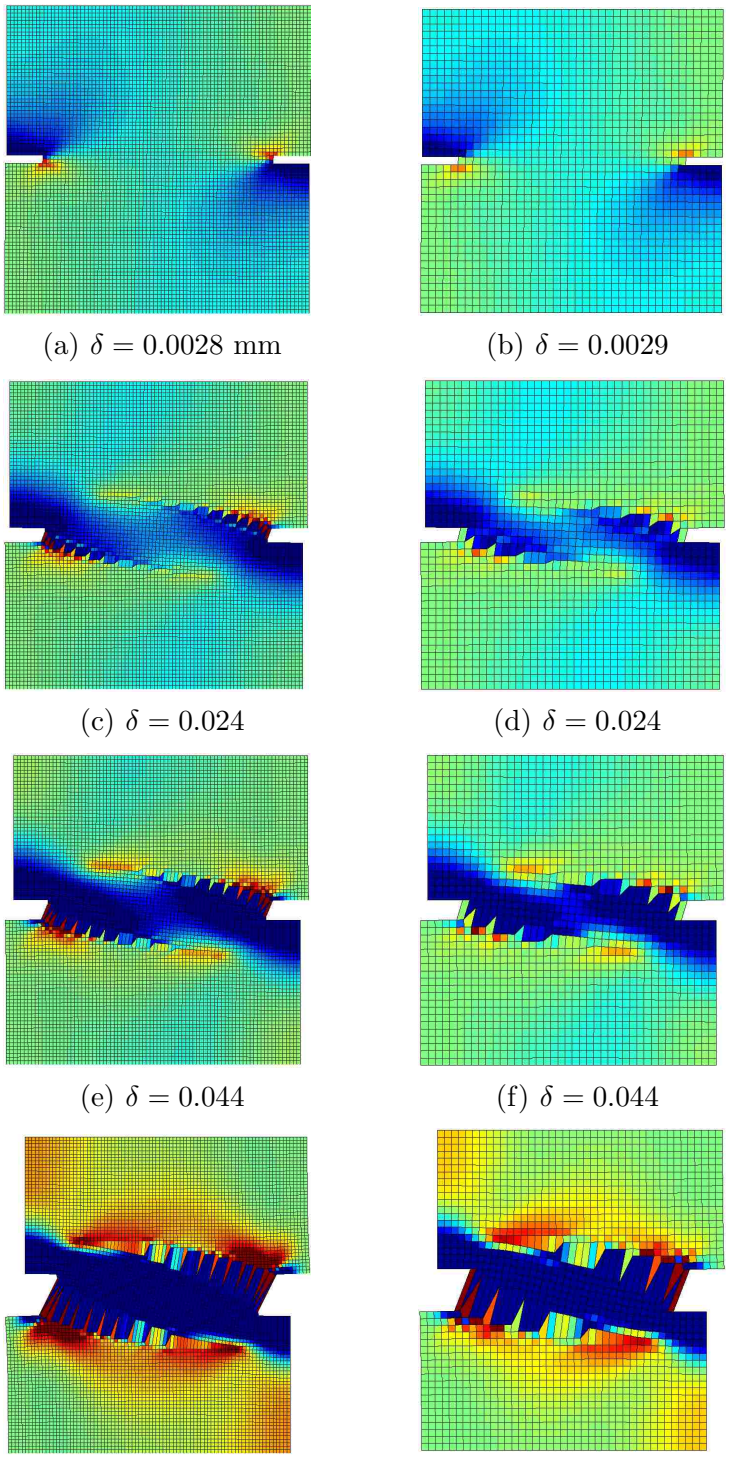

(a) $\delta = 0.0028$ mm (b) $\delta = 0.0029$

(c) $\delta = 0.024$ (d) $\delta = 0.024$

(e) $\delta = 0.044$ (f) $\delta = 0.044$

(g) $\delta = 0.123$ (h) $\delta = 0.123$

Figure 5.18: Normal Stress (σ_{xx}) - DEN Shear-Tension Simulations (scale = 200)

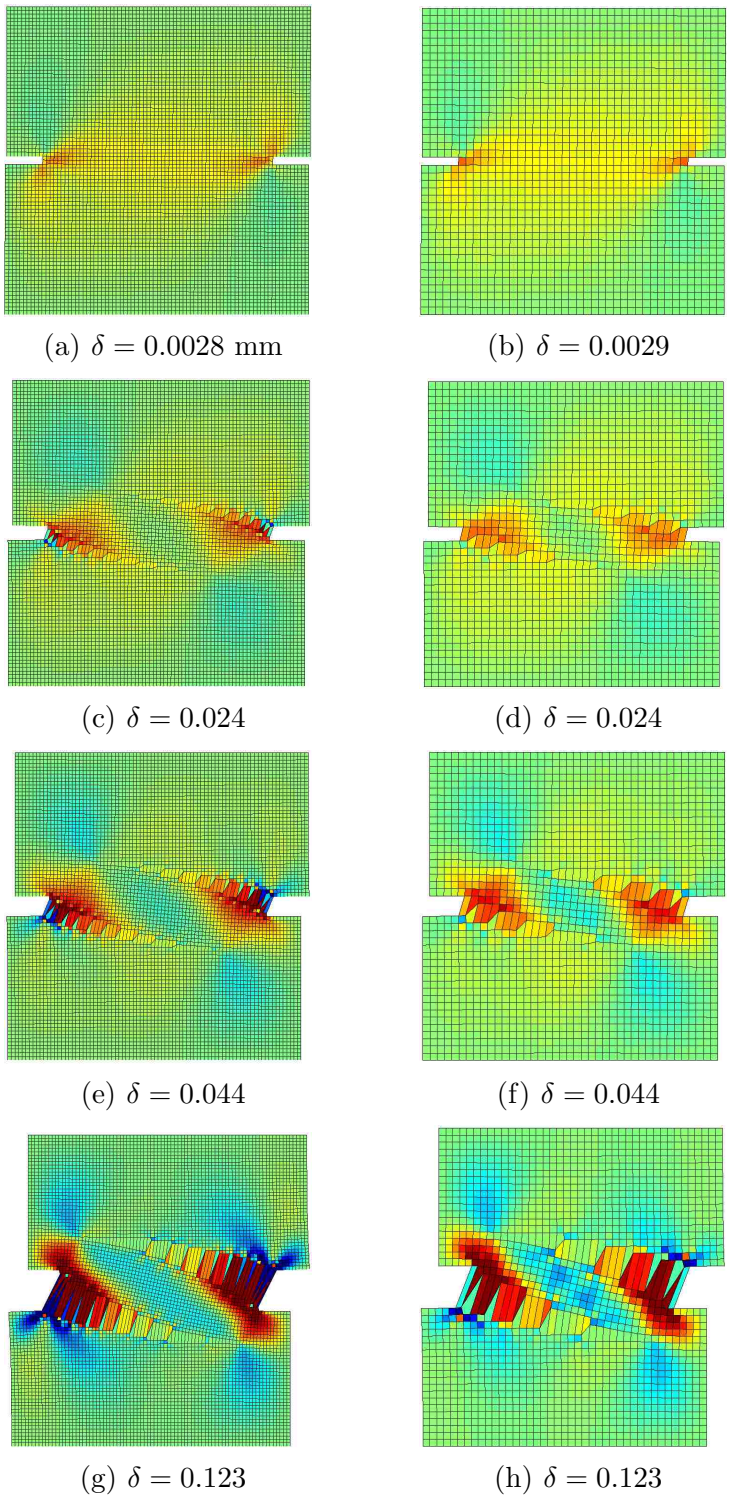

(a) $\delta = 0.0028$ mm (b) $\delta = 0.0029$

(c) $\delta = 0.024$ (d) $\delta = 0.024$

(e) $\delta = 0.044$ (f) $\delta = 0.044$

(g) $\delta = 0.123$ (h) $\delta = 0.123$

Figure 5.19: Shear Stress (σ_{xy}) - DEN Shear-Tension Simulations (scale = 200)

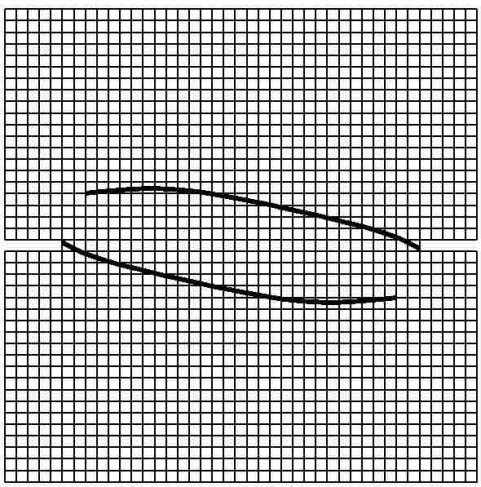

(a) Predicted - 5kN

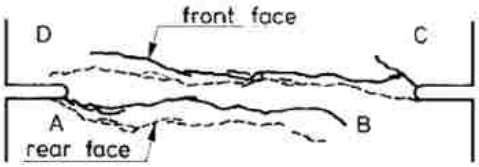

(b) Experiment - 5kN [58]

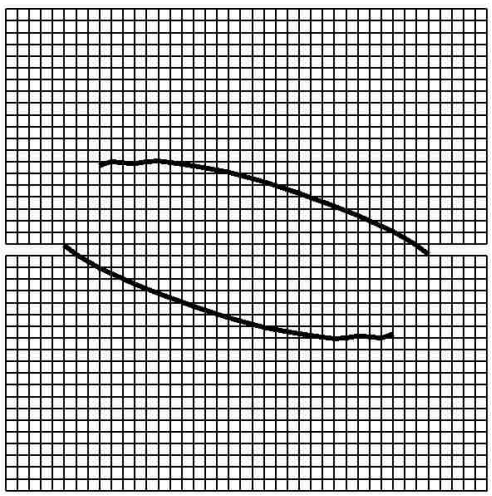

(c) Predicted - 10kN

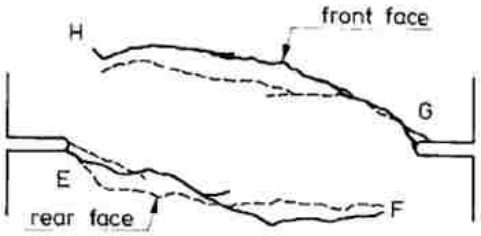

(d) Experiment - 10kN [58]

Figure 5.20: Crack Patterns for DEN Shear-Tension Problem

Chapter 6

Summary

6.1 Review of Contributions

This dissertation provides an algorithm for modeling mode-I failure using quadrilateral finite elements with standard nodal basis functions. The principal contribution of the dissertation is the development, implementation, and validation of an algorithm that provides a means to predict material failure at an angle through a finite element mesh without mesh bias. To the author's knowledge, this work represents the first time that mesh objectivity has been achieved in modeling mode-I failure at an angle through a finite element mesh using a discrete constitutive model, a standard finite element formulation, and the smeared crack approach.

Another important contribution is the simplicity, implementation convenience, and computational efficiency of the algorithm (see Section 4.6). The equations that govern the algorithm are explicit requiring no iterative methods and are formulated around one-point quadrature. The algorithm can be housed within a single constitutive model subroutine that is called by a traditional host finite element code to update the stress. The only modification necessary within the host code is to update the hourglass force contributions for a cracked element.

This contribution required the development and implementation of the following components: (1) mode-I failure model that precludes spurious shear stress along the crack surface, but keeps the crack orientation fixed as the crack evolves, (2) a crack tracking algorithm that provides the correct crack path, (3) an hourglass control method for an element undergoing softening, and (4) a cross-over scaling method that provides the correct characteristic crack dimension as a crack segment passes through two elements. All four components are necessary in order to alleviate mesh orientation bias with respect to the crack path and the load-deflection curve.

The distinguishing feature of the discrete failure model (see Section 3.3) is that the increment in shear stress along the crack surface is not allowed while the crack orientation is fixed. As a result, the total shear strain is not necessary to compute the shear stress and this paradigm precludes spurious shear stress accumulation. Spurious shear stress accumulation was identified as the primary cause of shear locking when modeling cracks using finite elements and the smeared crack approach. Because the crack orientation does not evolve with the crack opening, the crack path can be accurately represented using the crack tracking algorithm. This is in contrast to some models that must continuously rotate the crack surface.

One advantage of using a discrete failure constitutive model is that there is a specific representation of the mode of failure, which can be correlated with experimental observations. A nonlocal damage model has the disadvantage that the mode of failure can only be presumed from the path of failed elements based on the numerical solution.

A second advantage of the discrete model with a smeared crack representation is that the stability of the numerical solution is assured once it is shown that element snapback does not occur for the failure mode. Any deformation that does not activate the failure mode is elastic and therefore, stable. On the other hand, when a continuum damage model is used, there is the possibility of loss of stability and, as a consequence, a loss of convergence with mesh refinement. The stability associated

with the tangent tensor based on a discrete constitutive equation with small enough mesh size is important also in connection with hourglass control with softening.

The crack tracking algorithm (see Section 4.4) assumes that a crack is represented by a series of line segments that intersect element edges. The primary function of the crack tracking algorithm is to preclude mesh dependence of the crack path caused by the misalignment of the stress field around the crack tip. Without it, the crack would simply follow the element edges. With it brings about crack cross-over effects that must be handled appropriately as discussed later. The tracking algorithm decides which elements can fail based on which elements intersect the path of line segments that represent the crack.

Because one-point quadrature is intrinsic to the proposed algorithm, a set of appropriate hourglass control methods are required to preclude the formation of hourglass modes. More importantly, an hourglass control method for softening is required in order to obtain mesh objectivity in crack problems. Although hourglass control methods are well established for elements undergoing hardening, methods that apply to softening are not well established. A set of two new hourglass control methods are developed for both an element undergoing hardening (see Section 4.3.1) as well as softening (see Section 4.3.2). For both cases, a set of simple algebraic equations are derived for structured meshes that provide exact hourglass forces or those that reproduce four-point integration without error. For the hardening element, the primary contribution is an hourglass control method that does not require an hourglass coefficient. For the softening element, the hourglass control method selected, provides mesh objectivity. A suggested method to improve a commonly used hourglass control method is also provided.

The final piece of the mesh objective puzzle is dealing with crack cross-overs (see Section 5.2.2). Even when contributions (1) through (3) were implemented, there was still some mesh orientation bias. The load-deflection curve unloading slope was too small. These effects became worse as the mesh orientation was increased. It was

reasoned that when a cross-over crack occurs, the characteristic element dimension changes. When the cross-over dimension was used as the characteristic crack length for both elements that compose the cross-over, full mesh objectivity was obtained. When the crack tracking algorithm identifies a crack cross-over, the characteristic crack length used is simply the sum of the element dimensions that compose the cross-over. This approach was denoted cross-over scaling.

The ultimate success of the algorithm is due to integrating all contributions (1) through (4) together. Without one another mesh objectivity wouldn't have been possible. Without the proposed failure model, then spurious shear stress would result in shear locking, the crack orientation couldn't be accurately predicted, and the load-deflection curve would be erroneous. Without the crack tracking algorithm, the crack path would always follow the element edges. Without the hourglass control and cross-over scaling methods then mesh objectivity would be nearby, but would still remain elusive.

6.2 Summary of Results

The efficacy of the hourglass control method derived for the hardening element was investigated and compared to an existing approach (see Section 5.1). It was demonstrated that the integration error was zero when one-point quadrature was used for a structured mesh (i. e. square, rectangular, or parallelogram elements) with the proposed hourglass control method for hardening. In contrast, the existing approach couldn't achieve zero error for non-square elements. For arbitrary meshes, the existing hourglass control method provided a smaller minimum error than the proposed approach. It was observed that the proposed hourglass control method for a hardening element works equally well to the existing approach for the meshes considered in this dissertation.

A mode-I failure model problem was chosen to systematically investigate algo-

rithm performance for several mesh orientations and sizes (see Section 5.2). Failure was initiated in the middle of a two-dimensional bar by reducing the tensile strength of the center element. A crack was then allowed to propagate across the bar using the crack tracking algorithm. The results showed that the crack path, stress distribution, and load-deflection curves were essentially free of both mesh size and orientation bias. As the mesh was refined, the load-deflection curves became essentially the same.

The effects of crack cross-overs were investigated to show the efficacy of the cross-over scaling method proposed (see Section 5.2.2). Without cross-over scaling, mesh orientation bias was still pronounced. Stress contours showed that there were large normal stresses in cross-over elements. It was hypothesized that the accumulation of normal stress was due to an inconsistency in the unloading rate between the cross-over cracks and the cracks that are adjacent. Introducing cross-over scaling in elements within a cross-over effectively caused the cross-over cracks and adjacent cracks to unload at the same rate, which precluded the development of spurious normal stresses. Upon the implementation of cross-over scaling, mesh objectivity was finally achieved.

A set of double-edge-notch concrete experiments were selected to investigate the performance of the algorithm in modeling straight and curved cracks initiated from stress concentrations due to geometric discontinuities. In the direct-tension simulations that pull the specimen in tension (see Section 5.3), it was shown that the same load-deflection curve was obtained with an unrotated and rotated mesh. In addition, the normal stress distributions generated from both meshes were essentially the same. Finally, it was shown that when hourglass control for softening was turned off, the load-deflection curve for the oriented mesh deviated from the result obtained for the unrotated mesh. This suggested that hourglass control for softening plays an important role in obtaining mesh objectivity.

A combined shear-tension DEN simulation (see Section 5.4) was conducted to predict curved crack paths for two different lateral load cases using square meshes

of difference size. The simulation consisted of two loading stages. In the first stage, a lateral load is applied using displacement control such that the net axial force is about zero. Once the lateral force has reached the desired magnitude, the lateral and axial displacements are controlled such that the lateral force is held constant as the crack propagates.

The resulting load-deflection curves reasonably matched the experimental results. The predicted crack trajectories were curved and similar to what was obtained in the experiments. The model could also predict the larger curvature obtained in the larger lateral load case. The resulting stress contours between a coarse and a fine mesh were similar indicating that the forces in the material are represented without mesh bias. As the mesh was refined, the load-deflection curves shifted slightly upward. It was hypothesized that the root cause of this behavior was the spurious accumulation of normal stress near the notch brought on by not allowing additional cracks to form around the notch. The crack essentially gets pinned or stuck and normal stress continues to rise beyond the tensile strength. A fix for this would be to adjust the crack tracking algorithm to allow more cracks to occur in the notch region to prevent stress accumulation.

The failure model could still represent the unloading stage of the experimental data reasonably well even when the shear stress along the crack surface wasn't allowed to accumulate. This might suggest that for this specific combined shear-tension problem, the effects of shear along the crack surface are a minor contribution to the overall load-deflection curve. This isn't too surprising as the primary load path in the material during the cracking phase is of tension. In general, the algorithm was able to capture the features observed in the experiments.

6.3 Limitations to Proposed Methods

The assumptions initially defined set the course for many of the limitations of the proposed algorithm. The algorithm was formulated under the pretense of brittle material failure with little to no confining stress and small deformations. A limitation of the procedure is the step taken to prevent the development of parasitic shear; namely, a constraint that enforces zero shear stress once a mode-I crack is initiated. Recall that the shear stress is zero at crack initiation, and is zero when the complete crack is formed. As a result, the error caused by enforcing zero shear stress throughout the crack development may be significant. The constraint of zero shear stress implies that the potential evolution of shear due to a change in the loading path occurs in adjacent elements and, hence, will affect the orientation of the crack continuation. This is the approach that may be considered as an alternative and an improvement to the algorithm often used in the literature based on the assumption of a rotating crack, which does not address the issue of parasitic shear stress.

For more general discrete constitutive failure models that allow mixed mode behavior, corresponding constraints can be constructed that also prevent corresponding parasitic stress components. For many problems, a shear force along the crack surface is necessary such as for ductile material failure of concrete under large confining stress.

Because small deformations were assumed, it is unknown how applying large deformation kinematics will affect the results. This sort of formulation would be required for problems that involve plastic deformation prior to the onset of failure such as ductile failure in metals. However, adding plasticity would be rather straightforward as a plastic strain contribution to the total strain would be added. A separate portion of the constitutive model would handle the hardening response while the decohesion portion would still handle the softening response.

The algorithm was implemented and tested using a two-dimensional finite ele-

ment formulation to simplify the implementation, but mostly to simplify the post-processing, interpretation of the results, and reduce simulation run times. Presently, we do not foresee an issue in moving to three dimensions. Additional components of strain, stress, and crack opening displacement would be required. However, because code implementation usually presents a painful journey, at least for this author, we list this aspect as a possible issue principally due to unforeseen computational aspects that may present themselves.

6.4 Follow-on Research

The potential limitations presented in the previous section present possible future research efforts. A similar algorithm for mode-II failure could be developed to preclude spurious normal stress for failure in ductile materials. Large deformation kinematics could be introduced along with plasticity. Mixed mode failure could be investigated for concrete failure under large confining stress.

Another branch of research is applying the algorithm to particle methods that use finite element calculations in the background such as the Material-Point Method (MPM) [28]-[30]. In theory, the algorithm should also make MPM computations objective with respect to the computational grid when modeling mode-I brittle failure. This might apply to problems that involve ice, rock, and concrete.

Appendix A

Derivation of Cracked Element Edge Coordinates

The cracked element edge coordinates (CEECS) are used in the crack tracking algorithm to compute the path of the crack through the mesh based on the crack orientation $\mathbf{n}$ and the starting crack coordinates (SCCS) of the initiated crack denoted (x^e_{cr}, y^e_{cr}). The SSCS are the coordinates of the crack root that start each crack segment after the first initiated crack has formed and they are either (x^e_1, y^e_1) or (x^e_2, y^e_2) from the previous cracked element in the crack branch. For example, for cracked element 1 in Figure A.1, the SCCS are $(x^1_{cr}, y^1_{cr}) = (x^n_2, y^n_2)$, where (x^n_2, y^n_2) are the CEECS for the North element (N). For tracking cracks in problems considered here, we define three sets of CEECS: (1) coordinates for first initiated cracks (x^c_1, y^c_1) and (x^c_2, y^c_2), (2) coordinates (x^e_2, y^e_2) for the crack segment leading off of either (x^c_2, y^c_2) or (x^e_{cr}, y^e_{cr}), and (3) coordinates (x^e_1, y^e_1) leading off of either (x^c_1, y^c_1) or (x^e_{cr}, y^e_{cr}). The CEECS compute flag listed in the algorithm in Section 4.5, corresponds to cases (1) through (3). Note that for case (1), the first initiated cracks are those that initiate a crack branch. For example, for the double-edge-notch simulations in Section 5.4, there are two first initiated cracks because there are two separate crack branches. As

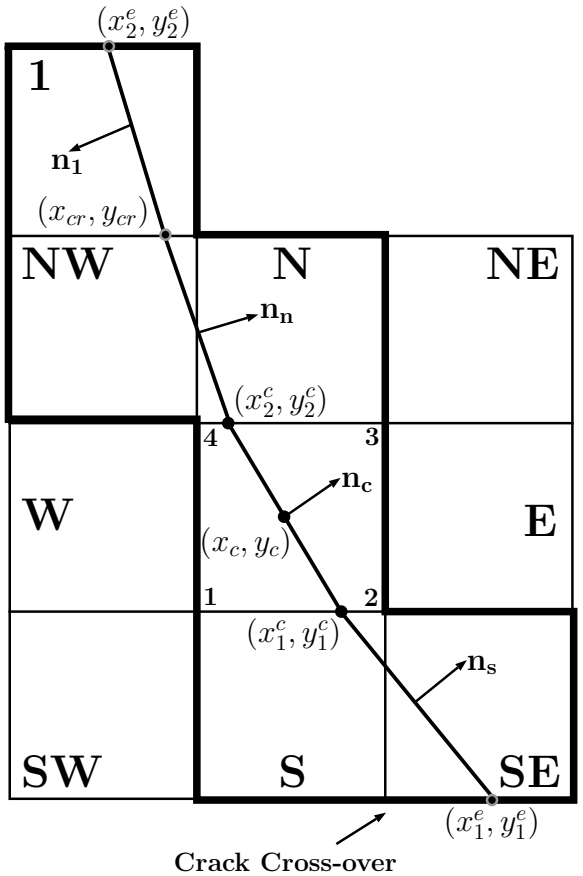

Figure A.1: Tracking a Crack Through a Mesh

a result, (x_1^c, y_1^c) and (x_2^c, y_2^c) are computed only twice in the simulation.

The general procedure for deriving the CEECS is to express the equation of the line representing the crack segment in terms of the crack orientation $\mathbf{n}$ and another equation for the line representing the element edge that corresponds to the CEECS that are to be computed. These two equations are then solved simultaneously to determine the CEECS. The first equation is formed by taking the dot product of the normal vector $\mathbf{n}$ and a vector defining the crack segment in terms of nodal coordinates. The second equation is formed by using the point-slope formula and

setting $x = x_i^e$ and $y = y_i^e$. Applying this for case (1), we have

$$0 = (x_1^c - x_c)n_1 + (y_1^c - y_c)n_2 \tag{A.1}$$

$$0 = \frac{x_1^c - x_1}{x_2 - x_1} - \frac{y_1^c - y_1}{y_2 - y_1}, \tag{A.2}$$

where n_1 and n_2 are the vector components of $\mathbf{n}$ in the global $\{x, y\}$ coordinate system, (x_i, y_i) are the nodal coordinates, and (x_c, y_c) are the coordinates for the element center corresponding to the first initiated crack. Solving eqs. A.1 and A.2 results in

$$x_1^c = \frac{\left[x_2y_1 - x_1y_2 + (x_1 - x_2)\, y_c\right] n_2 + (x_1 - x_2)\, n_1 x_c}{(x_1 - x_2)\, n_1 + (y_1 - y_2)\, n_2} \tag{A.3}$$

$$y_1^c = \frac{\left[x_1y_2 - y_1x_2 + (y_1 - y_2)\, x_c\right] n_1 + (x_1 - x_2)\, n_2 y_c}{(x_1 - x_2)\, n_1 + (y_1 - y_2)\, n_2} \tag{A.4}$$

$$x_2^c = \frac{\left[x_4y_3 - x_3y_4 + (x_3 - x_4)\, y_c\right] n_2 + (x_3 - x_4)\, n_1 x_c}{(x_3 - x_4)\, n_1 + (y_3 - y_4)\, n_2} \tag{A.5}$$

$$y_2^c = \frac{\left[x_3y_4 - y_3x_4 + (y_3 - y_4)\, x_c\right] n_1 + (y_3 - y_4)\, n_2 y_c}{(x_3 - x_4)\, n_1 + (y_3 - y_4)\, n_2}. \tag{A.6}$$

If we have a first initiated crack starting a crack branch, the CEECS compute flag is set to 1 and eqs. A.3 through A.6 are used to compute the CEECS.

Following a similar procedure from the previous example and setting up equations for the crack segments leading from (x_2^c, y_2^c) and (x_1^c, y_1^c), results in the CEECS equations for cases (2) and (3), respectively as follows:

$$x_2^e = \frac{\left[x_4y_3 - x_3y_4 + (x_3 - x_4)\, y_{cr}\right] n_2 + (x_3 - x_4)\, n_1 x_{cr}}{(x_3 - x_4)\, n_1 + (y_3 - y_4)\, n_2} \tag{A.7}$$

$$y_2^e = \frac{\left[x_3y_4 - y_3x_4 + (y_3 - y_4)\, x_{cr}\right] n_1 + (y_3 - y_4)\, n_2 y_{cr}}{(x_3 - x_4)\, n_1 + (y_3 - y_4)\, n_2} \tag{A.8}$$

$$x_1^e = \frac{\left[x_2y_1 - x_1y_2 + (x_1 - x_2)\, y_{cr}\right] n_2 + (x_1 - x_2)\, n_1 x_{cr}}{(x_1 - x_2)\, n_1 + (y_1 - y_2)\, n_2} \tag{A.9}$$

$$y_1^e = \frac{\left[x_1y_2 - y_1x_2 + (y_1 - y_2)\, x_{cr}\right] n_1 + (x_1 - x_2)\, n_2 y_{cr}}{(x_1 - x_2)\, n_1 + (y_1 - y_2)\, n_2}. \tag{A.10}$$

For case (2), we set the CEECS compute flag to 2 and eqs. A.7 and A.8 are used to compute the CEECS. Finally, for case (3), the CEECS compute flag is set to 3 and eqs. A.9 and A.10 are used to compute the CEECS.

All that is required to compute current crack segment information is the crack normal $\mathbf{n}$ of the current initiated crack, the SCCS, (x^e_{cr}, y^e_{cr}), which are equal to either (x^e_1, y^e_1) or (x^e_2, y^e_2) from the previous cracked element in the crack branch, and the nodal coordinates of the current initiated cracked element or the adjacent element that is slated to crack next. The CEECS and the adjacent element array E_{adj} are used to choose which elements are next in line to fail. If one of the adjacent elements has cracked, then a search is performed to find which element is evolving a crack or which element has a crack condition code $\mathrm{C}_{cond}(n_e, 2) = 2$. The CEECS compute flag and SCCS are then chosen based on which position in the adjacent element array the evolving crack is located. Then the next set of adjacent elements are determined using logic comparisons based on comparisons between the CEECS and the nodal coordinates of the evolving cracked element. This process continues as new cracks initiate.

For crack paths that involve an inflection in the crack path, then slight modifications to the SCCS and CEECS compute flag are necessary. For example, in the DEN direct-tension simulations, the crack normal component in the x-direction n_1 changes sign as the crack path goes downward for the top crack (or upward for the bottom crack). In the *Get-Crack* subroutine, which determines the SCCS and the CEECS compute flag, a search is performed to identify when a crack inflection occurs. If the condition is true, then the SCCS and compute flags for cases (2) and (3) are switched. The CEECS are then computed with the swapped SCCS and CEECS compute flag in the *Compute-CEECS* subroutine. Finally, it might be necessary to adjust the definition of the failure angle in eq. 4.105 depending on the interval that the $ATAN$ function is defined. Another approach is to setup the problem such that the curved cracks travel up/down if $ATAN$ is defined on the interval $[-\pi, \pi]$.

Appendix B

Standard Decohesion Model

In Section 5.2, results were compared to a *standard* decohesion model. This Appendix presents the equations for a standard mode-I decohesion model that uses the full strain field to compute the stress.

We start with the same decohesion function as used in the proposed model that assumes linear softening

$$F = \frac{\tau_n}{\tau_{nf}} + \frac{u_n}{u_0} - 1. \tag{B.1}$$

Applying eq. 3.23 results in

$$[[\dot{u}_n]] = \dot{\omega}\frac{\partial F}{\partial \tau_n} = \frac{\dot{\omega}}{\tau_{nf}}, \tag{B.2}$$

where $\dot{\omega}$ is a positive monotonically increasing function. Dropping the [[ ]] on $\dot{u_n}$ and applying the consistency condition $\dot{F} = 0$ results in

$$\dot{F} = \frac{\dot{\tau}_n}{\tau_{nf}} + \frac{\dot{u}_n}{u_0} = 0. \tag{B.3}$$

Substituting in eq. B.5 into eq. B.3 and solving for $\dot{\omega}$ results in

$$\dot{\omega} = -\dot{\tau}_n u_0. \tag{B.4}$$

Substituting in eq. B.4 into eq. B.5 results in

$$\dot{u}_n = -\frac{\dot{\tau}_n u_0}{\tau_{nf}}. \tag{B.5}$$

Next, we apply the smeared crack formalism such that the total strain is additively decomposed into elastic and crack strain contributions as follows:

$$\mathbf{e} = \mathbf{e}^{e} + \mathbf{e}^{cr}. \tag{B.6}$$

Applying Hooke's law and eq. B.6 results in the stress for a cracked element

$$\boldsymbol{\sigma} = \mathbb{E} : \mathbf{e}^{e} = \mathbb{E} : (\mathbf{e} - \mathbf{e}^{cr}). \tag{B.7}$$

Next, we transform the generalized Hooke's law relation for the stress into a matrix-vector relation for a two-dimensional state of stress using the 3×3 elasticity matrix $[C]$ and the strain vector e^{v} as follows:

$$\{\sigma^{v}\} = [C]\,\{e^{v}\}, \tag{B.8}$$

where

$$\{\sigma^{v}\} = \begin{Bmatrix} \sigma_{xx} \\ \sigma_{yy} \\ \sigma_{xy} \end{Bmatrix} \tag{B.9}$$

$$\{e^{v}\} = \begin{Bmatrix} e_{xx} \\ e_{yy} \\ 2e_{xy} \end{Bmatrix}. \tag{B.10}$$

When a crack forms, the stress update takes place in the $\{\mathbf{n}, \mathbf{t}\}$ basis. As a result, we must have equations that define σ_{nn}, σ_{tt}, and σ_{nt}. These equations are as follows for the standard decohesion model:

$$\sigma_{nn} = C_{11}(e_{nn} - e^{cr}_{nn}) + C_{12}e_{tt} \tag{B.11}$$

$$\sigma_{tt} = C_{12}(e_{nn} - e^{cr}_{nn}) + C_{22}e_{tt} \tag{B.12}$$

$$\sigma_{nt} = 2C_{33}e_{nt}. \tag{B.13}$$

Because a mode-I Rankine failure model is assumed, the only strain component that contains a crack strain is the normal component. Hence $e^{cr}_{tt} = 0$ and $e^{cr}_{nt} = 0$ From

eq. 3.27, the crack strain is

$$e_{nn}^{cr} = u_n / h_c. \tag{B.14}$$

If the decohesion function $F > 0$, then eqs. B.11 through B.14 are used to update the stress in the crack basis. The algorithm computes the u_n required that achieves $F \approx 0$. Then the local stress components are transformed back to the global basis.

Now let's examine the differences between the failure model proposed in Section 3.3 and the standard model proposed here. First, notice that now we have a nonzero σ_{nt} component defined in eq. B.13 that is a function of the shear strain e_{nt}. As we know from Section 2.2.1, once a mode-I crack is opened up in a finite element, a spurious e_{nt} component accumulates linearly with the crack opening displacement u_n. Applying $\sigma_{nt} = 2C_{33}e_{nt}$ then results in a spurious shear stress. This is the root cause of the poor performance of the standard decohesion model observed in Section 5.2.

In contrast, the new failure model is formulated to ensure that spurious shear stress does not accumulate when a crack opens by setting $\Delta\sigma_{nt} = 0$. Hence, the new failure model doesn't use e_{nt}. The implication of such an approach, is that the shear stress in the crack cannot evolve. This assumption is appropriate for concrete under very little compression which is assumed here. For materials that require shear evolution such as concrete under large compression, the evolution equation for the shear stress could be related to the normal stress σ_{nn} using a Mohr-Coulomb relationship.

The rotating crack model (RCM) enforces $e_{nt} = 0$ by rotating the crack orientation throughout a simulation defined by the the eigenvectors of the strain tensor such that the crack normal is always in line with the most tensile principal strain. It is then interpreted that the resulting principal strains are e_{nn} and e_{tt}. However, this model leads to an inconsistency between the physical crack orientation and what is termed the *computational crack* or the crack orientation necessary to enforce $e_{nt} = 0$. Therefore, it is difficult to use this model to predict the physical crack orientation.

References

[1] Y. Rashid. Analysis of prestressed concrete pressure vessels. *Nuclear Engineering and Design*, 7:334–344, 1969.

[2] D. Ngo and A. C. Scordelis. Finite element analysis of concrete beams. *ACI Journal*, 64(14):152–163, 1967.

[3] T. Belytschko and T. Black. Elastic crack growth in finite elements with minimal remeshing. *Journal of Numerical Methods in Engineering*, 45:455–471, 1999.

[4] T. J. R. Hughes. *The Finite Element Method: Linear Static and Dynamic Finite Element Analysis*. General Publishing Company, Don Mills, Toronto, Ontario, 2000.

[5] R. Hill. A general theory of uniqueness and stability in elastic-plastic solids. *Journal of the Mechanics and Physics of Solids*, 6:236–249, 1958.

[6] H. L. Schreyer and M. K. Neilsen. Analytical and numerical tests for loss of material stability. *International Journal for Numerical Methods in Engineering*, 39:1721–1736, 1996.

[7] M. K. Neilsen and H. L. Schreyer. Bifurcations in elastic-plastic materials. *Numerical and Analytical Methods in Geomechanics*, 30(4):521–544, 1993.

[8] H. L. Schreyer. Modelling surface orientation and stress at failure of concrete and geological materials. *Numerical and Analytical Methods in Geomechanics*, 31:147–171, 2007.

[9] Z. P. Bazant. Instability, ductility, and size effect in strain-softening concrete. *Journal of the Engineering Mechanics Division*, 102(2):331–344, 1976.

[10] Z. P. Bazant and B. H. Oh. Crack band theory for fracture of concrete. *Materials and Structures*, 16:155–177, 1983.

[11] A. C. Eringen and D. G. B. Edelen. On nonlocal elasticity. *International Journal of Engineering Science*, 10(3):233–248, 1972.

[12] Z. P. Bazant and F.-B. Lin. Nonlocal smeared cracking model for concrete fracture. *Journal of Structural Engineering*, 114(11):2493–2510, 1988.

[13] M. Jirásek. Nonlocal models for damage and fracture: Comparison of approaches. *International Journal of Solids and Structures*, 35(31-32):4133–4145, 1998.

[14] E. C. Aifantis. On the microstructural origin of certain inelastic models. *Journal of Engineering Materials and Technology*, 106:326–330, 1984.

[15] E. C. Aifantis. On the role of gradients in the localization of deformation and fracture. *International Journal of Engineering Science*, 30:1279–1299, 1992.

[16] S. A. Silling. Reformulation of elasticity theory for discontinuities and long-range forces. *Journal of Mechanics and Physics of Solids*, 48:175–209, 2000.

[17] S. A. Silling, M. Epton, O. Weckner, J. Xu, and E. Askari. Peridynamics states and constitutive modeling. *Journal of Elasticity*, 88:151–184, 2007.

[18] J. T. Foster, S. A. Silling, and W. W. Chen. Viscoplasticity using peridynamics. *International Journal for Numerical Methods in Engineering*, 81(10):1242–1258, 2010.

[19] J. G. Rots. *Computational modeling of concrete fracture*. PhD thesis, Delft University of Technology, 1988.

[20] J. G. Rots. Smeared and discrete representations of localized failure. *International Journal of Fracture*, 51:45–59, 1991.

[21] R. de Borst and P. Nauta. Non-orthogonal cracks in a smeared finite element model. *Engineering Computations*, 2:35–46, 1985.

[22] M. Jirásek and T. Zimmermann. Analysis of rotating crack model. *Journal of Engineering Mechanics*, 124(8):842–851, 1998.

[23] M. Jirásek and T. Zimmermann. Rotating crack model with transition to scalar damage. *Journal of Engineering Mechanics*, 124(3):277–284, 1998.

[24] L. Xu, H. L. Schreyer, and D. L. Sulsky. Blast-induced rock fracture near a tunnel. *International Journal for Numerical and Analytical Methods in Geomechanics*, 39:23–50, 2014.

[25] H. L. Schreyer, D. L. Sulsky, L. B. Munday, M. D. Coon, and R. Kwok. Elastic-decohesive model for sea ice. *Journal for Geophysical Research*, 111:C11S26, 2006.

[26] D. L. Sulsky, H. L. Schreyer, K. Peterson, R. Kwok, and M. Coon. Using the material-point method to model sea ice dynamics. *Journal for Geophysical Research*, 112:C02S90, 2007.

[27] C. A. Rutland and M. L. Wang. The effects of confinement on the failure orientation in cementitious materials: experimental observations. *Cement and Concrete Composites*, 19:149–160, 1997.

[28] D. Sulsky, Z. Chen, and H. L. Schreyer. A particle method for history-dependent materials. *Computer Methods in Applied Mechanics and Engineering*, 118(1-2):179–196, 1994.

[29] D. Sulsky, S.-J. Zhou, and H. L. Schreyer. Application of a particle-in-cell method to solid mechanics. *Computer Physics Communications*, 87(1-2):236–252, 1995.

[30] D. Sulsky and H. L. Schreyer. Axisymmetric form of the material point method with applications to upsetting and taylor impact problems. *Computer Methods in Applied Mechanics and Engineering*, 139(1-4):409–429, 1996.

[31] G. R. Johnson, S. R. Beissel, and R. A. Stryk. An improved generalized particle algorithm that includes boundaries and interfaces. *International Journal for Numerical Methods in Engineering*, 53(4):875–904, 2002.

[32] M. Cervera and M. Chiumenti. Smeared crack approach: back to the original track. *International Journal of Analytical Methods in Geomechanics*, 30:1173–1199, 2006.

[33] M. Cervera. An orthotropic mesh corrected crack model. *Computational Methods in Applied Mechanical Engineering*, 197:1603–1619, 2008.

[34] M. Cervera, M. Chiumenti, and R. Codina. Mesh objective modeling of cracks using linear strain and displacement interpolations. *International Journal for Numerical Methods in Engineering*, 87:962–987, 2011.

[35] M. Jirásek. A comparitive study on finite elements with embedded discontinuities. *Computer Methods in Applied Mechanics and Engineering*, 188:307–330, 2000.

[36] M. Ortiz, Y. Leroy, and A Needleman. A finite element method for localized failure analysis. *Computer Methods in Applied Mechanics and Engineering*, 61(2):189–214, 1987.

[37] T. Belytschko, J. Fish, and B. E. Engelmann. A finite element with embedded localization zones. *Computer Methods in Applied Mechanics and Engineering*, 70(1):59–89, 1988.

[38] E. N. Dvorkin, A. M. Cuiti no, and G. Gioia. Finite elements with displacement interpolated embedded localization lines insensitive to mesh size and distortions. *International Journal for Numerical Methods in Engineering*, 30(3):541–564, 1990.

[39] C. Linder and F. Armero. Finite elements with embedded strong discontinuities for the modeling of failure in solids. *International Journal for Numerical Methods in Engineering*, 72:1391–1433, 2007.

[40] R. E. Goodman, R. L. Taylor, and T. L. Brekke. A model for the mechanics of jointed rock. *Journal for the Soil Mechanics and Foundations Division*, 94(3):637–660, 1968.

[41] A. Hillerborg, M. Modéer, and P.-E. Petersson. Analysis of crack formation and crack growth in concrete by means of fracture mechanics and finite elements. *Cement and Concrete Research*, 6(6):773–781, 1976.

[42] A. R. Ingraffea and V. Saouma. Numerical modeling of discrete crack propagation in reinforced and plain concrete. *Engineering Application of Fracture Mechanics*, 4:171–225, 1985.

[43] T. Strouboulis, K. Copps, and I. Babuška. The generalized finite element method. *Computer Methods in Applied Mechanics and Engineering*, 190(32-33):4081–4193, 2001.

[44] J. Oẑbolt and Z. P. Bažant. Numerical smeared fracture analysis: nonlocal microcrack interaction approach. *International Journal for Numerical Methods in Engineering*, 39:635–661, 1996.

[45] J. Sanchez. *A Critical Evaluation of Computational Fracture Using a Smeared Crack Approach in MPM.* PhD thesis, University of New Mexico, 2010.

[46] J. Oliver. Modelling strong discontinuities in solid mechanics via strain softening constitutive equations. part 1: Fundamentals. *International Journal for Numerical Methods in Engineering*, 39(21):3575–3600, 1996.

[47] J. Oliver, A. E. Huespe, M. D. G. Pulido, and E. Chaves. From continuum mechanics to fracture mechanics: the strong discontinuity approach. *Engineering Fracture Mechanics*, 69:113–136, 2002.

[48] J. Oliver. Modelling strong discontinuities in solid mechanics via strain softening constitutive equations. part 2: Numerical simulation. *International Journal for Numerical Methods in Engineering*, 39(21):3601–3623, 1996.

[49] H. L. Schreyer. Introduction to computational mechanics. Book in Draft, 2010.

[50] D. P. Flanagan and T. Belytschko. A uniform strain hexahedron and quadrilateral with orthogonal hourglass control. *International Journal for Numerical Methods in Engineering*, 17(5):679–706, 1981.

[51] W. K. Liu, J. S.-J. Ong, and R. A. Uras. Finite element stabilization matrices - a unification approach. *Computer Methods in Applied Mechanics and Engineering*, 53:13–46, 1985.

[52] Maplesoft. *Maple 18. Maplesoft, a division of Waterloo Maple Inc., Waterloo, Ontario.*

[53] M. G. D. Geers, R. de Borst, and R. H. J. Peerlings. Damage and crack modeling in single-edge and double-edge notched concrete beams. *Engineering Fracture Mechanics*, 65:247–261, 2000.

[54] M. Cervera and M. Chiumenti. Mesh objective tensile cracking via a local continuum damage model and a crack tracking technique. *Computer Methods in Applied Mechanics and Engineering*, 196:304–320, 2006.

[55] M. Cervera, L. Pelá, R. Clemente, and P. Roca. A crack-tracking technique for localized damage in quasi-brittle materials. *Engineering Fracture Mechanics*, 77:2431–2450, 2010.

[56] P. Grassl and M. Jirásek. On mesh bias of local damage models for concrete. In Li VC et. al., editor, *Proceedings of the 5th International Conference on Fracture Mechanics of Concrete Structures (FraMCoS-5)*, pages 255–262, 2004.

[57] G. W. Wellman. A simple approach to modeling ductile failure. Technical Report SAND2012-1343, Sandia National Laboratories, JUNE 2012.

[58] M. B. Nooru-Mohamed. *Mixed-mode fracture of concrete: an experimental approach.* PhD thesis, Delft University of Technology, 1992.